The possible treatments for human diseases based on distinct biomechanical properties of living cells utilizing the atomic force microscopy techniques

Inaugural dissertation

for the attainment of the title of doctor
in the Faculty of Mathematics and Natural Sciences
at the Heinrich Heine University Düsseldorf

Presented by

Hsiao-Ching Tsai
from Chiayi County, Taiwan

Düsseldorf, June 2021

from the Institute of Applied Physics
at the Heinrich Heine University Düsseldorf

Published by permission of the
Faculty of Mathematics and Natural Science at
Heinrich Heine University Düsseldorf

Supervisor: Prof. Dr. Mathias Getzlaff

Date of the oral examination:

Abstract

Certain diseases are known to cause changes in the biomechanical and biophysical properties of cells. Typically, physical property changes can result in several-fold increases or decreases in the cell elasticity and can result in severe pathology and eventual catastrophic breakdown of bodily functions. This study provides insights into the intercellular structural reorganization and single-cell mechanical characterization of human cells in the context of diseases. These include cancer and Progeria. Force application techniques use the cell's response to the force applied to the cell as a way to measure cell mechanical properties. Cell functions in response to these stresses are directly related to their mechanical properties. Changes in biomechanics are therefore associated with diseases. Single-cell mechanical response characterization and surface-feature analysis require such tools as atomic force microscopy (AFM). AFM represents a developed method to detect the absence or presence of diseases, providing rapid, precise, and sensitive methods to detect and diagnose diseases. The results reveal that an approximately two-fold increase or decrease in elasticity from normal to pathological cells. The reorganization of the cellular cytoskeleton network at the onset of human diseases is also observed. AFM assessment demonstrates the impact of human diseases on cellular functions. Details of cellular properties may help to develop modern cell-selective treatments for human diseases. Medical ultrasound is a widely used technique enabling both diagnostic and therapeutic applications. Different cells can respond differently to different frequencies of ultrasound-based on their divergence in biomechanical properties and morphology. Therefore, characterizing and measuring the cells' properties are essential for the potential treatments. Besides, the transfection technique is a procedure artificially introducing foreign nucleic acids into human cells to produce genetically modified cells. Virus-mediated transfection, the most commonly used method, deliveries a gene into cells to produce recombinant proteins, or to enhance (or inhibit) specific gene expression in cells. However, the modification can cause changes in cell functions through biomechanical and biophysical mechanisms. Hence, these changes in cells are studied using AFM.

Contents

1 Introduction

Biomechanics The study of biological systems, particularly their structure and function, uses methods derived from mechanics, which refers to the investigation of motion phenomena in biological systems. Ideas and investigations relating to biomechanics date back at least to the Renaissance, when Italian physiologist and physicist Giovanni Alfonso Borelli first described muscular movement and other body functions according to the laws of statics and dynamics [1]. In the 20th century, research in biomechanics then became more widely known.

Contemporary biomechanics is a multidisciplinary field that combines physical and engineering expertise with knowledge from the biological and medical sciences. Biomechanics brings together a broad range of different disciplines: construction and aerospace engineers, biologists, physicists, medical practitioners, sports scientists, mathematicians, and computer specialists [2].

Biomechanics is the application of mechanical engineering principles to living organisms, is considered one of the core disciplines to understand the principle of physiology and pathophysiology in humans [3]. Biomechanics of organisms can be examined at different levels: cellular level, tissue level, organ level, and so on. Engineering principles may be used to understand the cause and progression of many human diseases. A basic understanding of these principles is beneficial for clinicians and medical professionals.

The thesis It presents the necessary background of engineering mechanics pertaining to biomechanics in the human body. The purpose of this study is to investigate how cell functions and behaviors are disturbed by one or more abnormalities in the genome, called mutations.

Alternations of biomechanical properties of cells and tissues are associated with cell processes and many human diseases. AFM provides the capacity to acquire high-resolution images of biosamples at the nanoscale and allows for readily carrying out mechanical characterization. High resolution of cytoskeleton organization and quantitative analysis of elastic moduli are assessed using AFM. A better understanding of the molecular biophysical basis of cellular mechanotransduction seems likely to lead to new nanotechnology-based therapeutics across a broad spectrum of disorders.

Chapters This thesis consists of five chapters. An introduction to the scientific background of this thesis is elucidated in chapter two. The biological background of human cells is first introduced. Methods from the field of mechanics applied to the cells used in a range of applications are presented in the following section.

The experimental setup of samples and different instruments are introduced and explained respectively in chapter three. The treatments for various measurements are covered as well.

In chapter four the results are presented and discussed. Chapter four can be split into two major parts: one part is focused on the human head and neck squamous carcinoma. Increased number of dividing cells, variation in cell size and shape, loss of specialized cell features, and loss of normal tissue organization are the distinguishing traits of a malignant lesion. The alternations in cells can be directly measured utilized AFM. AFM provides detailed characterizations of the cells, including organization of the cytoskeleton and cell elasticity, which are essential for designing a modern selective treatment. The application of ultrasound technique producing external mechanical waves can induce oscillations in cancerous cells leading to the resonance catastrophe, where the resonance frequency is mainly determined by mechanical and morphological properties. The other part is focused on one of the human rare diseases, Progeria. Quantitative comparison of the mechanical properties between progeria and normal dermal fibroblasts can be revealed using AFM. Detailed evaluating biomechanical properties of cells are beneficial in improving the understanding of pathophysiology. The transfection technique is a suggested method that can restore the diseased cells' function. The impact of the human telomerase reverse transcriptase (hTERT) treatment on cells is investigated using AFM to characterize the structural and mechanical properties of fibroblasts. Biomechanics underlies the abilities of the cell, tissue, or whole organ to carry out normal functions in health or to malfunction in disease.

Finally, in the last chapter, a conclusion and an outlook about the remaining questions are provided.

2 Scientific background

The main purpose of this work is trying to quantify and interpret the mechanical properties of cells. With a better understanding of the physical properties of living cells, it may help to explain some of the unclear mechanisms of thorny diseases in this study being cancer and progeria. On the other hand, it would possibly assist in the progress of novel treatment development.

This is a comprehensive issue including biology and physics. In order to clarify all the background information thoroughly, the introduction of this thesis in this chapter illustrates the biological and physical considerations. The fundamental theory of cell biology is emphasized to clarify the pathogeny of specific diseases in section 2.1. Subsequently, physical aspects like scanning probe microscopy, ultrasound technique, and the associated techniques along with their theoretical background are explained in section 2.2.

2.1 Biological background

As we all know that creature is an assembly of billions of cells, in other words, a cell is the unit composing living organisms. Therefore, one could assume that most of the diseases could be attributed to the pathological changes of cells. With the interest of inventing a novel treatment against specific diseases, it is impossible without knowing the cytology. Therefore, in the following paragraph, we will roughly review the eukaryote characteristics, cell cycle, and other cell processes.

2.1.1 Cell Structure of human beings

Parts of the human body are organs. They can be described as tissues that are composed of cells of different types, sizes, and shapes depending on the function. The general structure of a eukaryotic cell is given in Figure 1. A cell consists of three important components: the membrane, the nucleus, and between the two, the cytoplasm.

The cell membrane or plasma membrane is the structure that keeps cytoplasm from leaking out of a cell. The membrane is not a solid structure but consists of phospholipids with embedded proteins. The phospholipids form a lipid bilayer

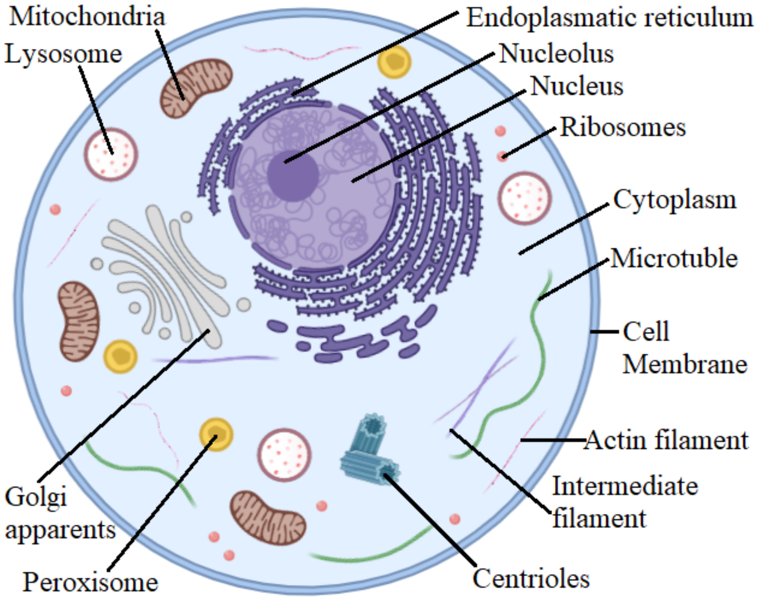

Figure 1: The structure of a eukaryotic cell. A eukaryote is defined as any cell or organism that possesses a clearly defined nucleus. A eukaryotic cell has not only a nuclear membrane that surrounds the nucleus, but also contains a variety of membrane-bound structure (organelles), and are enclosed by a plasma membrane.

that separates the contents of a cell from the extracellular fluid. The lipid bilayer is semi-permeable, only specific molecules can diffuse across the membrane to enter or exit the cell with the help of embedded proteins.

The cytoplasm and cell nucleus are enclosed by the cell membrane. The cytoplasm is the gel-like fluid inside the cell and takes up most of the cell volume. It is the medium for chemical reactions. It provides a platform upon which other organelles can operate within the cell. Several types of membrane-bounded structures called organelles are suspended in the cytoplasm. Some (such as endoplasmic reticulum (ER) and Golgi apparatus) are typically solitary, while others (such as mitochondria, peroxisomes, and lysosomes) can be numerous. Each type of organelles has a definite structure and a specific role in the function of the cell.

ER is responsible for producing most of the proteins and lipids used by other organelles within the cell. There is two types of ER, namely rough ER and smooth ER, rough ER which is studded with protein-synthesizing particles (ribosomes), smooth ER which lacks ribosomes involving in the synthesis of lipids. Ribosomes are found in many places around a eukaryotic cell, they may be attached to the cytoplasmic side of the plasma membrane or the cytoplasmic side of the endoplasmic reticulum and the outer membrane of the nuclear envelope. Ribosomes synthesize the proteins necessary for the cell to work. The Golgi apparatus participates in protein modification, it packages proteins into small membrane-bound vesicles which then translocate to the cell membrane. Lysosomes, the cell's recycling center, contain digestive enzymes ready to destruct protein. Unlike the lysosome, which mostly degrades proteins, peroxisomes contain oxidative enzymes that catabolize fatty acids (lipid destruction) and some chemical toxins. A cell cannot run without energy, the mitochondria are specialized in the production of cellular energy in the form of adenosine triphosphate (ATP). The cytosol is the gelatinous fluid, intercellular fluid, and is the portion of the cytoplasm not contained within membrane-bound organelles, that fills the cell and surrounds the organelles. The cytosol involves signal transduction between the cell membrane and the nucleus and organelles. The cytoskeleton is also located within the cytoplasm, a network of fibers that helps the cell maintain its shape and provide support for organelles. A cell frequently reorganizes its intracellular components leading to a change in its shape. The cytoskeleton is responsible for mediating these changes. By providing tracks with its protein filaments, the cytoskeleton allows organelles to move around within the cell. In addition to facilitating intracellular organelle movement, by moving itself the cytoskeleton can move the entire cells in multi-cellular organisms, in this way, the cytoskeleton is involved in intercellular communication.

The cell nucleus is surrounded by a double membrane with pores that permit the entry and exit of some molecules. The nucleus is the control center of a cell because it maintains integrity and regulates the expression of genes that could control the activities. The nucleus contains all the genetic material, which contains all the genome and controlling factors except for a small fraction of mitochondrial DNA. As well as all the genetic material, there is also a sub-section of the nucleus called the nucleolus, which looks like a nucleus within the nucleus. The nucleolus does not contain the chromosomes. What it contains is the machinery necessary to assemble the cell's ribosomal RNAs.

2.1.2 Cell processes

Cell division and cell death are the two predominant physiological processes that regulate tissue homeostasis in multicellular organisms. Differentiation occurs numerous times during the development of a multicellular organism as it changes from a simple zygote to a complex system of tissues and cell types.

Cell-division cycle The cell (-division) cycle, as illustrated in Figure 2, is a complex sequence of events by which cells grow and divide. Actively dividing eukaryote cells pass through a series of four distinct phases. These phases consist of two gap phases (G1 and G2), the S phase (synthesis), in which the genetic material is duplicated, and the M phase, in which mitosis partitions the genetic material and the cell divides.

Based on the stimulatory and inhibitory messages a cell receives, it decides whether it should enter the cell cycle and divide. Cells use specific proteins and checkpoint signaling systems to monitor and regulate the progress of the cell cycle. When checkpoints are activated, for example by damaged DNA or abnormalities in spindle formation, the cell is forced to undergo programmed cell death or apoptosis, thereby avoiding the propagation of potentially dangerous mutations. However, the cell cycle and its checkpoint systems can be sabotaged by defective genes or protein genes that cause dysregulation of cell cycle checkpoint control, which can lead to human diseases. For example, p53 mutants enable cancer development by allowing oncogene-expressing cells to proliferate unabated. The p53 is a gene that codes for a protein that regulates the cell cycle and hence functions as a tumor suppression.

Regulated cell death (RCD) RCD is a universal process in living organisms that is essential for tissue homeostasis or to restore biological equilibrium following stress. RCD functions to eliminate useless or potentially dangerous cells. Multiple cell death pathways have been classified both on morphological as well as biochemical criteria. Apoptosis and necrosis are two types of cell death.

Both types are different in the initial cause and progression of the cell death pathway. Necrosis is a form of rapid, traumatic, and unprogrammed cell death

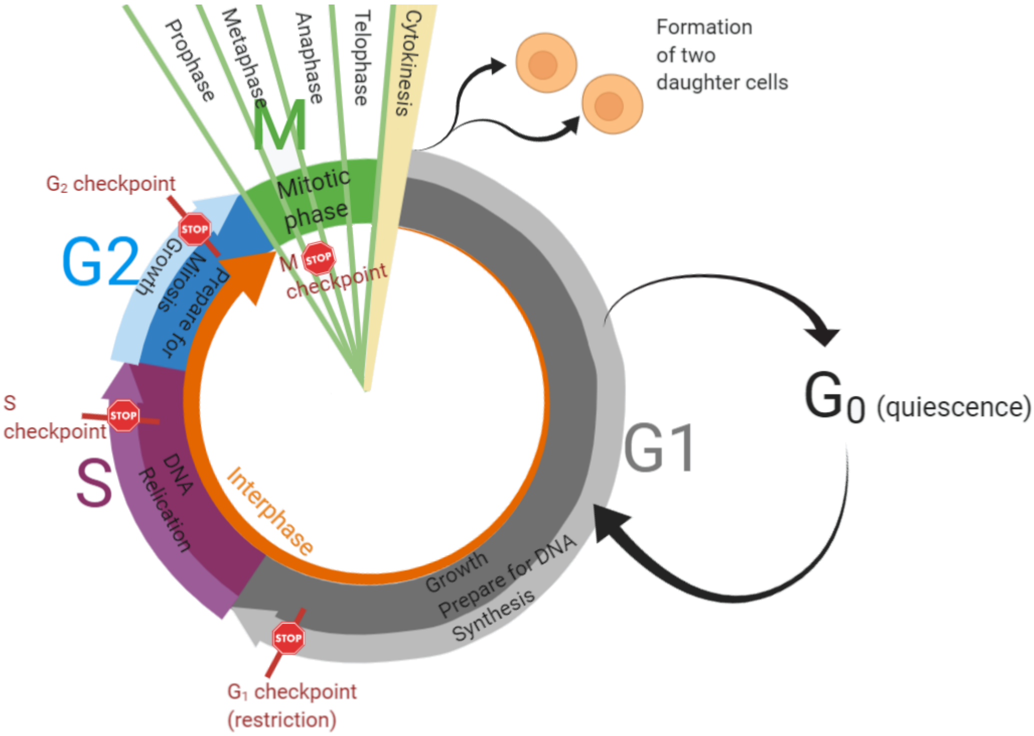

Figure 2: The cell cycle can roughly be separated into two parts: interphase and mitotic (M) phase. Interphase comprises two gap phases (G1 and G2); and S (for synthesis) phase, in which the cell grows and replicates its genetic material. M phase consists of two tightly coupled processes: mitosis, in which the cell nucleus divides, and cytokinesis, in which the cells cytoplasm, divides producing two new, identical cells.

that results from internal or external stresses such as mechanical injuries, chemical agents, or pathogens. During necrosis, the inability of the cell to maintain homeostasis is followed by an influx of water and other extracellular ions. This results in disruption of cell organelles, such as swelling of the ER and mitochondria, or decay of the Golgi apparatus, followed by lysis of the cell. As a result, cellular contents are released into the extracellular fluid, eliciting an immune response (inflammatory). Necrosis is unable to account for the normal physiological death of cells ongoing within a multicellular organism. Unlike necrosis, apoptosis is a form of programmed cell death that occurs in multicellular organisms. Apoptosis is a highly regulated and controlled process that confers advantages during the lifecycle of an organism. However, many pieces of evidence have suggested that dysregulation of this programmed cell death is closely related to several human diseases such as cancer, neurodegenerative disorders, autoimmune disorders, infectious diseases including AIDS [4].

Apoptosis depends on the activation of caspases that will then cleave some substrates resulting in the biochemical and morphological changes typical of this form of death. Characterizations of apoptosis include morphological changes and energy-dependent biochemical cascades (signaling pathway). It was found that biological apoptosis signals and biomechanical remodeling have an effect on each other during apoptosis. Disruption of the actin cytoskeleton, which is trigged by cytochalasin B (microfilament-inhibit drug), rapidly causes the decrease in cellular elasticity and volume, and the increase in cell surface roughness and intercellular crowding, ultimately leading to apoptosis [5].

The regulation of the cell cycle and programmed cell death represent major advances in biomedical research during the past several decades. It is becoming increasingly clear that dysregulation of either cell cycle or cell death is important in the pathogenesis of various diseases [6].

Cell differentiation Cellular differentiation occurs in the human fetal pituitary between the eighth and sixteenth weeks of gestation. Differentiation is a developmental process by which unspecialized cells change into specialized cells with distinctive structural and functional characteristics. Through differentiation, cells develop into tissues and organs. For mammals, totipotent is capable to differentiate into any type of cell, includes the zygote and products of the first few cell divisions. Certain types of cells can differentiate into many types of cells. These cells are known as pluripotent or stem cells in animals. Stem cells are important because they retain the capacity to differentiate into nearly all cell types in the body. This makes them very special in that they can differentiate and be used for given treatment purposes. Cell differentiation is important to the study of cancer because a cell's degree of differentiation is associated with its ability to proliferate.

Dedifferentiation is a process by which cells develop in reverse, from a more differentiated to a less differentiated state, usually as part of a regenerative process. When exposed to appropriate signals, certain mammalian cell types can be induced to dedifferentiate to progenitor cells and generate different types of functional cells for the repair of damaged tissues. However, scientists still have been puzzled about the mechanism of dedifferentiation, whether these dedifferentiation-derived progenitor cells or stem cell-like cells, could perform the same functions as embryonic or adult stem cells isolated from the body. Dedifferentiation is probably to become a new focus in stem cell research because of its importance in fields such as stem cell biology, regenerative medicine, cancer research, and aging [7].

2.1.3 Cell mechanics

Cell mechanics represents a comprehensive variable of life. Cellular elasticity is an integrative parameter summarizing the biophysical outcome of many cellular processes. This includes intracellular signaling, cytoskeletal activity, changes of cell volume and morphology, and many others. Not only intracellular processes defines a cell's elasticity but also environmental factors like their biochemical and biophysical surrounding.

Cytoskeleton The ability of a eukaryotic cell to resist deformation, to transport intracellular cargo, and to change shape during movement depends on the cytoskeleton. The cytoskeleton is now known to consist of hundreds of different (associated) proteins cooperating in the organization of the complex machinery that is involved in essentially all structural and dynamic aspects of living cells, including maintenance of cell shape, cell movement (motility), cell replication, apoptosis, cell differentiation, and cell signaling. Aberrant control of cytoskeletal signaling, which can result in a disconnection between extracellular stimuli and cellular responses, is often seen in immune pathologies, developmental defects, and cancer.

The cytoskeleton is a major regulator of intracellular mechanics. The cytoskeletal components of actin, microtubule, and intermediate filaments (Figure 3) interact with each other in complicated ways and are connected to other components, such as actin-binding proteins and integrins. The thickest of the three is the microtubule, a structural filament composed of subunits of a protein called tubulin. Microtubules maintain cell shape and structure, help resist compression of the cell, and play a role in positioning the organelles within the cell. In contrast to microtubules, the microfilament is the smallest type of cytoskeletal filament, and is made of a protein called actin. Actin fibers constitute a large component of muscle tissue and, along with the protein myosin, are responsible for muscle contraction. The final cytoskeletal filament is the intermediate filament. An intermediate filament is a filament intermediate in thickness between the microtubules and microfilaments and is constructed from many different subunit proteins. Unlike the microtubules, which resist compression, intermediate filaments resist tension (the forces that pull apart cells).

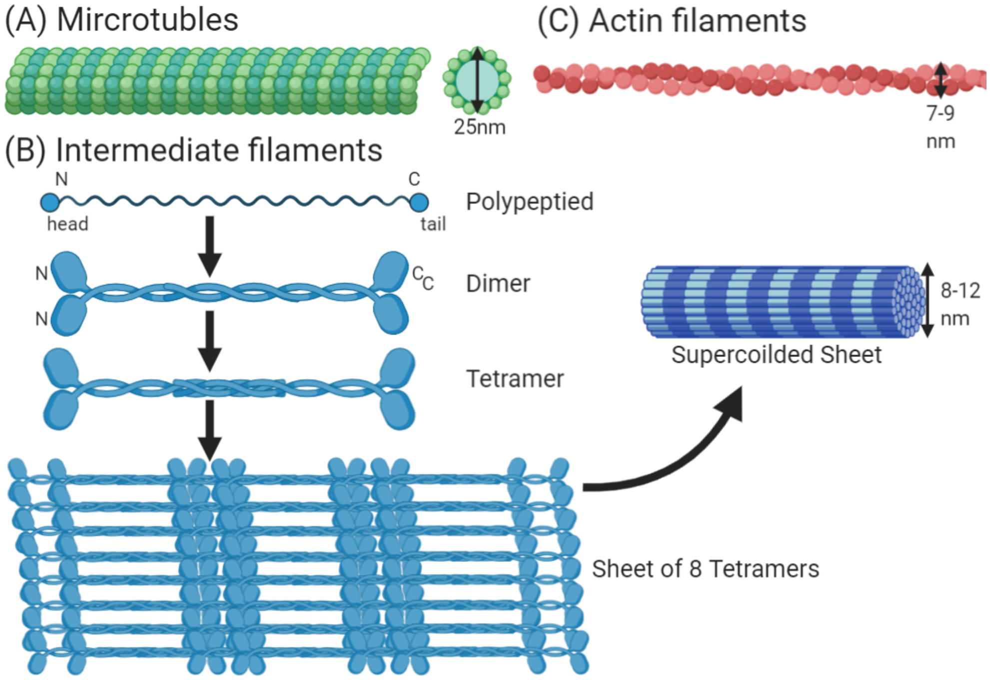

Figure 3: Three main components of cytoskeleton: (A) microtubules (tubulin polymers) (B) intermediate filaments (C) microfilaments (actin filaments). Among these fibers, microtubules are the thickest hollow fibers with a diameter of 25 nm, and double-stranded microfilaments being the thinnest have a diameter of 7 to 9 nm. Intermediate filaments are rope-like and fibrous with a diameter of approximately 10 nm.

Mechanotransduction Living cells are sensitive to mechanical forces from the microenvironment and transduce physical force-induced signals into biochemical and biological responses, a process is known as mechanotransduction. The ability of cells to respond appropriately to extracellular signals also depends on the regulation of signaling pathways themselves. Multiple signal pathways can potentially mediate intercellular mechanotransduction either directly or indirectly, leading to appropriate remodeling response to achieve tissue homeostasis [8].

The primary site of force transmission to the cell is the cell surface, where the extracellular matrix (ECM) is. Major components of ECM are different types of proteins and carbohydrates, and this complex system is found outside of the plasma membrane and connects to cytoskeletal fibers and transmembrane proteins [9]. One common pathway for force transmission is via the focal adhesions (FAs). FAs are integrin-containing (multi-protein structures) severe as an interface, that forms mechanical links between intracellular actin bundles and the ECM, and integrins form bonds with various extracellular proteins such as fibronectin or vitronectin, which constitute a primary pathway for intracellular force. On the intracellular side, many proteins tend to localize to focal adhesions, these include paxillin, focal adhesion kinase (FAK), and caveolin. Other proteins have been identified that link integrins to the actin cytoskeleton, having binding domains for both integrin and actin. FA-related signaling network controls the organization of the actin cytoskeleton. FAs act as mechanosensory machines, they self-assemble and elongate proportional to the applied force and induce signal cascades leading to actin polymerization (strengthening) [10]. Actin cables associated with adherens junctions at cell-cell contacts and provide a physical mechanism for cell-generated contractile forces to act upon cell-cell adhesions [11]. The cytoskeleton spans the entirety of eukaryotic cells, providing structural support and integral tension, therefore its key role in mechanotransduction processes is unsurprising.

It is now clear that cells transduce mechanical force by using a variety of mechanisms. There are several approaches for mechanically probing groups of cells to study the response of cells to mechanical cues. These methods are optical traps [12, 13], magnetic tweezers [14, 15], micropipette aspiration [16, 17], and atomic force microscopy [18, 19], and so on. The diverse methods of mechanically stressing cells and the basic understanding of some of the molecular components thought to be physically involved in mechanotransduction may lead to an increased understanding of relevant physiological processes.

2.1.4 Dysregulation of cell processes

In body tissues, normal cells can reproduce correctly, stop reproducing when necessary, remain in a specific location, become specialized for specific functions, and self-destruct when necessary. The rates of new cell growth and old cell death are kept in balance. However, when there is a change in DNA or damage to it, a gene can mutate. Gene mutations can disrupt the normal balance between cell division and cell death leading to diseases. Mutations can lead to changes in the structure of an encoded protein or a decrease or complete loss in its expression causing dysregulation. Dysregulation of the cell cycle and cell death processes play an important role in the pathogenesis of major diseases, including cancer, stroke, atherosclerosis, infection, inflammation, and neurodegenerative disorders as well as in the rare disease Progeria [6]. The development of new novel approaches for the treatment of various conditions associated with abnormalities in the regulation of cell cycle progression or cell death, however, is hindered by limited knowledge of the pathogenic mechanisms that lead to the development of the sporadic form of the disease.

Cancerous cells Cells divide only when they receive the proper signals from growth factors that circulate in the bloodstream or from a cell they directly contact. Many processes are involved in growth, reproduction and all these processes have to take place correctly for a cell to divide properly. If anything goes wrong during this complicated process, cells become faulty and start growing uncontrollably and form a tumor. Cancer is a genetic disease losing or perturbing many of the characteristics of normal cell behavior. Acquiring a series of mutations (damaged in DNA) make cancer cells divide more quickly, escape internal and external controls on division, and fail to undergo programmed cell death [20]. Different types of cancer involve different types of mutations, and each tumor has a unique set of genetic alterations. The most frequently altered gene in human tumors is TP53, encoding the p53 protein. Cells in which p53 is deleted or mutated lose the G1 checkpoint can avoid DNA damage-induced cell death. However, many cancers are not only linked with one specific gene. Instead, cancer likely involves multiple gene mutations. On the other hand, environmental exposures can modify gene expression and influence cell properties. It is also crucial to clarify the interactions between the organism and environmental factors in order to understand the gene-environment interplay for human health and the development of diseases.

Progeria cells Progeria, also known as Hutchinson-Gilford progeria syndrome (HGPS), is a rare, fatal genetic disorder with features of premature aging. Progeria is caused by a mutation in the human lamin A gene (LMNA) that induces changes in the nuclear architecture of patient cells [21]. The instability of nuclear limits the ability of cell division. Lamin A is localized to the nuclear lamina at the inner side of the nuclear envelope, contributing to nuclear structural stability and other nuclear functions. A mutant lamin A protein called progerin is associated with the inner nuclear membrane and affects the dynamics properties of lamins. Progerin overexpression causes a premature aging disorder. HGPS is a severe disorder that disturbs several organ systems leading to hair loss, decreased adipose tissue, increased bone fractures, short stature, hardening of arteries, and severe atherosclerosis (heart diseases). Most children suffering from Progeria die of heart attacks or strokes at an average age of fourteen years. At this time, there is still no cure or no effective treatment.

2.1.5 Cells and tissues

Most organs contain all four tissue types: epithelial tissue, connective tissue, muscle tissue, and nervous tissue. Among them, epithelial tissue plays a major role in maintaining health and homeostasis or balance within the body. Epithelial cells are the cells that cover the inside and outside surfaces of the body that act as a protective barrier. Epithelial cells cover a person's skin, but they also occur along the surfaces of the digestive tract, the internal organs, and blood vessels. There are many types of epithelial cells (Figure 4). Epithelial cells are classified into various groups according to two features (the shape of the cells and the number of cell layers): squamous (flat plate-like; wider than high), cuboidal (height and width similar), columnar, stratified squamous, stratified cuboidal, stratified columnar, pseudostratified (pseudo- = false) columnar, and transitional epithelium.

Epithelial tissues form the external surface of the body and line the cavities of most internal organs. Epithelial tissue is also the most common site for the development cancers. Carcinomas arise from epithelial tissue and account for as many as 90 percent of all cancer cases.

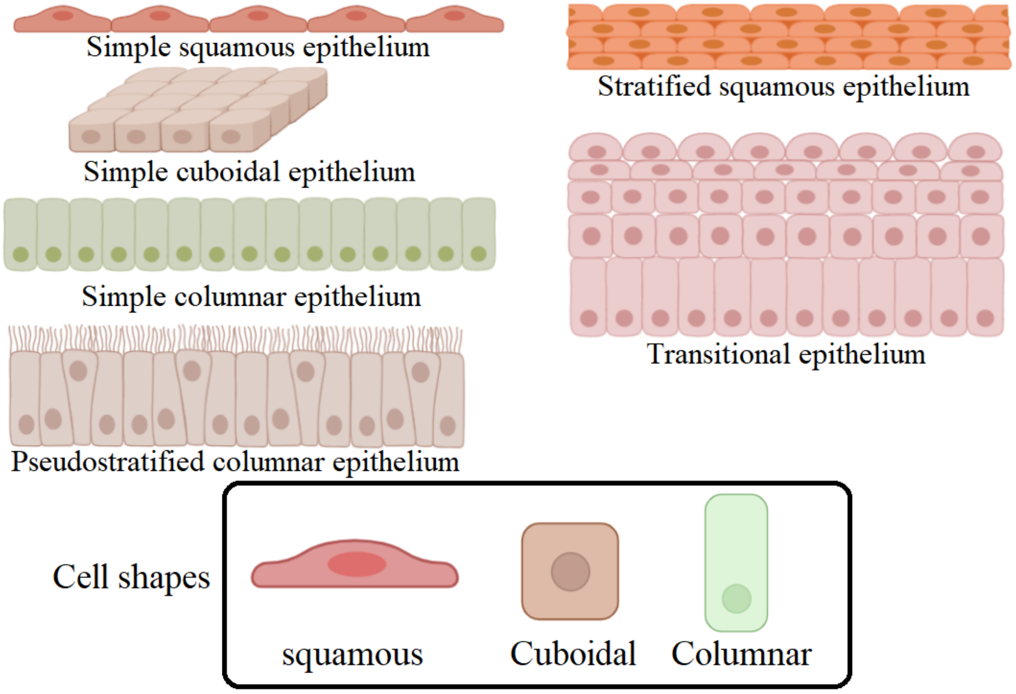

Figure 4: Different types of epithelial cells: simple squamous epithelium; simple cuboidal epithelium; simple columnar epithelium; pseudostratified columnar epithelium; stratified squamous epithelium; transitional epithelium. They are categorized according to cell shape and the number of cell layers.

Alternations of cancerous cells Cancer is a disease, which was suggested that starts with genetic alternations in one cell or a small group of cells. However, not every change in the body's tissues is cancer. Some tissue changes may develop into cancer if they are not treated. Here are some of the changed tissues that have the potential to become cancer: hyperplasia and dysplasia. In hyperplasia, there is an increase in the number of cells in an organ or tissue that appear normal under a microscope. In dysplasia, the cells look abnormal under a microscope but are not cancer. As long as there are very few abnormal cells and they are kept under control by the human immune system, they will not turn into cancer. Only when they keep on changing and start to divide quickly and grow uncontrollably compared to normal cells, they may form a lump called a tumor. Tumors grow and behave differently depending on whether they are cancerous (malignant), noncancerous (benign), or precancerous. A simplified scheme of cancer progression is presented in Figure 5. A malignant tumor can invade surrounding normal tissue and spread throughout the body via the circulatory or lymphatic systems. When cancer cells break away from where they first formed (primary cancer), travel through the blood or lymph system, and form new tumors (metastatic tumors) in other parts of the body, the new tumor is called metastases.

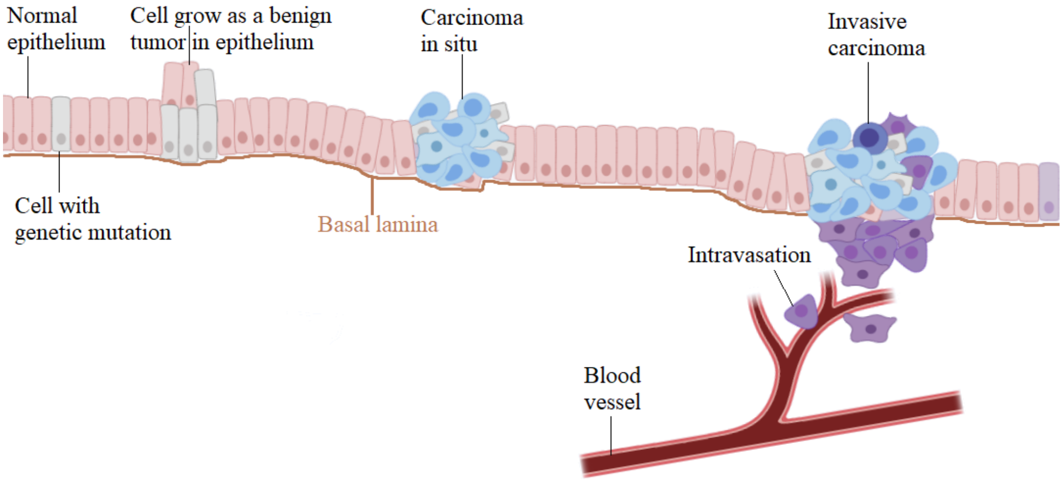

Figure 5: Simplified scheme of cancer progression. First, the tumor begins to develop with a mutation that makes the cell more likely to divide. The altered cells and their daughter appear normal, but they grow and divide too much. After some point, one of these cells experiences another mutation that results in some loss of growth on cell control. This cell's daughter divides very fast and looks abnormal in stage and orientation. Again, after some time, one of these cells experiences another mutation that alters cell behavior. These cells and their descendants become ever more abnormal and can break through basal lamina and invade capillary.

The Tumor Node Metastatic (TNM) classification of malignant tumors is a globally recognized standard for classifying the extent of the spread of cancer. It is a classification system of the anatomical extent of tumor cancers. The classification into different stages is based on three criteria: the characteristics of the size of the tumor at the primary site (T), the degree of local or regional lymph nodes involvement (N), and the presence of distant metastases (M). The TNM staging system is an important tool for clinicians to categorize tumors in a specific manner to assist with the assessment of disease status, prognosis, and management.

In many tumors, matrix and tissue mechanics are altered and tissue stiffness is associated with increased malignancy and metastasis. The structure of the cytoskeleton and ECM are transformed by cancer. And the altered protein structure also changes the ability of cancer to contract or stretch, by influencing their mechanics of deformation. As a result, the motility of cancer cells can be very different from those of normal cells, causing them to migrate through the tissue to different sites in the human body and inducing tumor metastasis. The assessment of the elasticity of cancer cells may allow a more accurate clinical stage and prognosis estimation that may also contribute to future therapy.

Alternations of Progeria cells LMNA (Lamin A/C) is a human protein that is encoded by the LMNA gene. Lamins and their associated proteins form a dense filamentous meshwork (nuclear lamina) underlying the inner nuclear membrane [22]. Nuclear laminas provide mechanical rigidity to the nucleus and maintain shape. Lamins are also thought to provide an anchoring site at the nuclear periphery for interphase chromatin [23].

LMNA mutations affect cardiac tissue, muscle tissues, adipose tissues to precipitate several diseases collectively termed as laminopathies. Different LMNA mutations cause rare clinical disorders that affect striated muscle, adipose, peripheral nerve, or multiple systems with features of accelerated aging [24]. Hutchinson-Gilford progeria syndrome (HGPS) is a rare precocious aging syndrome caused by mutations in LMNA that lead to the synthesis of a mutant form of prelamin A, generally called progerin. Progerin, a mutation in lamin A, affects lamin filament assembly and induces profound changes in nuclear architecture, gene instability, and function, promoting cellular senescence [21]. Another type of mutant lamin A namely, E145K-lamin A, also causes HGPS. E145K-lamin A induces profound changes in nuclear architecture and alterations in the cellular actin network [25].

2.2 Physical background

The mechanical characterization of biological samples is a fundamental issue in biology and related fields, such as tissue and cell mechanics, regenerative medicine, and diagnosis of diseases. Several existing methods are used to access the load-deformation behavior of different biosamples. With detailed biomechanical testing results (displacement or deformation), the biomechanical and biophysical performance of living cells can be revealed, and the effect of the pathological process on cell mechanics can be further predicted. Besides, with the quantitative mechanical characterization of cells, the suitable parameters of ultrasound, a potential selective ablation therapy, can be implemented. The fundamental knowledge of these apparatuses which are utilized in this study will be explained in detail in this chapter.

2.2.1 Single-molecule force spectroscopy

Single-molecule experiments are direct measurements of one molecule at a time. These different technological approaches used for pursuing a realistic description of materials' mechanical behaviors are atomic force microscopy (AFM) [18, 19], optical tweezers (OTs) [12, 13], magnetic tweezers (MTs) [14, 15]. AFM is a well-established technique, has advantages such as an easy adjustment to liquid environment, repeatability, and precise force determination. AFM can be used to create a high-resolution image of surface topography and to study the mechanical properties of biomolecules precisely, it has nevertheless limited use for examining small forces because its sensitivity is strictly dependent on the laser beam properties and the mechanical property of the probe. The motion of the AFM tip as it scans along the sample surface is monitored through a laser beam reflected off the cantilever. In contrast, OTs and MTs are very sensitive to weak forces. OTs technique is based on trapping small particles using forces generated by laser radiation pressure, however, the meanwhile, the sample is heated [12, 13]. MTs do not interface with molecules and can be applied from a few piconewtons to several nano newtons by using a magnetic field gradient to manipulate the magnetic beads attached to the cells [14, 15]. In typical magnetic tweezer experiments, a molecule of interest is tethered to a glass coverslip on one end and a magnetic bead on the another end. The main advantage of OTs is the ease with which single beads can be manipulated and carried around. On the contrary, MTs are at their best when working with a homogeneous force field. The three methods described above have their respective merits, but AFM can function perfectly in ambient air or even an aqueous environment, which allows the investigation of biological macromolecules and even living organisms. AFM is one of the only tools available for quantitative live-cell imaging while measuring the elastic and viscoelastic responses of cells to mechanical stimuli. Therefore, in this study, we only focus on the use of AFM.

2.2.2 Atomic force spectroscopy

AFM, also known as scanning force microscopy (SFM), is the most familiar technique among the available force spectroscopy. AFM is also the most popular type of scanning probe microscopy (SPM) and it was initially developed to overcome the limitation of the scanning tunneling microscope (STM) in imaging non-conductive samples in 1986 by Gerd Binnig [26].

AFM allows spatial and temporal control of samples, as well as highly quantitative force actuation and force measurement that is sufficiently sensitive to characterize the interaction of single molecules [27]. The operation conditions of the AFM are flexible, from vacuum to air to liquid media at reduced or elevated temperatures. Besides, AFM has been a powerful tool to integrate with different optical microscopy techniques, especially regarding the biosciences field, allowing to overcome some of its individual limitations, for instance, sample penetration and biological specificity. In this regard, AFM has been combined with confocal fluorescence-correlation spectroscopy, wide-field fluorescence, total internal reflection fluorescence, and confocal microscopy. A correlative microscopy approach is beneficial as it allows to pair up the high spatial resolution and mechanical characterization potential of an AFM, with the additional molecular information available, through various fluorescent markers or immunostains [28].

Principle of operation The AFM principle is based on the tip-cantilever assembly that interacts with the sample; this assembly is also commonly referred to as the probe. The schematic set-up of the system is shown in Figure 6. A typical AFM consists of a cantilever with a small probe at the end of the cantilever, a laser, a four-quadrant photodiode, and a scanner (Figure 6(A)). A laser beam is focused onto a cantilever and reflects from it onto a set of position-sensitive photodiodes. While the tip of the cantilever moves over the sample, the cantilever itself bends due to the interaction with the surface and the photodiodes register the resulting position changes of the laser reflection. Two piezos (a piezoelectric element expands or contracts in direct proportion to an applied electric field) generate the scanning movement of the cantilever, laser, and photodiodes in x- and y-direction. The signal from the photodiodes goes to a z-piezo, that moves the cantilever up or down to compensate for the cantilever deflection. The information of the deflection is used to generate a detailed image of the 3-D topography of the sample. Combining AFM with optical microscopy as illustrated in Figure 6(B), cells can be therefore positioned to assess cellular interactions at a given location on a functionalized surface, tissue, or on another cell.

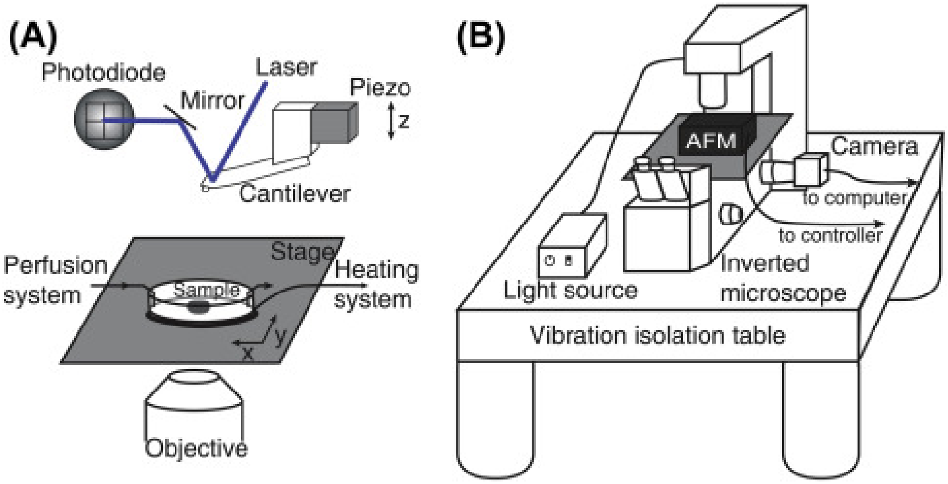

Figure 6: Schematics illustration of the principle of an atomic force microscope. (A) An animal cell is positioned by an x-y-z piezo scanner, while a colloid (or a square pyramidal silicon nitride) attached to an AFM cantilever is brought into contact with the cellular surface. Then, nanomechanical mapping of the sample is performed by a probe consisting of a flexible cantilever and a tip. (B) AFM scan head (x-y-z) and sample positioning stage (x-y) are mounted on the inverted optical microscope. Laser spot alignment of the AFM is accomplished using a standard monochrome CCD camera [29].

In the indentation pushing experiment, the AFM probe is indented against the sample while recording its response through a force-distance curve (or force-indentation curve), which represents the deformation of the cantilever given a prescribed force, or the required force to push the tip to a certain depth into the sample. The recorded curve can be used to calculate the sample's stiffness by data processing algorithms that take into account several parameters, such as the geometry of the tip and the depth of indentation.

When the tip comes very close to the sample, attractive and repulsive forces due to the interactions between the tip and the sample cause a negative or positive bending of the cantilever. The generated force is dependent on the spring constant of the cantilever and can be characterized by Hooke's law (1).

$$F = k \cdot x \tag{1}$$

where

F is the spring force (usually 0.1 to 1 N/m)
k is the spring constant
x is the spring stretch or the compression
(if the spring constant is smaller than that of the surface, the cantilever bends. This bending is detected by the deflection of the laser.)

AFM can be used to measure local elastic and viscoelastic properties of soft matter samples like biological cells. AFM force spectroscopy refers to single-point measurements in which the cantilever approaches and pokes into the sample and then withdraws. During the measurement, the cantilever deflection vs. piezo movement is measured, and this can ultimately be converted to a force vs. tip-sample separation measurement that provides mechanical information about the sample. This conversion requires the calibration of the spring constant and deflection sensitivity. The Hertz and Sneddon models of contact mechanics are usually adopted to extract the elastic modulus by analyzing the force-indentation curves for spherical and conical tips, respectively (Figure 7). The Hertz model describes the elastic deformation of two spheres as follows:

$$F = \frac{4}{3} \cdot \frac{E}{1-\upsilon^2} \cdot \sqrt{R} \cdot \delta^{\frac{3}{2}} \tag{2}$$

where

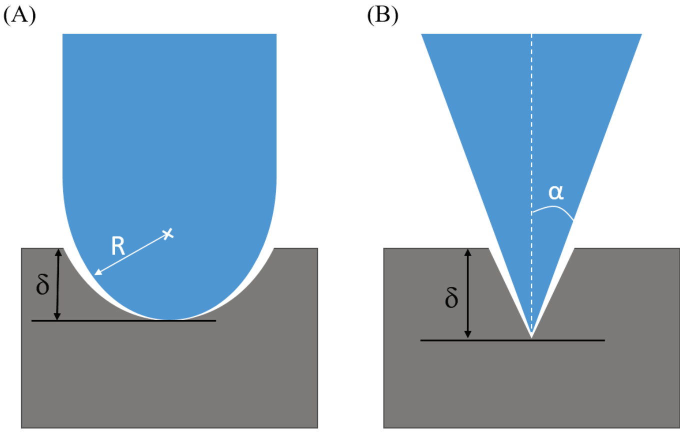

Figure 7: Two different contact models between cell and tip have been proposed in order to properly account for different geometries: (A) Spherical probe contacting semi-infinite half-space in the Hertz model. R indicates the radius of the probe (B) Conical probe indenting semi-infinite half-space in the Sneddon model, where α represents the angle between the half-space surface and the outside of the cone. δ indicates indentation.

F is the indentation force
E is the Young's modulus
R is the radius of the probe
υ is the Poisson's ratio (typically 0.2 - 0.5)
δ is the indentation depth

The Sneddon model represents the elastic deformation of conical or paraboloidal tips on a flat sample:

$$F = \frac{2}{\pi} \cdot \frac{E}{1 - \upsilon^2} \cdot \tan\alpha \cdot \delta^2 \tag{3}$$

where

F is the indentation force
E is the Young's modulus
α is the half-angle of the probe
υ is the Poisson's ratio (typically 0.2 - 0.5)
δ is the indentation depth

Tip-sample interactions With AFM, one can measure the force between atoms at the tip and the sample which are located as close as 0.1 to 100 nm. The forces which interact at the atomic scale, have been classified as short- or long-range forces, attractive or repulsive. A typical graph of the Lennard-Jones potential is depicted in Figure 8: over a short distance the forces are repulsive due to overlapping electron orbits (e.g. Pauli repulsion); whereas at longer distances, the forces are attractive (e.g. Van-der-Waals force or dispersion force). The Lennard-Jones potential (4) provides a qualitative description of the tip-sample interaction in AFM, as seen below:

$$V(r) = 4\varepsilon((\frac{\sigma}{r})^{12} - (\frac{\sigma}{r})^{6}) \tag{4}$$

where

ε is the depth of the attractive well
r is the spring stretch or the compression
σ is the interparticle distance where the sign of the potential change

Modes of Operation Depending on tip-sample separation during scanning, three modes of an atomic force microscope are available: contact mode, intermittent (tapping) mode, and non-contact mode (Figure 9).

Contact mode is also called static mode where the probe does not oscillate and is in continuous contact with the sample surface. Problems with the contact mode are higher wear rate and failure of the tips during scanning caused by excessive forces. When exploring vulnerable biological samples, they can be destroyed by scratching because the probe scanning tip is in direct contact with the surface.

Tapping mode is a dynamic mode also called intermittent contact or semi-contact mode and is where the probe oscillates such that the tip only comes back-and-forth contact with the sample at the bottom of its oscillation. By maintaining a constant oscillation amplitude a constant tip-sample interaction is maintained. The disadvantages of tapping mode are slower scanning rates than in contact mode and tapping of the sample, which might be a problem for soft matter samples. Operation tapping mode in liquids, the fluid medium tends to damp the cantilever's

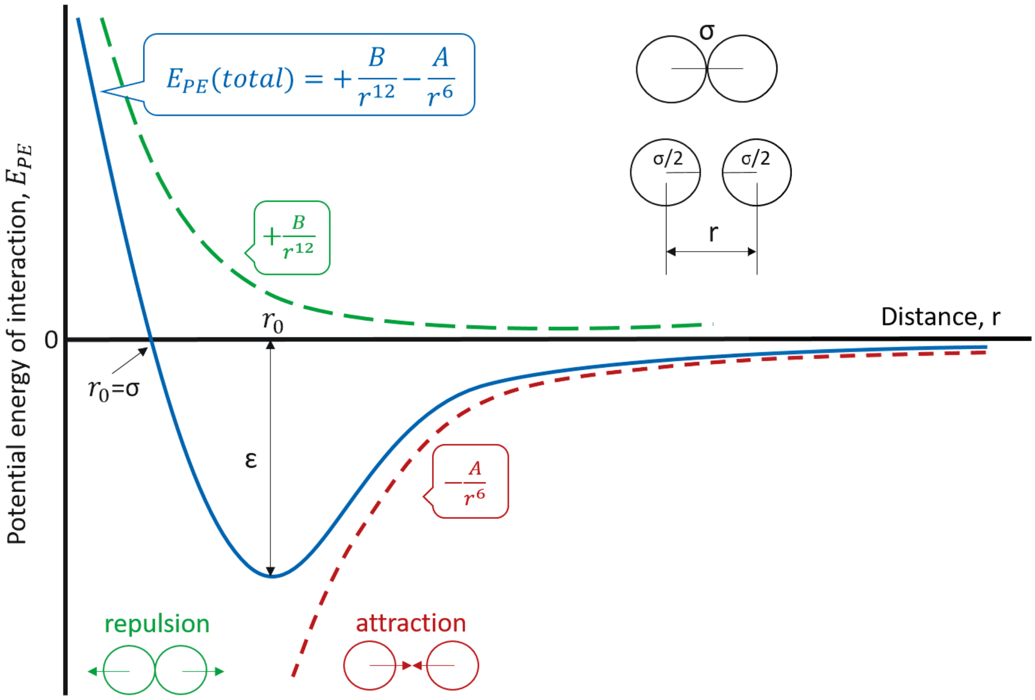

Figure 8: Lennard-Jones potential describes the intermolecular forces between particles using the Lennard-Jones potential curve

normal resonant frequency. In this case, the entire fluid cell can be oscillated to drive the cantilever into oscillation.

Non-contact is also a dynamic model where the probe is vibrated above the sample without the tip coming into very close contact with the surface. However, it is a very challenging technique, and one misstep in setting the feedback will crash the tip quite spectacularly. It is also usually best to do this in a vacuum, adding to the complexity.

Different parts of the AFM force-distance curve (Figure 9) are used for different experiments. In stiffness measurements, the data recorded during the tip approach is used. On the other hand for adhesion experiments, data recorded during tip retract is used.

2.2.3 Ultrasound

Ultrasound waves are kind of sound waves with frequencies beyond 20 kHz, making them undetectable for the human ear. There are usually three characteristics of

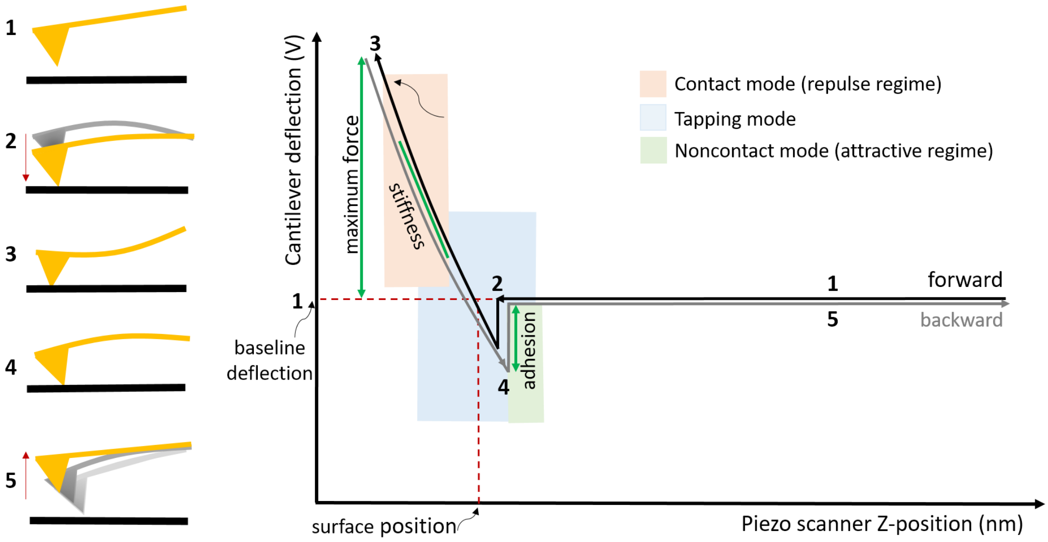

Figure 9: Schematic representation of typical approach force-versus-distance curves on a soft sample. The force curve can be divided into different segments where the black line (1 - 3) refers to motion where the tip is approaching the surface, and the gray line (3 - 5) is when the tip is retracting from the surface. The tip of the cantilever is initially distant from the sample to which it is brought into contact. During retraction of the AFM tip, adhesive events may occur at different distances due to interactions between tip and sample.

ultrasound waves: frequency, wavelength, and velocity. Frequency is the number of times a particle experiencing a complete compression and decompression cycle in one second. Wavelength is the distance between two equivalent points on the waveform in a particular medium. Velocity is the velocity at which the wave travels through the medium.

Mechanical vibration (ultrasound) at increasing frequencies is known as sound energy. Acoustic waves can produce a variety of biological effects in tissues through either thermal or non-thermal physical mechanisms. Ultrasound exposures used for diagnostic imaging are designed to minimize the interactions of the sound field with the tissue, whereas therapeutic applications of ultrasound depend on the direct interaction of the sound field with the tissue to produce biological effects. Currently, ultrasound is used widely in medicine as both a diagnostic and therapeutic tool. Different medical applications of ultrasound were classified according to ultrasound intensity or frequency [30].

Piezoelectricity Piezoelectricity is the ability of certain crystals to generate an electric charge in response to applied mechanical stress and vice versa. Figure 10 shows a simple molecular model; it explains the generating of an electric charge as the result of a force exerted on the material. Before subjecting to some external stress, the charges in the piezoelectric crystal are exactly balanced, the external effect of the charges is reciprocally canceled. As a result, the piezoelectric crystal is electrically neutral. After exerting some pressure on the crystal, its internal structure can be deformed, causing the separation of the positive and negative gravity centers of the molecules and generating little dipoles. Eventually, the facing poles inside the material are mutually canceled, a distribution of a linked charge appears on the surfaces of the materials. That is to say, the material is polarized. The polarization generates an electric field and can be used to transform the mechanical energy of the material's deformation into electrical energy. The piezoelectric effect is reversible, piezoelectric materials always exhibit both the direct piezoelectric effect and the inverse piezoelectric effect.

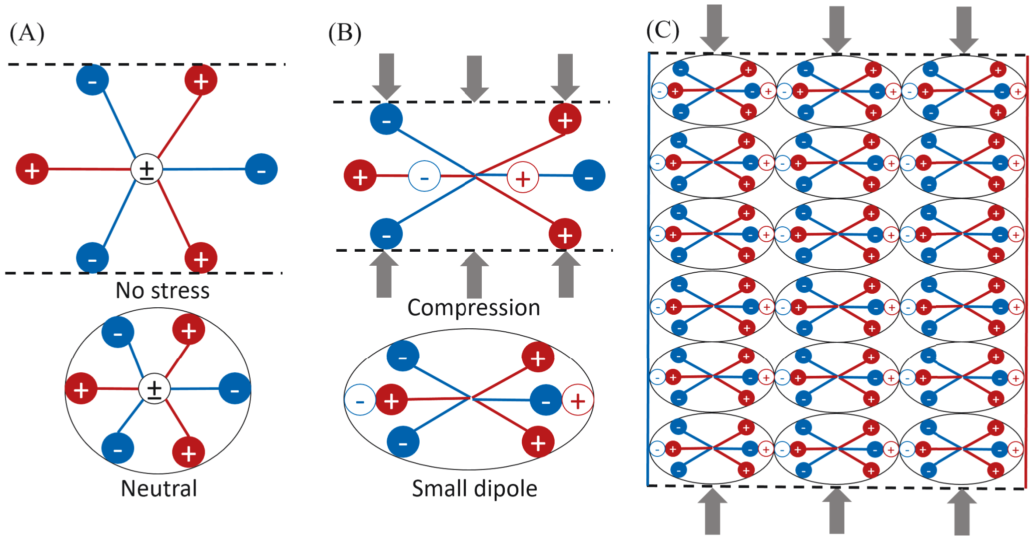

Figure 10: Simple molecular model for explaining the piezoelectric effect: (A) unperturbed molecule; (B) molecule subjected to an external force, and (C) polarizing effect on the material surfaces

Piezoelectric ceramics are the materials for generating and detecting ultrasonic waves. Charge carriers are shifted in piezoelectric materials under the influence of an electric field, which leads to a macroscopic change in length (inverse piezoelectric effect). If the applied voltage is alternating, the particles in the medium, e.g. in the air, start to vibrate. Pressure fluctuations occur. Rarefaction of the particles leads to lower pressure and compression to increased pressure. The wavelength of the sound describes the distance between two decompression or compression areas. The resulting sound waves propagate in the surrounding medium. The speed of the sound varies according to the density and the elastic properties of the medium.

Biological effects Diagnostic ultrasonography has provided a wealth of knowledge in medicine with millions of ultrasound examinations performed each year. Ultrasonography remains one of the fastest-growing imaging modalities due to its low cost and real-time image display. However, ultrasound exposure may produce harmful biological effects depending on a variety of acoustic exposure parameters [31]. The biological effects of ultrasound refer to the potential adverse effects the imaging modality has on human tissue. These are primarily via two main mechanisms: thermal and mechanical.

Due to the law of the conservation of energy, all of the sound energy attenuated by tissues must be converted to other forms of energy. The majority of this is turned into heat. As such, it is possible for an ultrasound to raise tissue temperature by up to 1.5 °C. For sensitive tissues, this temperature rise may have deleterious effects if present for an extended period.

When high-intensity ultrasound is coupled into liquid, acoustic cavitation occurs. Acoustic cavitation is known as the phenomenon in which rapid changes of pressure in a liquid lead to the formation of small vapor-filled cavities in places where the pressure is relatively low. These cavities are called bubbles or spherical voids. As the liquid compresses and decompresses, the cavitation bubbles can behave in two ways: stable cavitation, stable bubbles are formed at relatively low ultrasonic intensity; transient (inertial) cavitation, where transient bubbles are formed using high-intensity sonication. A stable bubble does not collapse but moving forth and back in a fluid, therefore potentially causing the surrounding medium to flow (i.e., stream). The transient cavitation, the process in which a bubble in a liquid rapidly collapses, produces a shock wave. Transient bubbles' collapsing is considered to be the main source of the chemical and mechanical effects of ultrasonic energy [32]. The collapsing bubble can be considered as a microreactor in which temperatures of several thousand degrees and pressure higher than one thousand atmospheres are created instantaneously.

When cavitation bubbles oscillate and collapse, several physical effects are generated, namely, shock waves, microjets, turbulence, shear forces, etc. These effects can be used for a number of applications including emulsification, extraction, cleaning, etc. The collapse of the acoustic cavitation bubbles is also near adiabatic and generates temperatures of thousands of degrees within the bubbles for a short period [33]. These bubbles generate very high energies to adjacent tissue. This can increase tissue temperature by more than 1000 °C. The effect can be used as treatments, e.g. for tumor ablations and facial aging.

High-intensity *focused* ultrasound (HIFU) has been used for clinical treatment of a variety of solid malignant and benign tumors, including those in the pancreas, liver, kidney, bone, prostate, and breast, as well as uterine fibroids and soft-tissue sarcomas [34]. HIFU is a high-intensity ultrasound beam brought to a tight focus, enhancing both thermal and non-thermal effects, and destroy all cells lying within the focal volume [35]. This makes ultrasound an excellent non-invasive tumor ablation technique for deep-seated targets within the body by causing tissue necrosis through the conversion of mechanical energy into heat (up to 80 °C or 90 °C within tissues).

Low-intensity pulsed ultrasound (LIPUS) is a form of ultrasound that si delivered at a much lower intensity ($<3\,\mathrm{W/cm^2}$) than traditional ultrasound energy and output in the mode of the pulse wave, and it is typically used for therapeutic purpose in rehabilitation medicine [30]. Because LIPUS has minimal thermal effects due to its low intensity and pulsed output mode that attract the attention of researchers. LIPUS has been demonstrated to have a range of biological effects on tissues [36], including promoting bone-fracture repairing, accelerating soft-tissue healing, inhibiting inflammatory responses, brain stimulation, increasing chemotherapy uptake, and so on. A recent report indicated that cancerous and healthy cell types were disturbed and response differently to the LIPUS at 0.5 MHz and a 20 ms pulse duration [37]. LIPUS may prove a safe, noninvasive, and cell-selective clinical use for disease tissue ablation. The cells were suggested to respond differently to ultrasound at different frequencies and with different fatigue behaviors based on their distinct mechanical properties.

3 Materials and methods

This study is intended to measure the mechanical properties of adherent cells by using AFM. The utilization of AFM should assist us in designing new therapies for human diseases. The investigation method (with AFM techniques) is the same for both oral cells and fibroblasts. However, these cells are examined to achieve different goals. The mechanical properties of oral cells (healthy, dysplastic, cancerous, and metastatic cells) are investigated with AFM for the evaluation of cellular response to the acoustic waves generated by the applicator (ultrasonic transducer). On the other hand, AFM is used to indicate the differentiation between normal fibroblasts and HGPS fibroblasts. The biomechanical properties of both fibroblasts and HGPS fibroblasts are further compared with immortalized fibroblasts' to estimate the impact of the transfection technique (hTERT transfection) on cells.

3.1 Cell lines and cell culture

Cell culture is an incredibly useful tool in biological research. Cell culture provides an imperative model system to study the basic physiology and biochemistry of cells (e.g., aging, metabolic studies), the effects of drugs and toxic compounds on the cells, and the process of mutagenesis and carcinogenesis. The major advantage of using cell culture is the consistency and reproducibility of results that can be obtained from using a batch of clonal cells. Cell culture allows easy control and manipulation of all physicochemical and physiological cell factors (i.e., temperature, osmotic pressure, pH, oxygen, and carbon dioxide tension, hormones, and nutrients).

3.1.1 Cells

Oral cells In order to carry out the project, six different head and neck squamous cell carcinoma cell lines, one epithelial dysplasia cell line, and one normal oral epithelial cell line were used. Carcinoma cell lines (UD-SCC-1, UD-SCC-2, UD-SCC-4, UD-SCC-6) were established in the laboratory at the Department of Oto-Rhino-Laryngology of University Hospital Düsseldorf using tissues from patients with head and neck squamous cell carcinoma (HNSCC). The procedure of cell lines establishing is described in detail by Ballo [38]. The UT-SCC-14 and UT-SCC-24B cell lines were established at the Department of Otorhinolaryngology-Head and Neck Surgery, Turku University Hospital [39] from primary tumors of two patients with squamous cell carcinoma. Dysplastic oral keratinocytes (DOK) and human oral keratinocyte (HOK) cell lines are commercially available cell lines.

The **UD-SCC-1** cell line is originating from oropharyngeal cancer. The primary tumor is classified by the TNM system as a tumor larger than 5 cm (T3), with infection of a lymph node at the internal thoracic artery (N2b) but without distant cancer spread (M0)- The T3N2bM0 tumor is from a 64-year-old male patient.

Cell line **UD-SCC-2** originates from hypopharyngeal cancer. The primary tumor is classified as smaller than 2 cm (T1) with infection of the lymph nodes (N2). Distant metastases were no found (M0). The T1N2M0 tumor is from a 58-year-old male patient.

Cell lines UD-SCC-4, UD-SCC-6, and UT-SCC-14 are all originating from tongue cancer. The primary tumor of the cell line **UD-SCC-4** is classified as larger than 5 cm (T3), infecting of an axillary lymph node (N1) but without distant metastases (M0). The T3N1M0 tumor is from a 47-year-old male patient. The primary tumor of the cell line **UD-SCC-6** is between 3 cm and 5 cm big (T2), without lymph node infection (N0) or distant metastases (M0). The T2N0M0 tumor is from a 64-year-old male patient. The primary tumor of cell line **UT-SCC-14** is between 5 cm and 7 cm big (T3) with infection of an axillary lymph node (N1) but without distant metastases (M0). The T3N1M0 tumor is from a 25-year-old male patient.

Cell line **UT-SCC-24B** originates from tongue cancer. The UT-SCC-24B cell line is highly metastatic cell line (metastatic site: neck) derived from primary cell line UT-SCC-24A. The metastatic tumor of cell line UT-SCC-24B is classified as larger than 2cm but smaller than 5 cm big (T2), with regional lymph node (N0) but without distant metastases (M0). The T2N0M0 tumor is from a 41-year-old male patient.

Cell line **DOK** was isolated from a fragment of the dorsal tongue from a 57-year-old male patient [40]. The degree of the dysplasia was mild to moderate.

The **HOK** cells from ScienCell Research Laboratories are isolated from human oral mucosa [41]. The cells are cryopreserved at passage one, they were additionally immortalized in the laboratory at the department of OtoRhino-Laryngology of University Hospital Düsseldorf to achieve a high proliferation rate.

The general characteristics and procurement information such as tumor cell line name, patient data, and TNM stage are summarized in Table 1. The TNM system is a globally recognized standard for classifying stages of cancer. The T refers to the size and extent of the primary tumor, the N to the number of nearby lymph nodes that have cancer, and the M to whether cancer has spread to a different part of the body.

Table 1: Synopsis of histopathological parameters of all patients with cancer with different disease conditions. Tumor samples are classified concerning location, type, staging, gender, and age of patients

Cell line	Sample Origin	Lesion Type	TNM Classification	Patient Gender	Patient age (year-old)
UD-SCC-1	Oropharynx (Tonsil)	Primary	T3N2bM0	M	64
UD-SCC-2	Hypopharynx	Primary	T1N2M0	M	58
UD-SCC-4	Oropharynx (Tongue)	Primary	T3N1M0	M	47
US-SCC-6	Oral cavity (Tongue)	Primary	T2N0M0	M	64
UT-SCC-14	Oral cavity (Tongue)	Primary	T3N1M0	M	25
UT-SCC-24B	Oral cavity (Tongue)	Primary (Metastatic)	T2N1M0	M	41
DOK	Dorsal (Tongue)	Primary	Dysplastic	M	57
HOK	Oral mucosa (Tongue)	Immortalized	Healthy	-	-

Dermal fibroblasts Primary dermal fibroblast cell lines were provided by Prof.-Dr. med. Michael Walter. Cell lines HGP003, HGP164, HGP178 were established in the laboratory at the Institute of Medicine of Charité University hospital Berlin from dermal samples of three HGPS patients. Cell lines 811, N14, and N20 were established in the laboratory at the Institute of Medicine of Charité University hospital Berlin from skin biopsies of three donors.

Cell line **HGP003** is derived from a skin biopsy from a male patient with a Hutchinson-Gilford progeria syndrome (HGPS) at the age of 2 years. Cell line **HGP164** is derived from a skin sample from a 4 -year-and-8-month-old girl with HGPS. Cell line **HGP178** is derived from a skin sample from a 6-year-and-11-month-old girl with HGPS.

Cell line **811** is derived from a skin sample from a 1-month-old female infant, who is diagnosed with sepsis. The **N14** and **N20** cell lines are derived from the skin biopsies of two 50-year-old female patients with a history of Cholelithiasis. Such diseases, sepsis, and cholelithiasis are not genetic disorders.

The fibroblat cell lines (HGP003, HGP164, HGP178, 811, N14, and N20) were additionally infected with the catalytic subunit human telomerase (hTERT), which successively elongates the shortened telomere, in the laboratory of the Institute for Laboratory Medicine, Clinical Chemistry and Pathobiochemistry of Charité - Universitätsmedizin Berlin to generate immortalized cell lines. These immortalized cell lines were named **HGP003-T**, **HGP164-T**, **HGP178-T**, **811-T**, **N14-T**, and **N20-T**, respectively.

The clinical characterizations and information such as human dermal cell line name, patient data are summarized in Table 2.

3.1.2 Cell culture

The vitro study was performed by the author within the frame of rules specified by the laboratory at the Department of Oto-Rhino-Laryngology of University Hospital Düsseldorf for the experiments.

Revival of the adherent cell lines oral cells and fibroblasts were thawed rapidly by gently agitating a vial of cells in a 37°C water bath. The vial contents were transferred to a centrifuge tube containing 9 ml of complete medium and centrifuged at 1400 rpm for 5 to 7 minutes. The cell pellet was gently resuspended in 5 ml of fresh culture medium and added to a growth vessel (10 cm Petri dish) with an appropriate volume of culture media (circa 10 ml).

Cultivation of head and neck squamous cell carcinoma cell lines Head and neck squamous cell carcinoma cell lines (UD-SCC-1, UD-SCC-2, UD-SCC-4,

Table 2: Synopsis of three patients with HGPS and three donors with other diseases that are not caused by a genetic defect. Tissue samples are categorized by origin, type, gender, and age of patients

Cell line	Sample Origin	Lesion Type	Classification	Patient Gender	Patient age (year-old)
HGP003	Skin	Primary	Progeria	M	2
HGP003-T	Skin	Immortalized	Progeria (+hTERT)	M	2
HGP164 (FN164)	Skin	Primary	Progeria	F	4y 8m
HGP164-T (FN164-T)	Skin	Immortalized	Progeria (+hTERT)	F	4y 8m
HGP178	Skin	Primary	Progeria	F	6y 11m
HGP178-T	Skin	Immortalized	Progeria (+hTERT)	F	6y 11m
811	Skin	Primary	Neonatal sepsis	F	1m
811-T	Skin	Immortalized	Neonatal sepsis (+hTERT)	F	1m
N14	Skin	Primary	Cholelithiasis	F	50
N14-T	Skin	Immortalized	Cholelithiasis (+hTERT)	F	50
N20	Skin	Primary	Cholelithiasis	F	50
N20-T	Skin	Immortalized	Cholelithiasis (+hTERT)	F	50

UD-SCC-6, UT-SCC14, and UT-SCC-24B) were cultured in Dulbeccos Modified Eagle Medium (DMEM, Gibco No. 31966) supplemented with 10 % fetal bovine serum, 1 % penicillin-streptomycin (10,000 U/ml), and 0.2 % MycoZap and maintained a incubator (37°C, 5 % CO_2(v/v). Cell lines were subcultured twice a week at a ratio of 1:3 depending on the confluency. The spent medium was aspirated and the dish washed with 5 ml to 10 ml phosphate-buffered saline (PBS) to get rid of any FBS in the residual medium. Afterward, the 2 ml Trypsin-EDTA(1x) (detaching agent) was added to the washed dish, and returned the dish to the 37°C incubator. Using an inverted microscope to check for cell layer dispersion, before 7 ml of complete growth medium was added to stop the trypsin reaction. The cell solution was pipetted up and down several times to separate the cell clumps into single cells, and one-third volume of cell resuspension (the detached cells in medium) was transferred to a dish containing fresh medium.

Cultivation of dysplastic oral keratinocyte cell line The DOK cell line was cultivated in DMEM medium containing 10 % fetal bovine serum, 1 % penicillin-streptomycin (10,000 U/ml), and 0.5 % hydrocortisone (1 μg/ml). DOK cells were routinely subcultured every three to four days. During cell subculture, the conditioned culture media was removed and the rinsed dish with 5 ml to 10 ml PBS. Afterward, the 2 ml Trypsin-EDTA solution was added to the washed dish and returned the dish to the 37°C incubator. The digestion was stopped by adding 7 ml of fresh cell culture medium, and cell solution was pipetted, and then one-third volume of the cell resuspension was kept culturing by adding another certain amount of fresh medium.

Cultivation of human oral keratinocyte cell line The HOK cell line was cultivated in oral keratinocyte medium (OKM) supplemented with 1 % oral keratinocyte growth supplement (OKGS, Cat. 2652) and 1 % penicillin-streptomycin (P/S, Cat. 0503). Cell lines were subcultured once a week at a ratio of 1:2 and 1:3 depending on the confluency. The spent medium was discarded and the dish washed with 5 ml to 10 ml PBS. Afterward, the 2 ml Trypsin-EDTA(1x) (detaching agent) was added to the washed dish, and returned the dish to the 37°C incubator. Dishes were inspected under an inverted microscope to check for cell layer dispersion before 7 ml of complete growth medium was added to stop the trypsin reaction. The cell solution was transferred to a centrifuge tube and centrifuged (5 mins, 350 g, 20°C). After centrifugation, the supernatant was aspirated, and the cell pellet was resuspended in 3 ml (or 4 ml) of a complete medium. The cell solution was pipetted up and down several times to separate the cell clumps into single cells, and then the one-third (or one-fourth) volume of the cell resuspension was transferred to a 0.1 % gelatin-coated dish containing a fresh medium with the required number of cells.

To Prepare a gelatin-coated dish, 2 ml of 0.1 % gelatin was added to a petri dish and placed in the 37°C incubator for 30 minutes. After 30 minutes of waiting, the gelatin solution was aspirated before cell seeding.

Cultivation of dermal fibroblast cell lines The dermal fibroblast cell lines (HGP003, HGP003-T, HGP164, HGP164, HGP164-T, HGP178, HGP178-T, 811, 811-T, N14, N14-T, N20, and N20-T) were cultivated in DMEM medium with 10 % fetal bovine serum and 1 % penicillin-streptomycin (10,000 U/ml). Cell lines were subcultured once every two weeks (or once a month) at a ratio of 1:2 depending on the confluency. The spent medium was aspirated and the dish washed with 5 ml to 10 ml PBS. Afterward, the 2 ml Trypsin-EDTA solution was added to the washed dish, and returned the dish back to the 37°C incubator. Using an inverted microscope for detachment, before 7 ml of complete growth medium was added to stop the trypsin reaction. The cell suspension was transferred to a centrifuge tube and centrifuged at 1400 rpm for 5 minutes. After spinning, the supernatant was aspirated, and the remaining cell pellet was resuspended in 2 ml (or 3 ml) of fresh culture medium, and then half (or one-third) volume of the cell resuspension was kept culturing by adding another certain amount of fresh medium.

3.1.3 Sample preparation for measurements

Sample preparation for AFM measurements During sample preparation of head and neck squamous cell carcinoma cell lines, all of the oral cells (healthy, dysplastic, cancerous, and metastatic cells) were cultivated in Petri dishes (TPP, No. 93040) coated with 0.1 % gelatin as a controlled variable (Figure 11), because of the cultivation process of HOK cell line. A cell strainer 40 μm was additionally utilized in order to remove cell clumps and debris, especially for the UD-SCC-4, UD-SCC-6, UT-SCC-14, and UTSCC-24B cell lines.

During samples of dermal fibroblast cell lines, no gelatin-coated dish was required, and fibroblasts were seeded onto a culture dish (TPP, No. 93040).

Samples were prepared 72 hours prior to an AFM measurement, so that cell monolayer at confluency level above 70 % is observed under an inverted microscope. The number of cells used for sample preparation can be found in Appendix A.1. After three days of incubation, the spent medium was changed into a fresh medium to move any floating debris or dead cells.

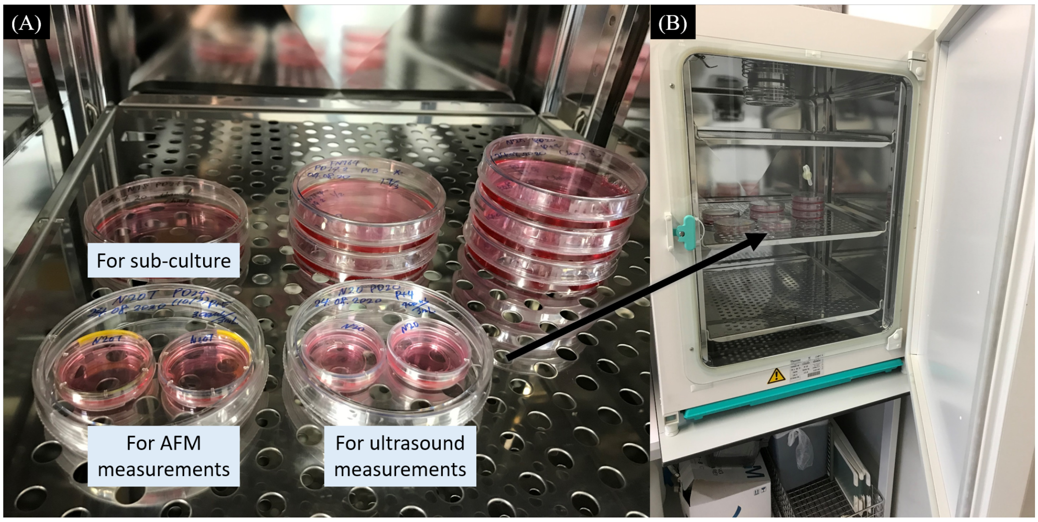

Figure 11: (A) Cell subculture and sample preparation (B) Cell culture environment

Sample preparation for ultrasound measurements During samples of head and neck squamous cell carcinoma cell lines, all of the oral cells (healthy, dysplastic, cancerous, and metastatic cells) were cultivated in imaging dishes (Mobitex, No. 6160) coated with 0.1 % gelatin (Figure 11). A cell strainer of 40 μm was additionally utilized in order to remove cell clumps and debris, especially for the UD-SCC-4, UD-SCC-6, UT-SCC-14, and UTSCC-24B cell lines. The 35 mm cell imaging dishes with a glass bottom were used for high resolution (live cell) imaging.

3.2 Atomic force microscopy experiments

Atomic force microscopy (AFM) is a kind of scanning probe microscopy, and its near-field technique is based on the interaction between a sharp tip and the atoms of the sample surface. To address the wide complexity of biological systems, which can range from nucleic acids and proteins to cells and tissues, a variety of AFM modes have been implemented over the years. The biological AFM emerged as a powerful, multifunctional imaging platform that allows biological samples, including biomolecules and cells, to be visualized and manipulated whether in a controlled atmosphere or a liquid medium. There are several methods and many ways to modify the tip of the AFM to investigate sample surface properties, including measuring the changes in mechanical property of cell membrane, cell stiffness, and cell viscoelasticity.

3.2.1 AFM setup

The AFM (NanoWizard 3, Bruker) is located at the Institute of Physical Biology of Heinrich-Heine-University Düsseldorf. The AFM is coupled with the inverted microscope (Olympus IX73) connecting with two cameras (upper: DBK31BF03; lower: DFK31BF03). A hybrid AFM-inverted microscope placed on the vibration isolation system (i4 Series, Accurion GmbH) is equipped in a vibration isolation cabinet (Figure 12).

The core of the NanoWizard 3 BioScience system is HyperDrive (Figure12) allowing to detect the smallest cantilever deflections. The Nanowizard 3 is equipped with $100 \times 100 \times 15\,\mu\text{m}^3$ x-y-z piezos and an extra Z piezo of $100\,\mu$mm, which uses capacitive sensors for position measurement. The quantitative imaging (QI) tip movement algorithm is developed by JPK to prevent lateral forces and controls vertical forces, making nondestructive measurements for cantilever tip and sample.

3.2.2 Data acquisition

The elastic moduli measurements were performed on living cells using a silicon nitride cantilever of spring constant 0.1 N/m (CP-qp-CONT-SiO, NanoandMore). A single sphere was attached to the end of the tip with a diameter of $6.62\,\mu$m

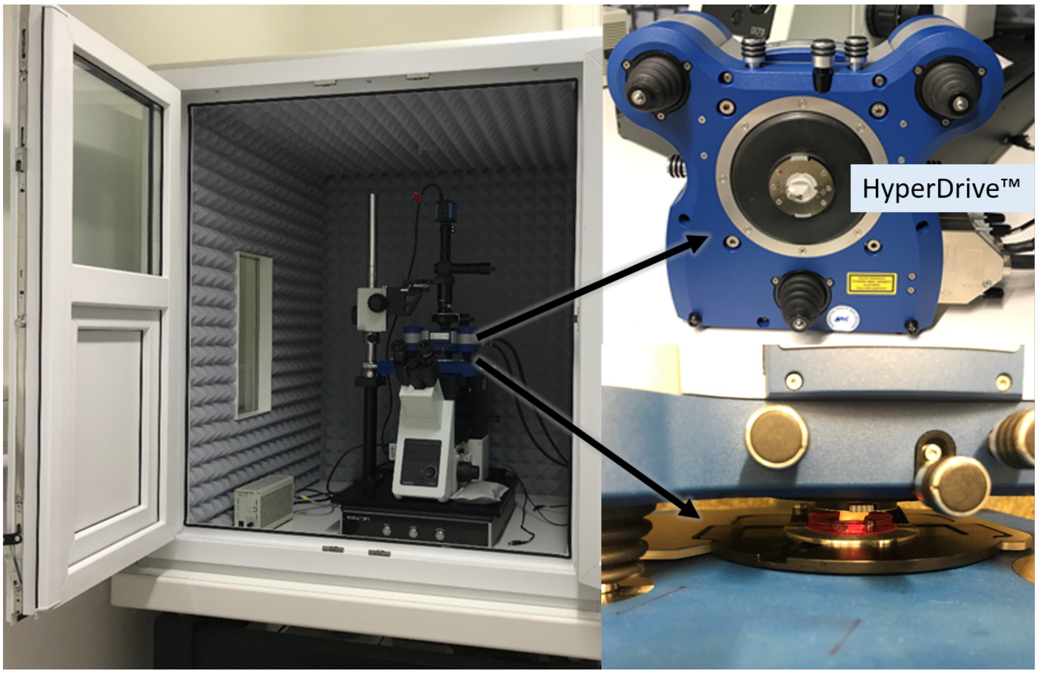

Figure 12: AFM equipment mounted onto an inverted microscope (Olympus IX73)

(Figure 13 (A)). The cell imaging measurements were conducted using a soft sharp probe (a pyramidal shape with a nominal tip radius of 15nm and a tip angle of 25° - 45° with a nominal force constant of 0.08 N/m (silicon nitride triangular shaped with reflect coating OMCL-TR400PSA from Olympus) (Figure 13 (B)).

A sample (Petri dish) was attached to a round metal holder (Figure 12) and mounted on the stage of the AFM at room temperature. The complete growth medium was added to the maximum capacity volume of the petri dish to eliminate capillary forces and reduce the vibration in a liquid environment. Samples (petri dishes) were replaced by a new one within one hour due to cell viability.

The bending of the cantilever (deflection) is detected by optical means. The IR laser beam (laser spot) was first focused on the tip of the cantilever using an optical microscope with CCD-camera (Figure 14) and laser adjustments screws (Figure 12), and the laser spot reflected from the cantilever and was detected by the detection system (the reflected beam was presented in the laser alignment window). Afterward, the reflected beam was moved to the center of the photodiode detector with detector adjustment screws. The reflection signal from the different

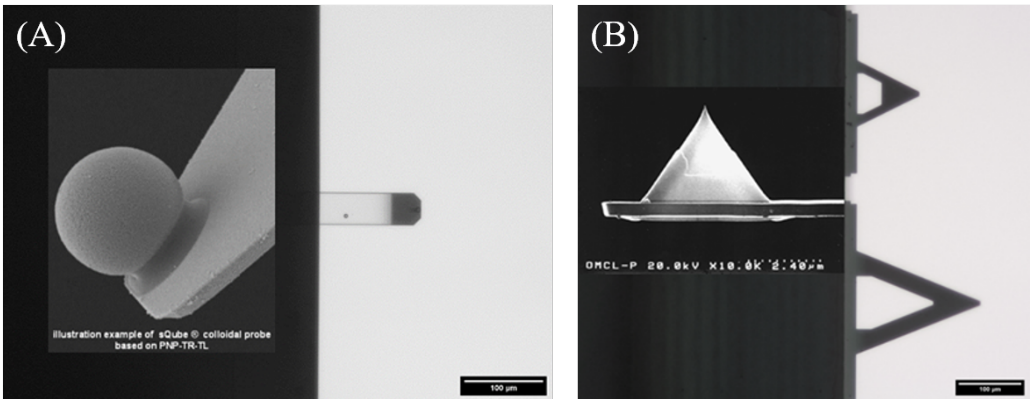

Figure 13: The AFM tip side view of the CP-qp-CONT-SiO (A), and the OMCL-TR400PSA (B)

quadrants of the detector graphically presented in the laser alignment window in SPM software.

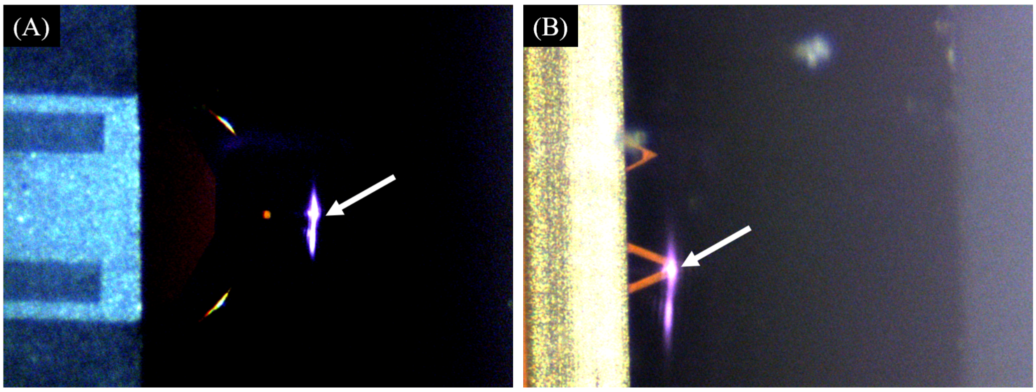

Figure 14: The laser spot pointed out with the white arrows need to be focused on the tip of the CP-qp-CONT-SiO (A) and the OMCL-TR400PSA (B)

When the laser beam has been focused on the tip of the cantilever and the reflected beam has also been adjusted, however, the sum presented in the laser alignment window (the maximum laser value for the cantilever) is still close to zero. In this case, the mirror must be readjusted. The difference in angle of the optical path has to be corrected with the adjustment mirror, especially for samples in a liquid environment.

Each cantilever was calibrated before each AFM measurement in order to obtain precise force data. The deflection sensitivity was calibrated by ramping the cantilever against a hard surface, a plastic Petri dish substrate (TPP, No. 93040) in the presence of complete growth existed as a stiff subject (Figure 15(A)). The spring constant of the cantilever was determined from the thermal noise spectrum (Figure 15(B)).

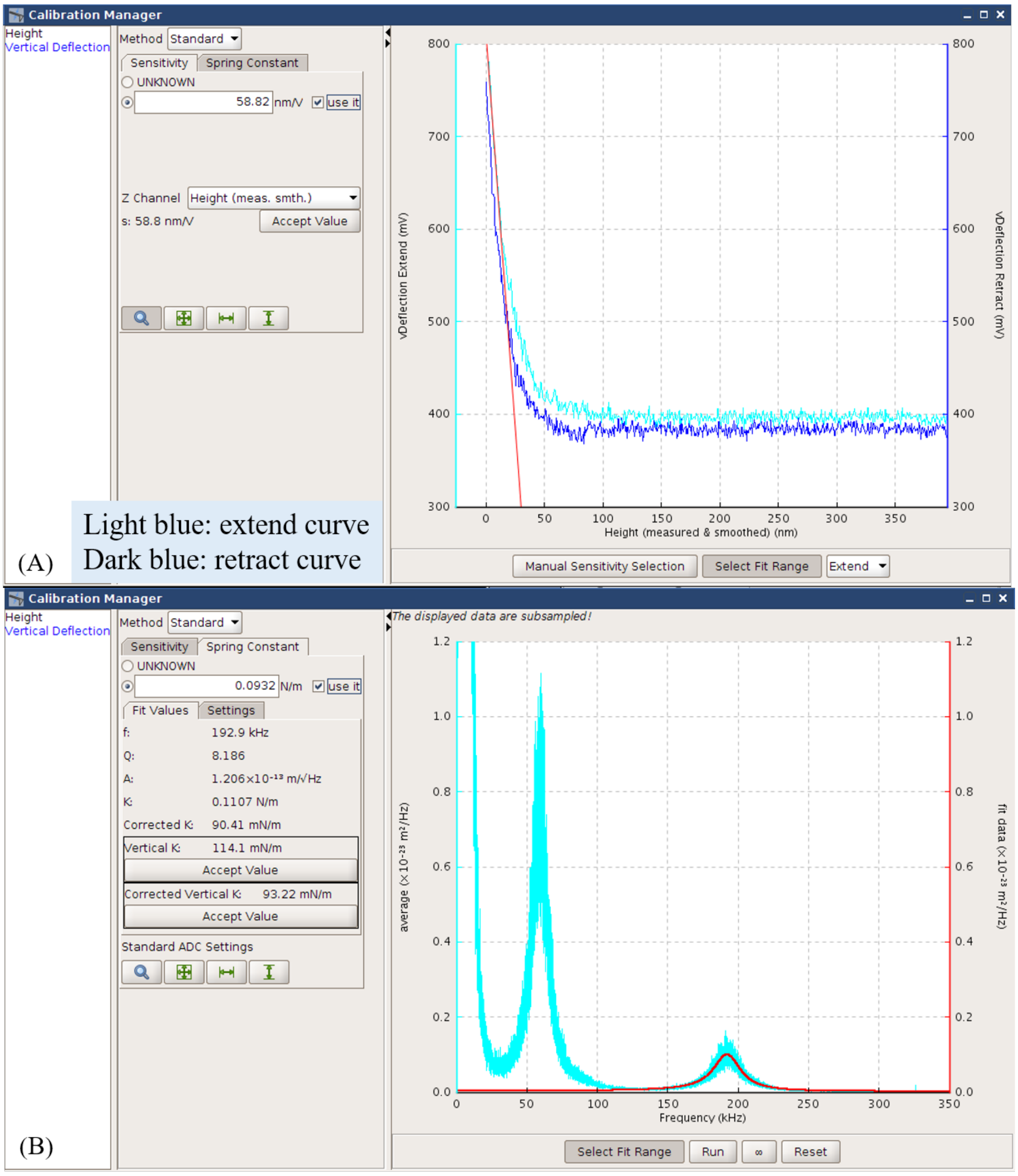
(A)

Light blue: extend curve
Dark blue: retract curve

Calibration Manager
Height
Vertical Deflection
Method Standard
Sensitivity | Spring Constant
○ UNKNOWN
● 58.82 nm/V ☑ use it
Z Channel Height (meas. smth.)
s: 58.8 nm/V

(B)

Calibration Manager
Height
Vertical Deflection
Method Standard
Sensitivity | Spring Constant
○ UNKNOWN
● 0.0932 N/m ☑ use it
Fit Values | Settings
f: 192.9 kHz
Q: 8.186
A: 1.206×10^{-13} m/√Hz
K: 0.1107 N/m
Corrected K: 90.41 mN/m
Vertical K: 114.1 mN/m
Corrected Vertical K: 93.22 mN/m
Standard ADC Settings
The displayed data are subsampled!

Figure 15: Calibration of cantilever

After the calibration of the cantilever, the cantilever was placed over the sample using the optical system integrated with AFM (Figure 16).

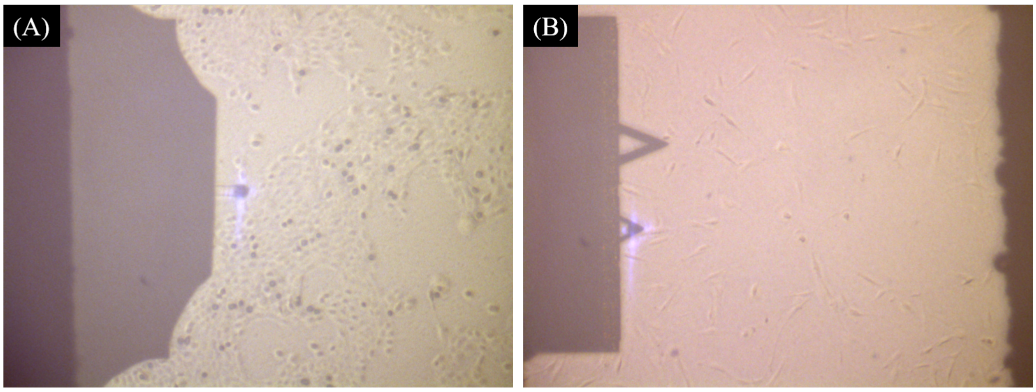

Figure 16: The Cantilever is placed over (A) the UD-SCC-1 Cells and (B) the HGP003 cells

To obtain force-indentation curves, the sample (the cell) was indented in contact mode (QI advanced). Each cell was indented only once. The AFM tip semi-automatically moved on a selected area matrix. In QI mode, a complete force-distance curve was recorded at each pixel of the scan area and the resolution was set to 32×32 pixels for cell mechanics studies with a trigger force of 3 nN. To obtain the high-resolution cell imaging (256×256 pixels), an appropriate trigger force, such as 4 nN was selected to carry out AFM measurements. During AFM measurements, the force curves were online calculated and generated into different channels (height (measured) image, slope, and adhesion) in the Data viewer windows, as illustrated in Figure 17.

The available channels can be obtained simultaneously during AFM imaging. Each channel can be displayed as either trace or retrace. The data from a force experiment is performed in contact mode and is displayed as an x-y plot (x-axes: the height position of the cantilever for approach and retract (nm); y-axes: the deflection of the cantilever (nN)). These force-distance curves (plots) produced during force spectroscopy mode were recorded at a scan rate of 100 kHz in QI mode with the image and are accessible for offline analysis. For more details about force curves analysis see section 2.2.3.

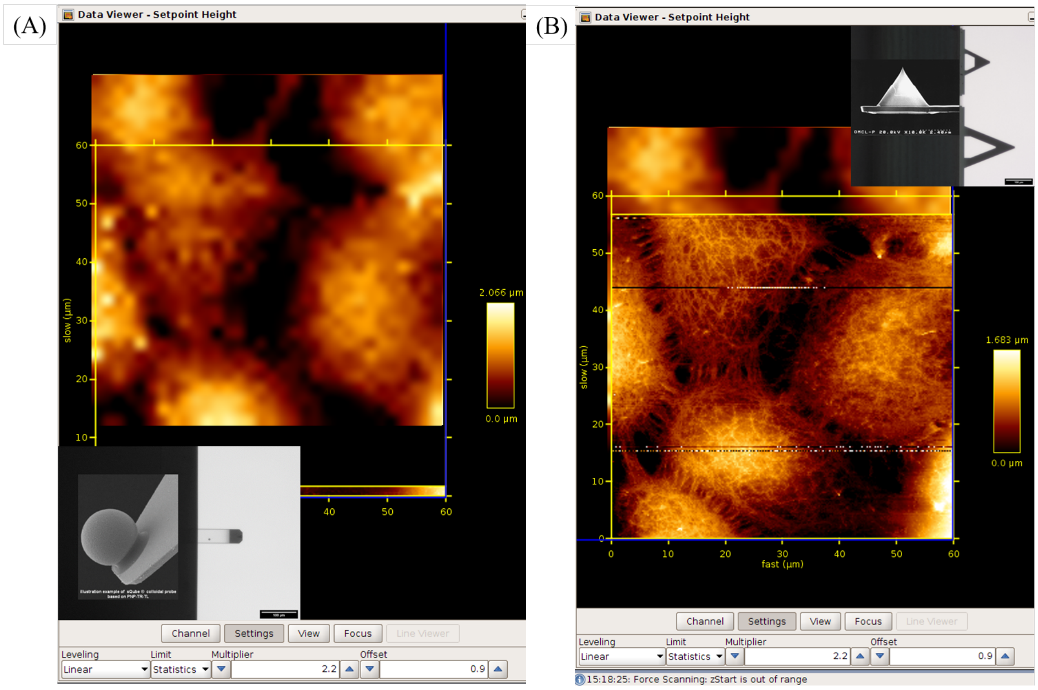

(A) Leveling: Linear; Limit: Statistics; Multiplier: 2.2; Offset: 0.9

(B) Leveling: Linear; Limit: Statistics; Multiplier: 2.2; Offset: 0.9

15:18:25: Force Scanning: zStart is out of range

Figure 17: AFM measurement using JPK SPM software (A) with a spherical tip (B) with a pyramidal tip

3.2.3 Data analysis

The offline analysis processing was accessed with the JPK SPM data processing program (DP program, Bruker). The force curve during the extension of z-piezo was used to determine Young's Modulus of cells. The mechanical properties of cells were represented in terms of Young's modulus of elasticity (E).

For data post-processing, several fitting parameters have been chosen. First of all, the baseline offset in vertical deflection was removed before further processing. When the cantilever is far away from the sample surface, the interaction force is virtually zero. The offset, by the reason of the initial setting of the equipment or the thermal drift, should be subtracted from all the deflection data to calculate the true interaction force. Subsequently, the point where the force curve crosses the zero-force line was automatically calculated and set as the zero of the x-axis. Then the vertical deflection was further calibrated with the saved sensitivity and saved spring constant of the cantilever using calibration operation. However, before the calculation of Young's Modulus, the height signal for cantilever deflection should be corrected with tip-sample separation. The corrected distance is always shorter than the raw height signal (slope or force curve is steeper) because the cantilever deflection occurred in the opposite direction leading to an additional piezo movement towards the sample. At last, the Young's Modulus of a sample was automatically calculated by applying a Hertz/ Sneddon fitting (chapter 1.2.1) to the whole extend force curves (Figure 18). After data post-processing, a new image displaying the results of Young's Modulus was obtained which reveals the differences in cell elasticity.

The nanoindentation data was processed by curve-fitting with the Hertz contact model under the specific assumption in a defined regime using JPK data processing software. Depending on the shapes of the indenter, the radius, half-angle (pyramid) have to be specified. The Poisson ratio is usually set to be 0.5. A flowchart (Figure 19) with symbols depicts the data process.

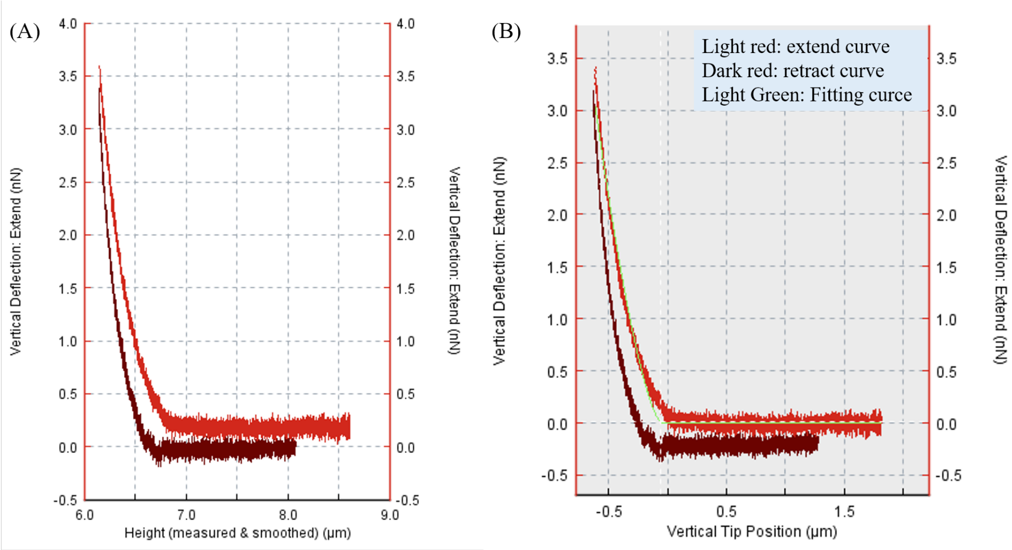

Figure 18: Data processing: (A) row data, (B) the force curve fitted to the Hertz model

With both force-indentation curves and Young's modulus image, the regions of interest in a cell were defined. Even without nucleus extraction, mechanical properties of the nuclear and peripheral region of cells still can be investigated, attributable to the cell image with a distinct nucleus is observed. The peripheral region of the cell has defined the region of cytoplasm without the central nucleus.

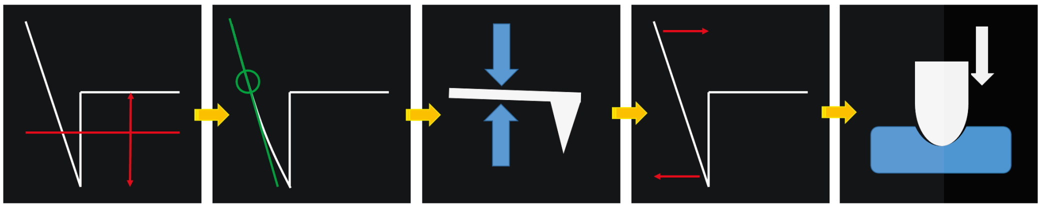

Figure 19: A simplified flowchart depicts AFM data analysis: first, automatically subtract the baseline; secondly, automatically adjust the x offset (contact point); thirdly, (re-) calibrate vertical deflection by adjusting sensitivity and spring constant; afterward, the correct height for cantilever bending (vertical tip position); and in the end, determinate elasticity from indentation (Young's Modulus)

3.2.4 Statistical analysis

The statistical difference of the overall difference between groups was analyzed by analysis of one-way variance (ANOVA) using R commander. Once ANOVA indicated statistical significance, Tukey's test was automatically performed to compare means of all treatments to the means of every other treatment.

3.3 Ultrasound experiments

The biomechanical properties of human cells were probed by AFM as discussed in the previous chapters. Each cell exhibited distinguishable cell structure and cellular stiffness from another cell. The differences in biomechanics can lead to cells respond differently to the acoustic waves that induce oscillation in cells. A large amplitude, which can be obtained at one peculiar frequency, may destroy carcinoma cells instead of healthy cells. In this study, oral cells (healthy and cancer cells) were irradiated with different resonance frequencies, 24.71 kHz and 67.57 kHz respectively. Cells' reactions in response to external mechanical waves were perceived and recorded with an inverted microscope connecting to a camera.

3.3.1 Ultrasound setup

The ultrasound (US) measurements were carried out in the laboratory at the Institute of Organic and Macromolecular Chemistry of Heinrich-Heine-University Düsseldorf. The whole ultrasound setup was equipped in a vibration isolation cabinet (Figure 20).

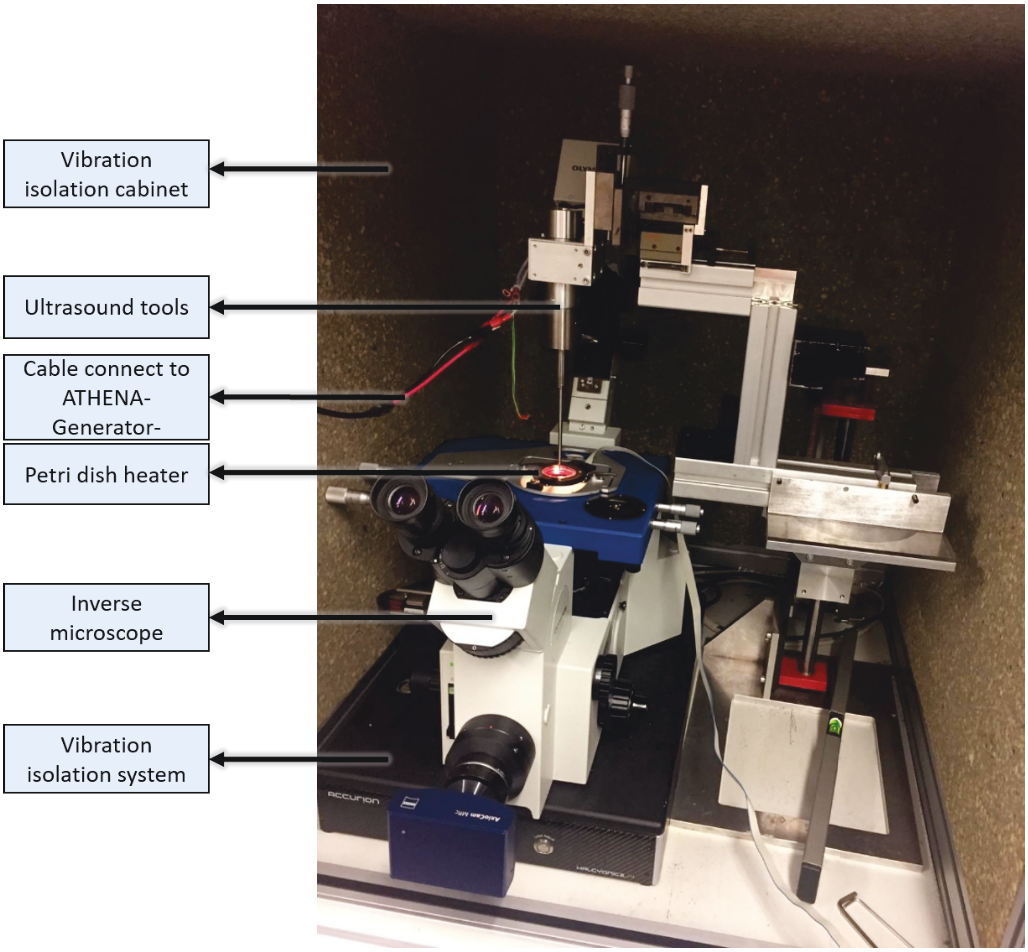

Figure 20: The ultrasound setup: acoustic actuator with an inverted microscope (Olympus IX70)

The ultrasound setup used to observe the reaction of cells to acoustic waves consists of several components: generator, converter, booster, and sonotrode. An ultrasound generator uses to generate the required voltage in respectively required ultrasonic frequency. The ATHENA ultrasonic generator from ATHENA Technologie Beratung GmbH which provides an operating frequency range from 20 to 300 kHz was applied. The converter, made up of piezoelectric aluminum discs, played as the interface between the electric and the mechanical area that converts the high-frequency voltage to mechanical longitudinal vibrations. The booster increased or reduced the vibration (amplitude) from the converter and transferred it into the sonotrode. The sonotrode (or horn) being the tool transmits the mechanical vibrations into the component that needs to be processed. A brief illustration of the ultrasound device is shown in Figure 21.

The titanium sonotrode, with the approximation of the 65 μm diameter, was manufactured in the central workshop of Physics at the Heinrich-Heine-University Düsseldorf. During US measurements, the Petri dish heater (JPK, Bruker) was applied for long-term cell studies, as the heater enabled temperature control of cell culture dishes. For living cell experiments the temperature was set to 37°C. However, without optimal conditions such as the CO_2(v/v), the oxygen content of the atmosphere, and humidity levels, the sample (the dish) was replaced into a new one within two hours during the ultrasound measurements.

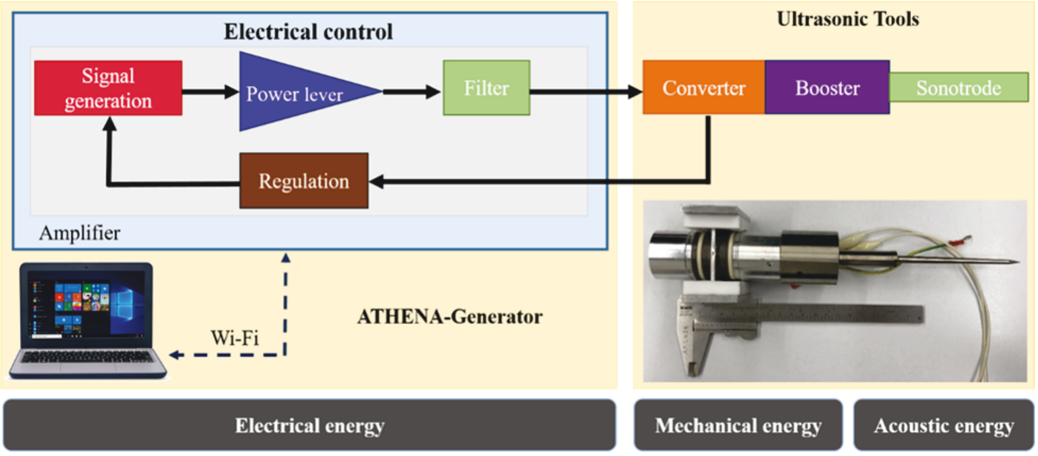

Figure 21: A brief illustration of ultrasound device

3.3.2 Acoustic waves

The problem with the control of the ultrasound probe is that it cannot vibrate stably at any frequency, but rather the peaks at which the frequency runs stably in the case of resonance must be found. Therefore, the ultrasound probe must be calibrated in advance. Figure 22 shows that the frequency response is measured with the corresponding potential resonance frequencies. Clear peaks can be seen in the frequency response at higher frequencies (>24.7 kHz). However, only the frequencies at which the phase crosses zero can be used. At 24.7 kHz, both the peak within the frequency response and the zero crossings in the phase can be seen, since the probe was originally designed for this frequency range. In the case of the ultrasound probe used here, only two frequencies, at 24.7 kHz and 67.5 kHz and a maximum amplitude of 400 mA, can be used.

Formula (5) explains the simultaneous change of the target current and the frequency used. The current is selected differently for the two frequencies to generate a comparable speed of vibration and to ensure the stability of the probe. The Formula (5) describes the calculation of the vibration speed of the set frequencies. The calibration factor results from the slope of the characteristic curve as shown in Figure 23, which has already been determined previously by a Laser Doppler vibrometer (LVD). The LVD measurement was accomplished in the department of Dynamics and Mechatronics at the University of Paderborn. From the values of the calibration factor in Table 3, a set current of 150 mA at 24.7 kHz and a set current of 400 mA at 67.5 kHz, for instance, results in a similar vibration speed of 1.0 m/s. The two adjustable parameters for the ultrasound experiment are the oscillation frequency and current amplitude. The resulting vibration speed can be calculated using the calibration factor that is previously determined. The measurement results of the calibration factor results from the slope of the characteristic curve at other resonances can be found in Appendix B.1.

$$v = K \cdot I_{soll} \tag{5}$$

where

v is the vibration speed of the sonotrode
K is the calibration factor
I_{soll} is the current

Table 3: Calibration factors in four different modes of the ultrasound probe

Mode (kHz)	K (m/sA)	Standard deviation (m/sA)
24.7	6.470	0.021
33.1	0.301	0.002
49.5	0.162	0.021
67.5	2.695	0.170

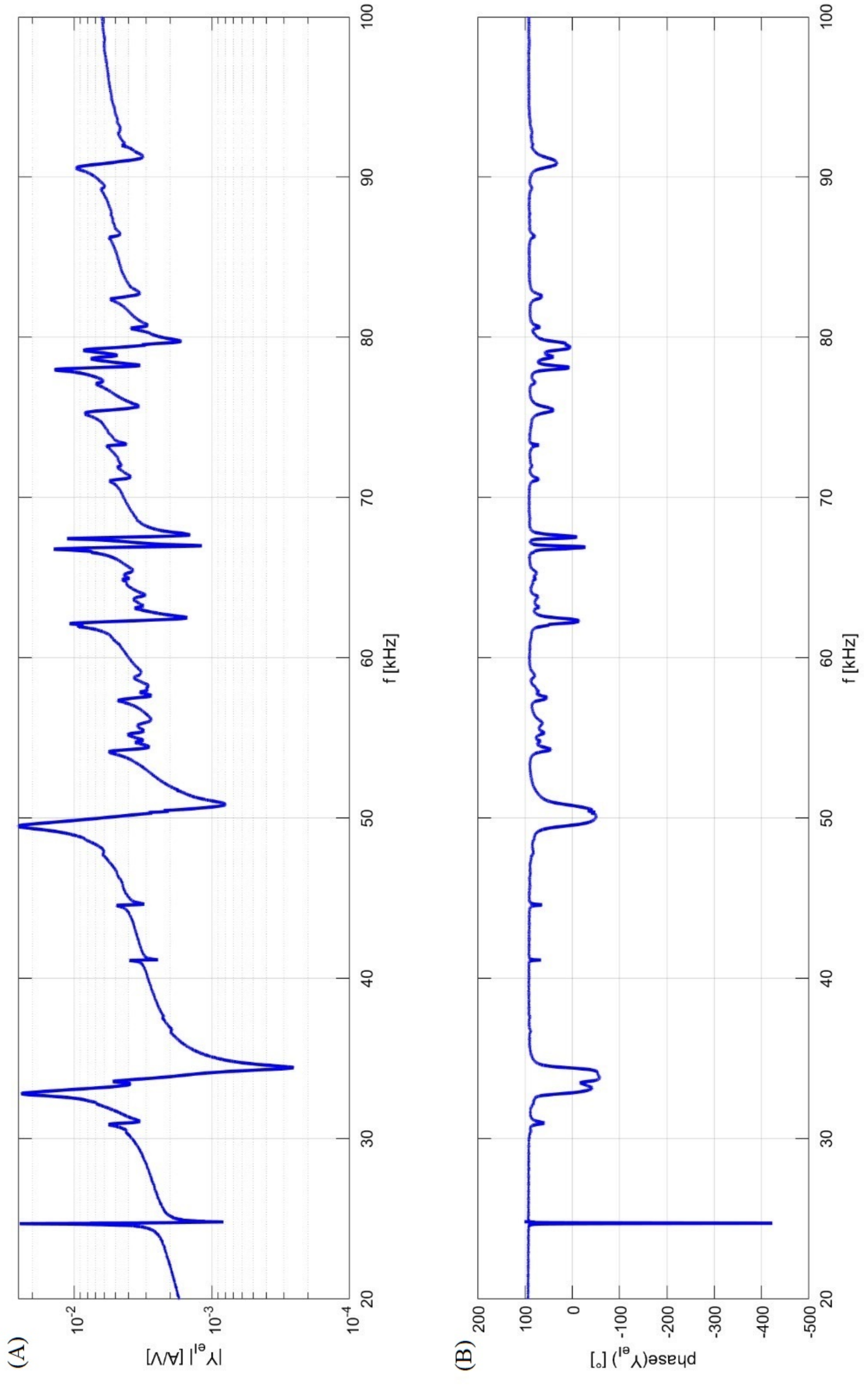

Figure 22: The characterization of the acoustic waves: (A) oscillator output gain and (B) phase shift

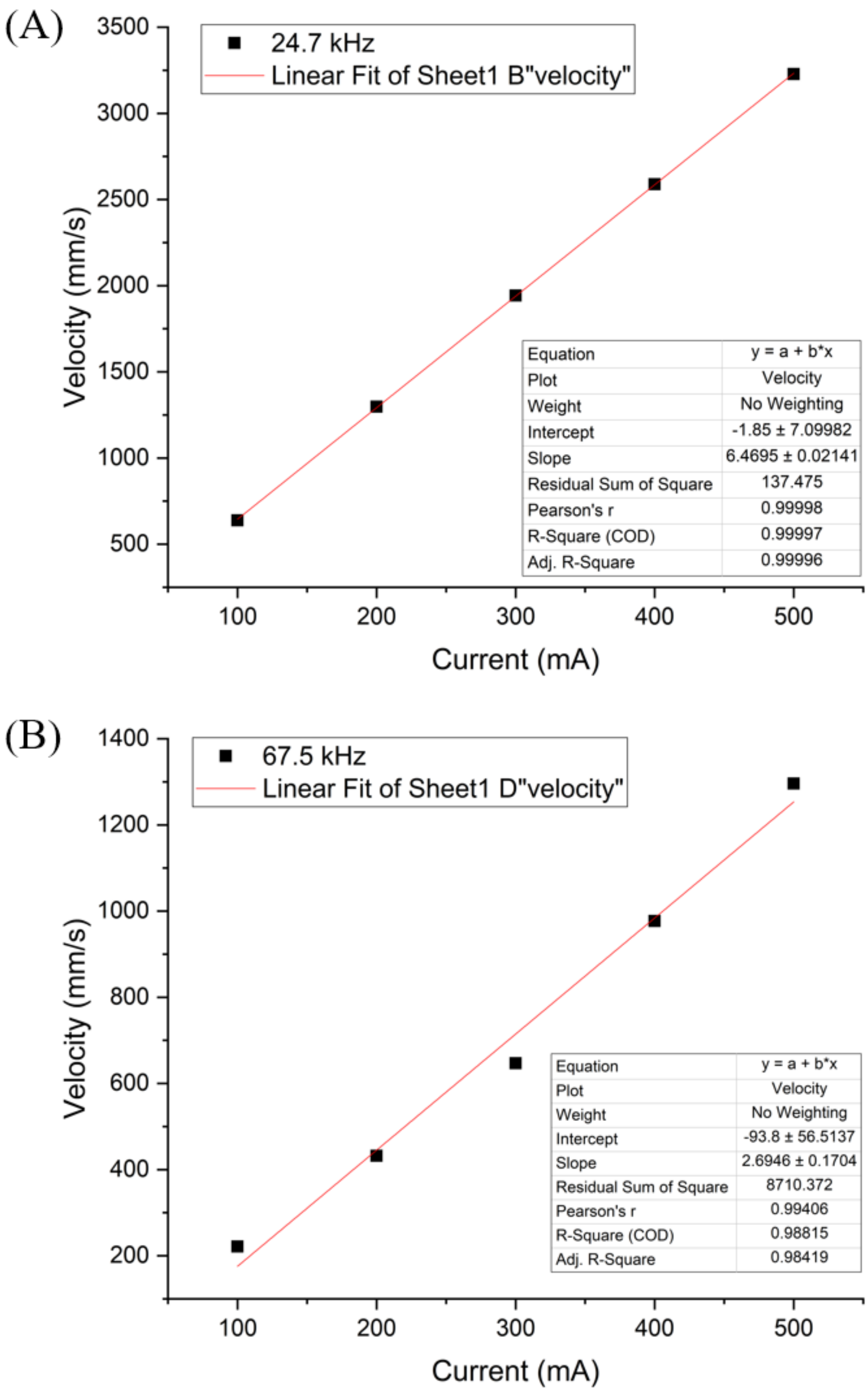

Figure 23: Vibration velocity- target current characteristics of the two resonances according to the measurements using laser Doppler vibrometer: (A) at the resonance frequency of 24.7 kHz (B) at the resonance frequency of 67.5 kHz

4 Results and discussion

Both cellular biomechanical properties and subcellular structures are revealed utilizing AFM. A detailed evaluation of the results is given in this chapter. The optimization of experimental control variables is first presented. After the optimization, the biomechanical properties of oral cells are then given to indicate whether cell conditions are altered in cancerous oral cells. Reflecting the response of oral cells to acoustic waves generated using the US instrument is covered in the following section.

Additionally, the direct comparison of mechanical properties between normal and HGPS skin fibroblasts is exhibited using AFM. The difference in cells' biomechanical features indicates whether nuclear defects have an impact on cellular behaviors. The transfection technique is further required to restore cell functions and extend the lifespan of cells. The AFM is once more implemented to determine whether the transfection with the hTERT gene affects the fibroblasts' cell functions. At the end of each section, an overview discussion is provided.

4.1 Optimal parameters and environment conditions for AFM measurements

The AFM assessment of the value of Young's modulus is not an easy task due to effects from various factors. They can be linked with the experimental conditions provided by the AFM, such as the scan rate, the indentation force, and the stiff substrate below the investigated cells. Other important factors influencing the mechanical properties of cells are those which directly influence the cellular properties, such as the day of measurement after the passage, culture condition (buffer composition), and the density of cell confluence on a substrate.

Therefore, a suitable selection of physical or physiological cues affecting the AFM-based assessment is necessary. The optimal parameters and conditions for living cell measurements are given as following. All the AFM measurements were conducted by the author, besides the measurements in chapter 4.1.1 was performed together with a student as a part of the bachelor thesis [1].

---

[1] Anna Frigge

4.1.1 Optimization of parameters

AFM operation is usually described as one of three modes: contact mode, tapping mode (intermittent contact), and non-contact mode. Different parameter settings of a mode, such as scan size, scan rate, and set point values (applied force) affect data output differently. In the contact mode that we chose in this study, the scan rate is decreased as the scan size is increased.

During the AFM experiments, we applied the same force (3.3 nN) on the same UD-SCC-1 cell at a scanning speed range of 2.5 to 50 μm/s. Here, we chose the speed order of 50, 40, 25, 15, 5, 2.5, 10, 20, 30 μm/s, instead of gradual cumulative or plummeting speed rate, to execute the AFM measurements to ensure the resistance of the sample under the compression. UD-SCC-1 cells were indented by colloidal probes to obtain force curve measurements to estimate the Young's modulus of cells.

As illustrated in Figure 24, the extend and retract force curves are not identical, the slope of the curves noticeably changed when the indentation velocity is greater than 10 μm/s. It seems like the gap between the baselines of the extend curve and of retract curve depends on the speed of scanning. AFM probing of the UD-SCC-1 cell at a constant approach- and retraction velocity of 15 μm/s, the retract curve shifted below the extend curve (Figure 24(F)).

We also examined the Young's modulus of the UD-SCC-1 nucleus obtained from approaching force curves, force-displacement data were analyzed by fitting them with Hertzian models of contact in which two major assumptions: linear elasticity and infinite sample thickness are made. There is no significant difference in those of the elastic values obtained from approaching force curves at scanning speed under 10 μm/s, whereas cellular mechanical response starts to change at the loading speed greater than 10 μm/s.

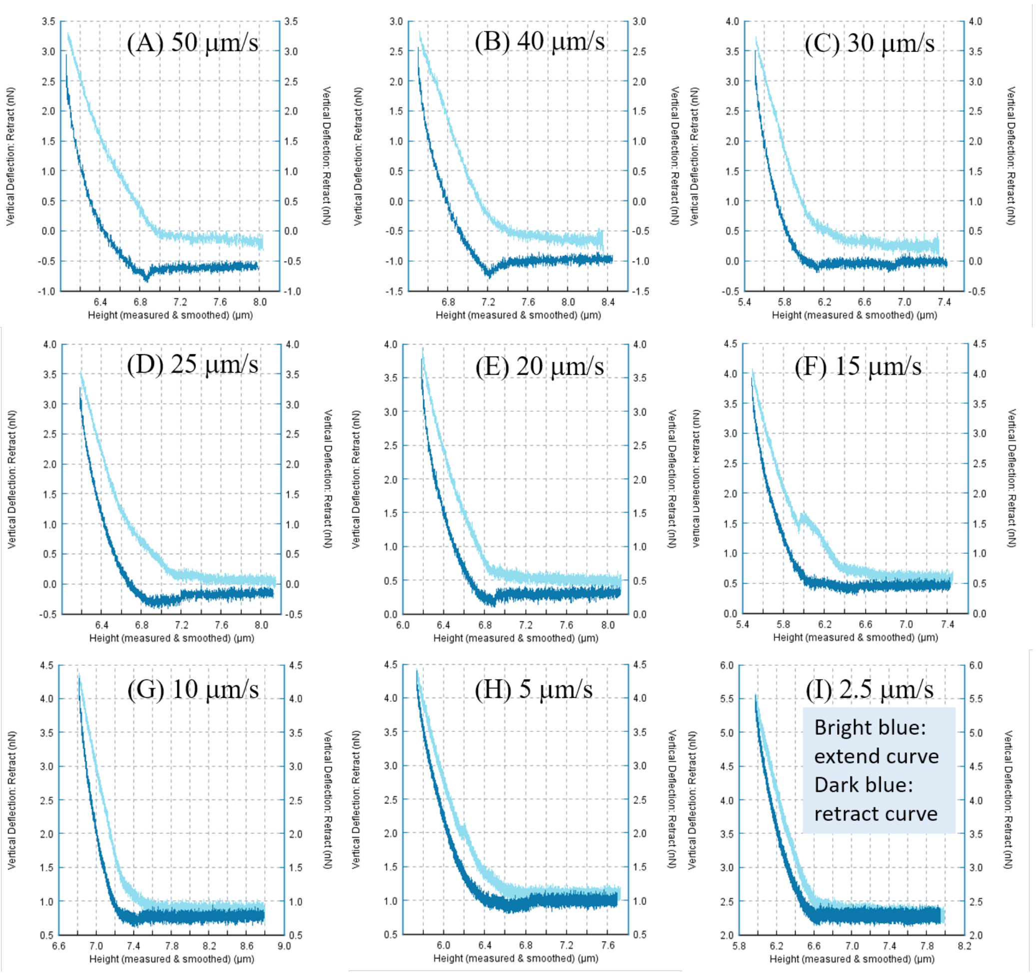

Figure 24: Force-indentation curves of the UD-SCC-1 nucleus applied with the same force (3.3 nN) at different scanning rate (from 2.5 to 50 μm/s). At scanning speed over 15 μm/s, the gap between the baselines of the extend curve and of the retract curve is increasing.

Cells' mechanical resistance to compression forces applied with AFM probe is complex and depends on both scan rate and force magnitude. Thus, we further probed another UD-SCC-1 cell with different applied forces ranging from 1 nN to 4 nN, but at a constant scan rate of 6 μm/s. Figure 25 shows that the force-indentation curve of the UD-SCC-1 nucleus was steady when the applied forces were less than 3.5 nN. Continuing increasing the applied force on the cell, the force-indentation curves became unstable at applied force over 3.5 nN. When the applied force was smaller than 1.5 nN, the force seemed not sufficient enough to deform the cell.

AFM is used to probe the elastic responses of single cells undergoing deformation. The Young's modulus that is based on Hertz's theory was used to calculate the stiffness of individual UD-SCC-1 cells. When the indentation force was below 2 nN, it led to a decrease in the elastic modulus because of insufficient indentation force. The insufficient indentation force at the constant scanning rate generates unreliable data for elastic modulus estimation, whereas the exceeding applied force may damage the cell generating higher estimated cell elasticity. Therefore, appropriate applied force should be examined for each cell line before the AFM assessment.

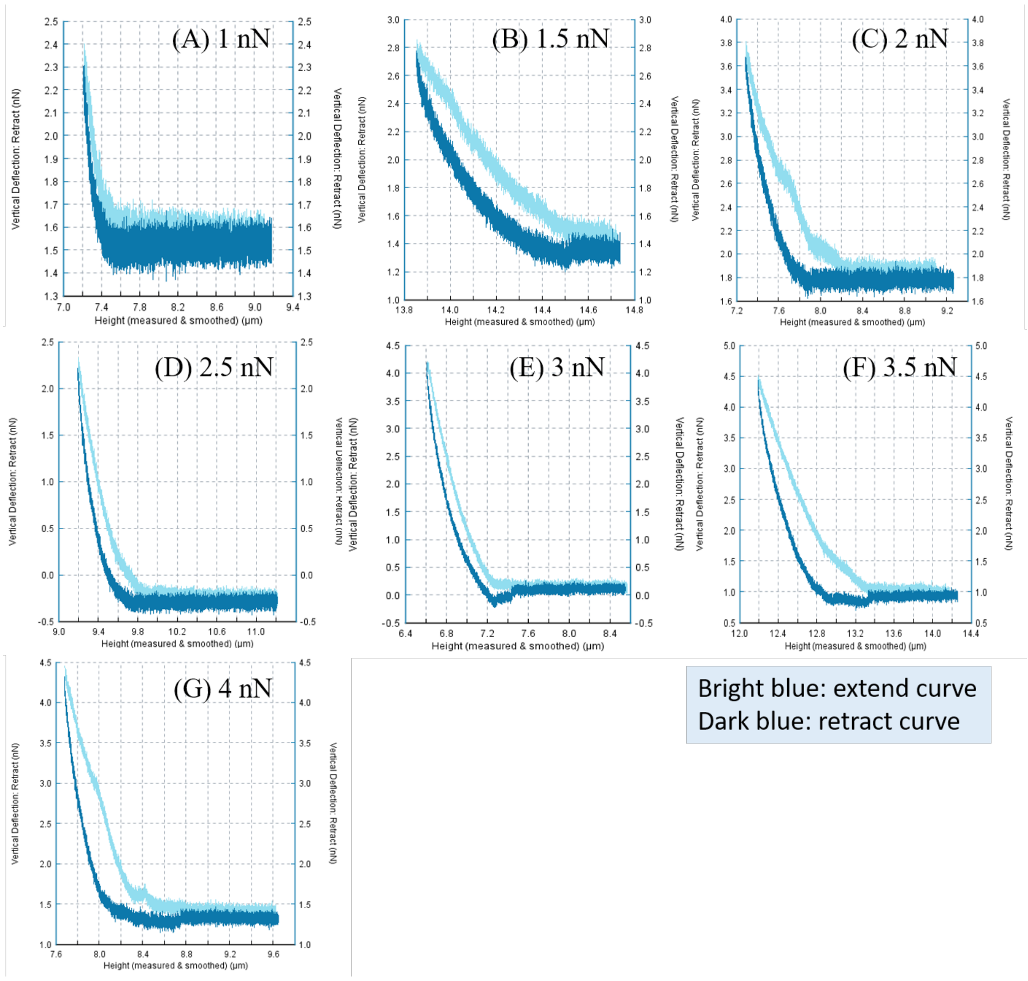

Figure 25: Force-indentation curves of the UD-SCC-1 nucleus applied with various forces (1 nN to 4 nN) at a constant scanning rate of 6 μm/s. The insufficient applied force of 1.5 nN does not properly influence nuclear deformations.

Figure 24 shows that the baseline of extend and retract force-indentation curves shifted when the scanning (indentation) speed was greater than 10 μm/s. The hydrodynamic effect appeared most at (pulling) speeds greater than 10 μm/s when they reached a similar order of magnitude to molecule forces [42]. The hydrodynamic drag force due to the viscous friction of the cantilever with the liquid. The offset is proportional to the velocities of the cantilever and is influenced when velocity is above 10 μm/s. Because of the effect, substantial errors could occur in AFM measurements of soft samples at low indentation depths [43].

The inherent nonlinearities in piezoelectric actuators, especially the hysteresis effect will lead to displacement errors in a horizontal direction in AFM scanning images [44]. The hysteresis varies according to the amplitudes of the applied voltage. A hysteresis loop becomes wider for greater amplitudes and depends on the input rate. As the frequency increases, the hysteresis loop gets wider [45]. The nonlinear relationship and hysteresis of piezo are corrected in one of two ways: closed-loop and open-loop. When Z closed loop is enabled, the non-linearities are corrected by the actual location of the scanner in the three-axis (X, Y, and Z) that continually correct the piezo voltage value during the experiment. In an open loop, the piezo voltage is increased and decreased in real-time to produce a linear scan in X and Y in both trace and retrace directions. In the AFM (NanoWizard 3) we used, the closed-loop introduces a small amount of noise that ensures data equality for imaging and force measurements in air and liquid.

Operating AFM with cantilever and sample immersed in liquid provides several advantages, including the reduction of Van der Waals forces, the elimination of capillary forces, and providing the ability to study biologically essential processes [46, 47]. However, AFM used to probe the living biological samples in the fluid medium (a surrounding media with certain viscosity) is difficult due to the hydrodynamic force on the tip deflection and the stability of the light intensity is significantly affected by the ingredients in liquids when the laser beam goes through the glass window and the liquid medium, as the viscosity and density may not be uniformly distributed in the environment. Operation in liquid presents additional complexity than for operation in air. Besides, the cantilever dynamics in the liquid environment remains little understood. Therefore, in this study, the AFM measurements in liquids were conducted with cautions to avoid potential problems and possible limitations.

4.1.2 Influence of cultivation substrates

For a better understanding of how physical attributes of the gel influence the AFM assessment of the cell elasticity. The measured elastic moduli of cells cultured on the substrates of different stiffness obtained from Hertz fits was investigated. Because of limited expansion capacity and a finite lifespan of primary cells, HOK cells, the immortalized UD-SCC-1 cells were chosen to show how substrates affect cell functions resulting in different biomechanical properties. The UD-SCC-1 cells were cultured on two different substrates, on clear plastic (which is made of high grade of polystyrene (PS)), and on gelatin-coated plastic (PS), respectively.

In order to represent the reality of tissue in the human body, a cell that is without any neighboring cells was not chosen, a cell surrounded by other adherent cells instead, to perform the indentation measurements. The UD-SCC-1 cells grow as a monolayer in a culture dish. However, it is difficult to draw a conclusion or establish an analysis only based on a few AFM measurements. A specific number of AFM measurements should be conducted to investigate cell mechanics, the minimum measurement number of twenty was suggested according to the statistical calculation [2].

The average elastic values are (3.4 ± 2.5) kPa and (2.6 ± 1.1) kPa for UD-SCC-1 cells cultured onto the substrates without coating and with gelatin-coating, respectively. Table 4 shows the average and median value of Young's modulus of UD-SCC-1 cells. Even though the difference in elastic modulus is not significant, the result shows that the physical factor (stiffness of substrate) slightly impacts the UD-SCC-1 cells' mechanical response. The boxplot and the histogram of UD-SCC-1 cells' Young's modulus are shown in Figure 26.

For further information, the elasticity of different regions, such as nuclear regions and peripheral regions were inspected as well. The cell peripheral regions are defined as the area without a nucleus. An average Young's modulus of (3.8 ± 2.3) kPa over UD-SCC-1 nucleus was obtained for the cells seeded on the uncoated surface, and ((3.1 ± 1.6)) kPa for those cells cultured on the gelatin-coated surface. The boxplot and the histogram of UD-SCC-1 nuclear Young's modulus are shown in Figure 27.

The elasticity results of UD-SCC-1 cells' peripheral regions on the uncoated substrate are significantly greater ((3.3 ± 1.7) kPa) from those cells on the gelatin-coated substrate ((2.4 ± 0.8) kPa) ($p < 0.001$, the p-value express the level of statistical difference). The boxplot and the histogram of UD-SCC-1 Young's modulus in cells' peripheral regions is shown in Figure 28.

---

[2] Pablo Emilio Verde

Table 4: The Young's modulus of human oral cancer cells cultured on different substrates.

Cell lines	Sample Origin	Average Young's modulus of cells' nuclei (kPa)	Average Young's modulus of cells' body (kPa)	Average Young's modulus of cells' peripheral regions (kPa)
UD-SCC-1 (on uncoated substrate)	Oropharynx (Tonsil)	3.8 ± 2.3 (n = 35)	3.4 ± 2.5 (n = 35)	3.3 ± 1.7 (n = 109)
UD-SCC-1 (on gelatin-coated substrate)	Oropharynx (Tonsil)	3.1 ± 1.6 (n = 45)	2.6 ± 1.1 (n = 45)	2.4 ± 0.8 (n = 124)
Cell lines	Sample Origin	Median Young's modulus of cells' nuclei (kPa)	Median Young's modulus of cells' body (kPa)	Median Young's modulus of cells' peripheral regions (kPa)
UD-SCC-1 (on uncoated substrate)	Oropharynx (Tonsil)	2.8 ± 2.3 (n = 35)	2.6 ± 2.5 (n = 35)	2.9 ± 1.7 (n = 109)
UD-SCC-1 (on gelatin-coated substrate)	Oropharynx (Tonsil)	2.8 ± 1.6 (n = 45)	2.3 ± 1.1 (n = 45)	2.3 ± 0.8 (n = 124)

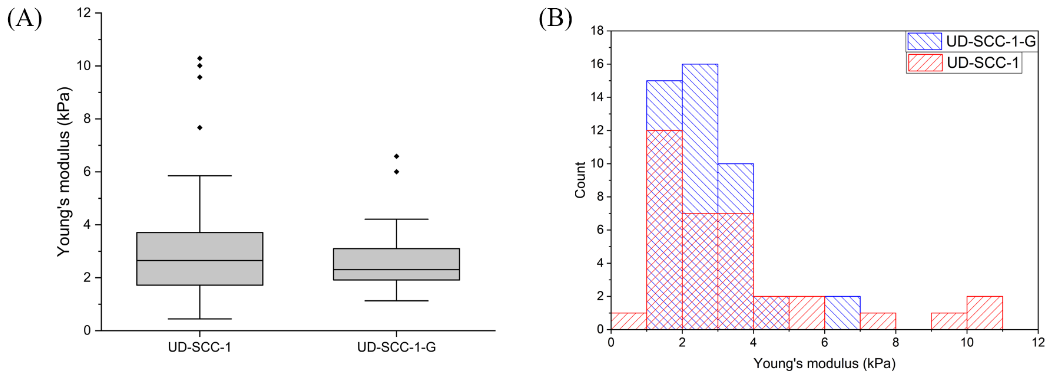

Figure 26: The boxplot and the histogram of UD-SCC-1 cells' Young's modulus. Cells cultured on stiff and soft substrates (A) The different substrates stiffness results in different cellular stiffness. But, the difference is not significant. (B) Histogram of elastic moduli of cells on the stiff substrate is boarder than on the soft substrate. UD-SCC-1-G: cells cultured on the gelatin-coated substrate; UD-SCC-1: cells seeded on the uncoated substrate.

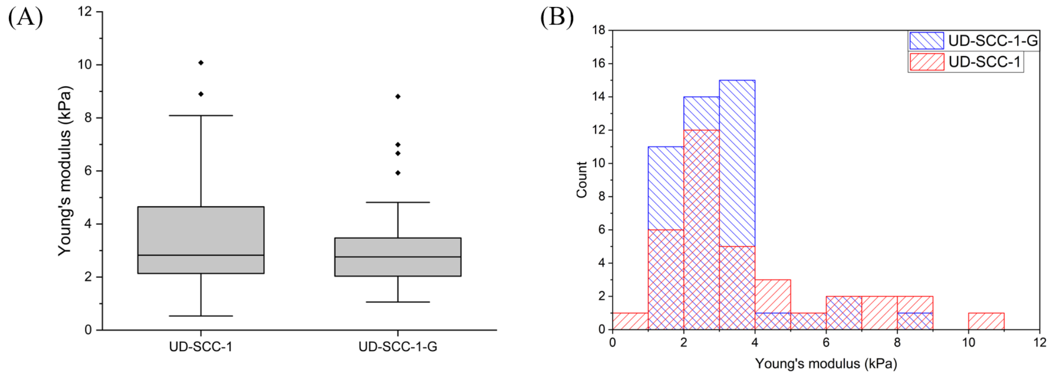

Figure 27: The boxplot and the histogram of UD-SCC-1 nuclear Young's modulus. (A) On the soft substrates, nuclei exhibit lower elastic moduli when compared to the cells on the stiff substrate. (B) Histogram of the elastic moduli is narrow cells on the soft substrate than those on the stiff substrate. UD-SCC-1-G: cells cultured on the gelatin-coated substrate; UD-SCC-1: cells seeded on the uncoated substrate.

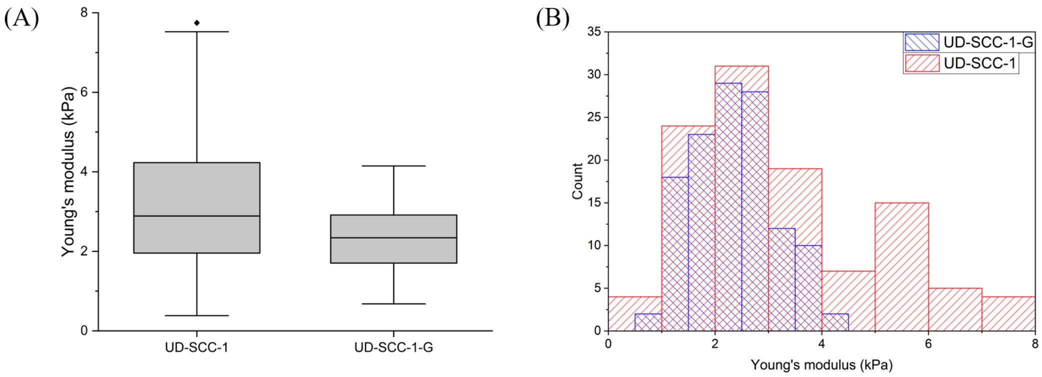

Figure 28: The boxplot and the histogram of UD-SCC-1 Young's modulus in cells' peripheral regions. (A) The cells cultured on soft substrates have a significantly lower elastic modulus when compared to the cells on the stiff substrate. (B) Histogram of the elastic moduli is boarder and wider when cells cultured on the stiff substrate than on the soft substrate. UD-SCC-1-G: cells cultured on the gelatin-coated substrate; UD-SCC-1: cells seeded on the uncoated substrate.

The UD-SCC-1 cells did sense two different surface cultivations, resulting in different Young's Moduli, and the cells slightly change their cell cytoskeleton morphology regarding the different substrates. The morphology of UD-SCC-1 cells was obtained by controlled poking with pyramidal indenter using AFM. In AFM images (Figure 29), UD-SCC-1 cells are spheroid in shape. On stiff substrates, UD-SCC-1 cells have stretched-out morphology. By contrast, cells on soft substrates are round, oval, or spherical.

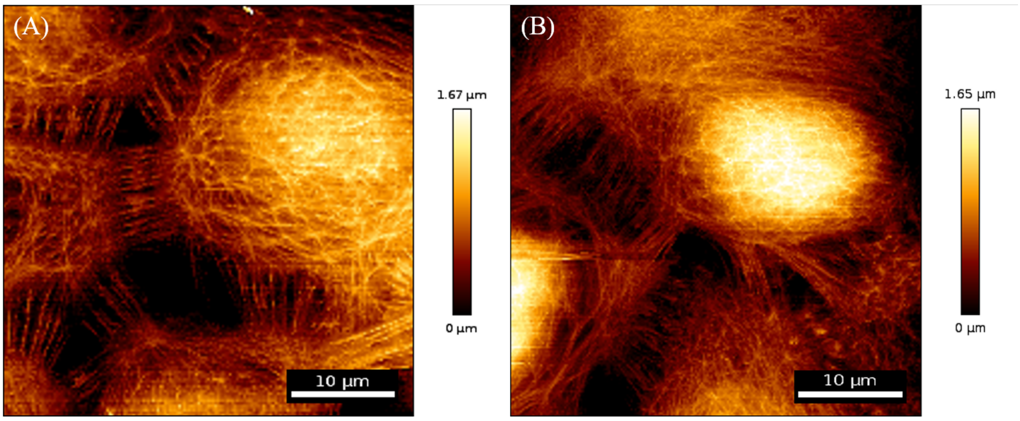

Figure 29: The topography of UD-SCC-1 cells. (A) UD-SCC-1 cells were cultured on an uncoated Petri dish; (B) UD-SCC-1 cells cultured on a gelatin-coated Petri dish. Actin filaments could be visualized by AFM in cells that UD-SCC-1 cells displayed more of a spread cellular shape on stiffer substrates.

In Figure 26, the data distributions of UD-SCC-1 cells exhibit a wide frequency band. The cells respond to the indentation, but the deformation may be complex because of the heterogeneous structure of living cells. The mechanical response of cells to the compression varies because of the complexity of the cytoplasm. The cytoplasm is composed of a cytoskeleton network and many proteins as well as organelles and vesicles to equilibrate the pressure applied on cells. The heterogeneous structures of living cells usually play a dominant role in leading the broad frequency distribution [50].

Many cultured cell types do not favor to adhere to uncoated glass and plastic surfaces, especially in low serum or serum-free conditions. A thin layer of gelatin hence is additionally added as a coating substrate onto the Petri dish for certain cell types (HOK is the one in our case) to enhance cell attachment and differentiation, whereas in general no specific surface modification (i.e. collagen matrices) is required for most of the cancerous cells. It has been reported that cells sense and respond distinctly to soft versus stiff substrates [51]. Cell morphology and functions can depend strongly on substrate stiffness. Since cell mechanical behavior can be altered using a substrate, the effect of the pattern of the substrate on cellular mechanical properties should be examined.

The cell morphology strongly depends on the stiffness of the substrate that has been inquired before [48, 49]. On stiff substrates, fibroblasts spread invariably greater and develop concentrated focal adhesion cluster and stress fibers of bundled F-actin as well as endothelial cells and human blood neutrophils. This may be a reasonable explanation for the dissimilar elasticity of UD-SCC-1 peripheral regions.

Studies reported that cells respond differently to the various flexibility of substrates [52]. Both epithelial cells and fibroblasts are capable of probing the stiffness of the substrate, and that proper mechanical feedback is required for regulation of the formation and dynamics of adhesion and cytoskeleton structure. The response of the cell to the substrate was suggested that originate at cell-substrate adhesion sites, where mechanical input might be translated into intracellular signals through the associated cytoskeleton or enzyme complexes [51]. Many cells, such as smooth muscle cells, epithelial cells, and 3T3 fibroblasts, are found to spread and organize with the stable focal adhesions (FAs) and cytoskeleton much on the rigid or stiff substrate. In contrast, a cell showed diffuse and dynamic adhesion complex on soft substrates [52, 53]. Changes in the stiffness of the underlying substrate of cells can affect their function (such as adhesion structures) as well as cell stiffness [54]. Also, the structure of substrates affects cellular mechanical behavior and morphology, simultaneously [55]. In another word, biomechanical behavior can be directly altered by the substrate topography.

The AFM cantilever usually approaches a surface and is used to apply local forces to living cells to quantify force transduction through the cytoarchitecture to measure cell mechanics. In other cases, researchers can also use the AFM tip to pull on cell surface molecules for studies of biomolecular interactions on a single molecular scale, adhesion of living cells, for instance [56, 57]. In this section, we are interested in how the physical factors affect the elastic measurements of living cells using AFM, the physical factors including the indenting force, the scanning rate, the geometry of probing tips, and operating temperature. Several studies have reported that the geometric difference of cantilever tip affects precision in AFM stiffness measurements. Indentation measurements with pyramidal tips often lead to an overestimation of elastic modulus, while colloidal tips should be used for mechanical characterization [58, 59]. In this study, the elastic moduli of cells were performed by indentating cells with a colloidal probe, and the Young's modulus is quantified from the recording cantilever deflection while deforming the cell. The UD-SCC-1 cells not only modify their morphology with regards to the different substrates but also respond differently to the different substrates result in different Young's modulus. The decrease in Young's modulus of UD-SCC-1 cells cultured onto the gelatin-coated substrate is observed. Hence, for the following AFM measurements, operating on the same background is utilized to observe the living cells' behavior.

Human and mammalian cell lines are maintained at 36°C to 37°C for optimal growth. Rising temperature or dropping temperature can cause denaturation of proteins and disturbance of cell regulation [60, 61].The AFM measurements were performed in liquid at room temperature within two hours to ensure cell viability. Because physical cues influence the AFM assessment, the elasticity measurements in the following sections, are conducted with the colloidal tips and applied with the optimized force value (depends on cell line) on the sample surface at an optimized scanning rate of $6\,\mu$m/s (between $2.5\,\mu$m/s and $10\,\mu$m/s) to study the mechanical response of cells. And the QI mode, a special mode from JPK Wizard 3 AFM system, was chosen to carry out the contact-mode AFM imaging in order to get high-quality imaging data.

4.2 Human oral cells

Cell mechanics is a novel label-free biomarker for indicating cell states and pathological changes. Abnormal cells have different characteristics compared to normal (healthy) cells in terms of morphology, cell growth rate, cell-cell interactions, cell-extracellular interactions, and cytoskeletal organization. AFM is an established technique in biological research for differentiating the mechanical properties of various cell types. AFM permits quantitative high resolution, a non-destructive image of biosample surfaces. In addition, AFM operating in many different modes offers a vast amount of information about bio-samples ranging from topography to mechanical properties characterization. By means of the AFM technique, the cytoskeleton network changing during the disease progression which is closely associated with the biomechanics can be confirmed.

4.2.1 Different disease states of head and neck squamous cells

The oral cells were cultured on the gelatin-coating substrate, and elasticity experiments using the AFM technique were performed to characterize cell deformation. In AFM, the elastic properties of living cells are delivered from indentation experiments and described quantitatively by Young's modulus defined here as a measure of cellular deformability. During AFM measurements, the sharp pyramidal tip on the spring was used to push against the cell surface for cellular imaging, whereas colloidal probes were used for mechanical characterization.

The Young's modulus was obtained by fitting the force-indentation curves with the Hertz model. Table 5 shows the average and median value of Young's modulus of human oral cells with different cancer stages. Turkey's test presents that the average Young's modulus of the HOK cells ((4.6 ± 2.2) kPa) is significantly different from that of the DOK cells ((2.5 ± 0.9) kPa). The HOK cells are distinctly different from four of the oral cancerous cells: UD-SCC-1 ((2.6 ± 1.1) kPa), UD-SCC-2 ((1.9 ± 0.9) kPa), UD-SCC-4 ((2.1 ± 0.7) kPa), UD-SCC-6 ((2.6 ± 1.1) kPa), UT-SCC-14 ((2.0 ± 1.1) kPa). There is a substantial difference in elastic values between the HOK cells and the UT-SCC-24B cells ((1.5 ± 0.5) kPa). For visualizing and describing numerical data, the boxplot and the histogram of oral cells' Young's modulus are shown in Figure 30.

A similar trend in Young's modulus is observed that the average elastic value of HOK nuclei ((5.6 ± 2.7) kPa) is higher than pathological oral cells: DOK ((3.4 ± 1.8) kPa), UD-SCC-1 ((3.1 ± 1.6) kPa), UD-SCC-2 ((2.5 ± 1.6) kPa), UD-SCC-4 ((2.6 ± 0.9) kPa), UD-SCC-6 ((3.7 ± 1.7) kPa), UT-SCC-14 ((2.9 ± 2.0) kPa) and UT-SCC-24B ((2.0 ± 0.9) kPa). The boxplot and the histogram of nuclear Young's modulus of oral cells are shown in Figure 31.

The Young's modulus in peripheral regions of healthy HOK cells ((3.6 ± 1.8) kPa) is once again stiffer than that of the dysplastic cells (DOK: (2.0 ± 1.8) kPa)), cancerous cells (UD-SCC-1: (2.8 ± 0.8) kPa, UD-SCC-2: (1.4 ± 0.6) kPa, UD-SCC-4: (2.1 ± 0.7) kPa, UD-SCC-6: (2.3 ± 1.0) kPa and UT-SCC-14: (1.3 ± 0.5) kPa) and metastatic cells (UT-SCC-24B: (1.2 ± 0.3) kPa).The boxplot and the histogram of Young's modulus in cells' peripheral regions of oral cells are shown in Figure 32.

Table 5: The Young's modulus of human oral cells with different cancer stages.

Cell lines (on gelatin-coated substrate)	Sample Origin	Average Young's modulus of cells' nuclei (kPa)	Average Young's modulus of cells' body (kPa)	Average Young's modulus of cells' peripheral regions (kPa)
UD-SCC-1	Oropharynx (Tonsil)	3.1 ± 1.6 (n = 45)	2.6 ± 1.1 (n = 45)	2.4 ± 0.8 (n = 124)
UD-SCC-2	Hypopharynx	2.5 ± 1.6 (n = 41)	1.9 ± 0.9 (n = 44)	1.4 ± 0.6 (n = 116)
UD-SCC-4	Oropharynx (Tongue)	2.6 ± 0.9 (n = 35)	2.1 ± 0.7 (n = 35)	2.1 ± 0.7 (n = 100)
UD-SCC-6	Oral cavity (Tongue)	3.7 ± 1.7 (n = 34)	2.6 ± 1.1 (n = 36)	2.3 ± 1.0 (n = 103)
UT-SCC-14	Oral cavity (Tongue)	2.9 ± 2.0 (n = 38)	2.0 ± 1.1 (n = 40)	1.3 ± 0.5 (n = 111)
UT-SCC-24B	Oral cavity (Tongue)	2.0 ± 0.9 (n = 27)	1.5 ± 0.5 (n = 30)	1.2 ± 0.3 (n = 79)
DOK	Dorsal tongue	3.4 ± 1.8 (n = 36)	2.5 ± 0.9 (n = 34)	2.0 ± 1.8 (n = 96)
HOK	Oral mucosa	5.6 ± 2.7 (n = 40)	4.6 ± 2.2 (n = 40)	3.6 ± 1.8 (n = 125)

Cell lines (on gelatin-coated substrate)	Sample Origin	Median Young's modulus of cells' nuclei (kPa)	Median Young's modulus of cells' body (kPa)	Median Young's modulus of cells' peripheral regions (kPa)
UD-SCC-1	Oropharynx (Tonsil)	2.8 ± 1.6 (n = 45)	2.3 ± 1.1 (n = 45)	2.3 ± 0.8 (n = 124)
UD-SCC-2	Hypopharynx	2.1 ± 1.6 (n = 41)	1.5 ± 0.9 (n = 44)	1.3 ± 0.6 (n = 116)
UD-SCC-4	Oropharynx (Tongue)	2.5 ± 0.9 (n = 35)	2.0 ± 0.7 (n = 35)	2.0 ± 0.7 (n = 100)
UD-SCC-6	Oral cavity (Tongue)	3.6 ± 1.7 (n = 34)	2.6 ± 1.1 (n = 36)	2.1 ± 1.0 (n = 103)
UT-SCC-14	Oral cavity (Tongue)	2.3 ± 2.0 (n = 38)	1.8 ± 1.1 (n = 40)	1.3 ± 0.5 (n = 111)
UT-SCC-24B	Oral cavity (Tongue)	1.8 ± 0.9 (n = 27)	1.4 ± 0.5 (n = 30)	1.2 ± 0.3 (n = 79)
DOK	Dorsal tongue	2.9 ± 1.8 (n = 36)	2.3 ± 0.9 (n = 34)	1.6 ± 1.8 (n = 96)
HOK	Oral mucosa	5.2 ± 2.7 (n = 40)	4.6 ± 2.2 (n = 40)	3.3 ± 1.8 (n = 125)

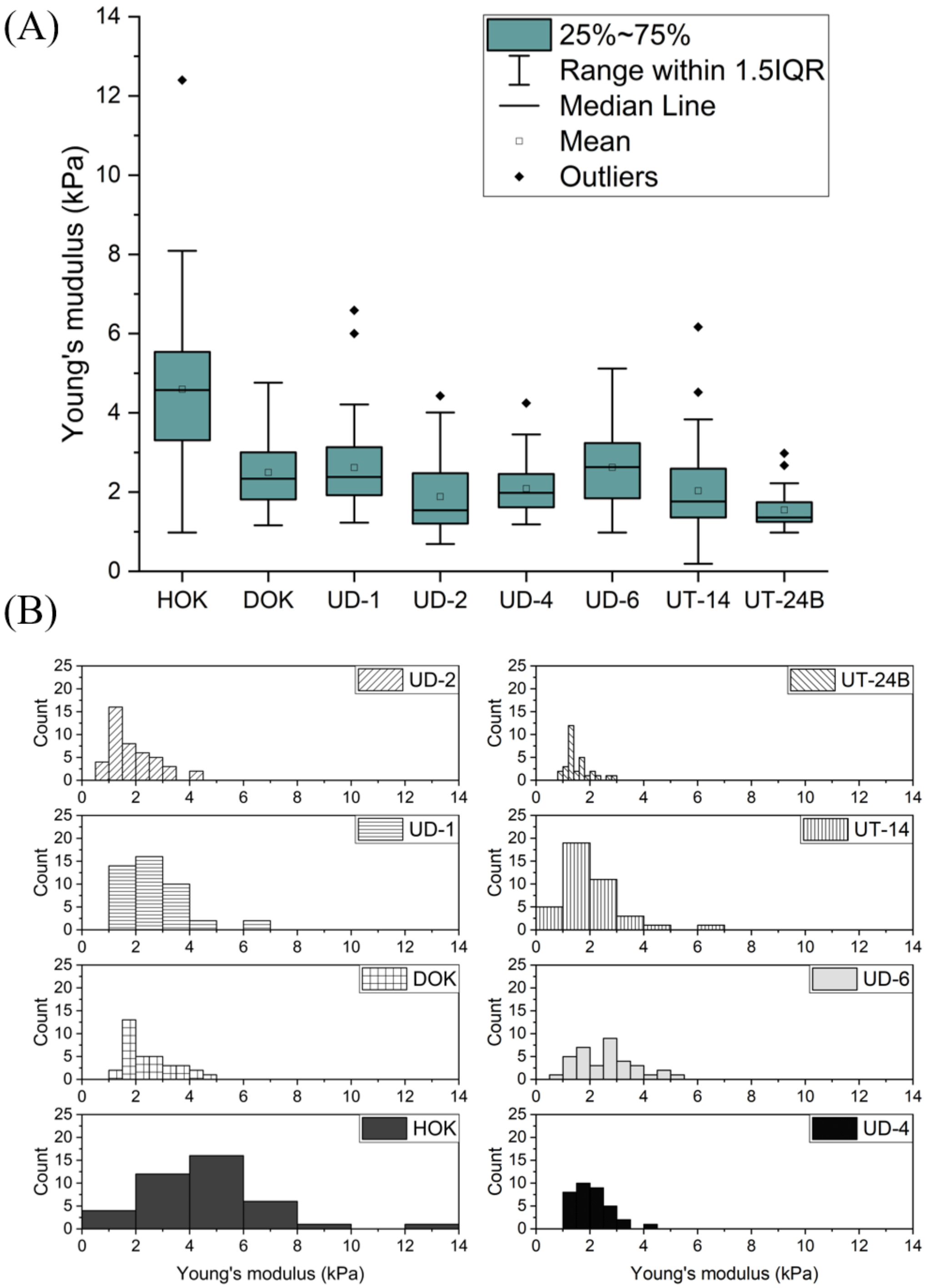

Figure 30: The boxplot and the histogram of oral cells' Young's modulus. (A) The UT-24B boxplot is condensed which presents more consistent values, whereas the HOK boxplot shows a longer length of boxplot that values in the boxplot various quite a bit. The range of Young's modulus of cancerous oral cells is overlapping. (B) A clear peak at 5 kPa occurs in the data distribution of HOK cells.

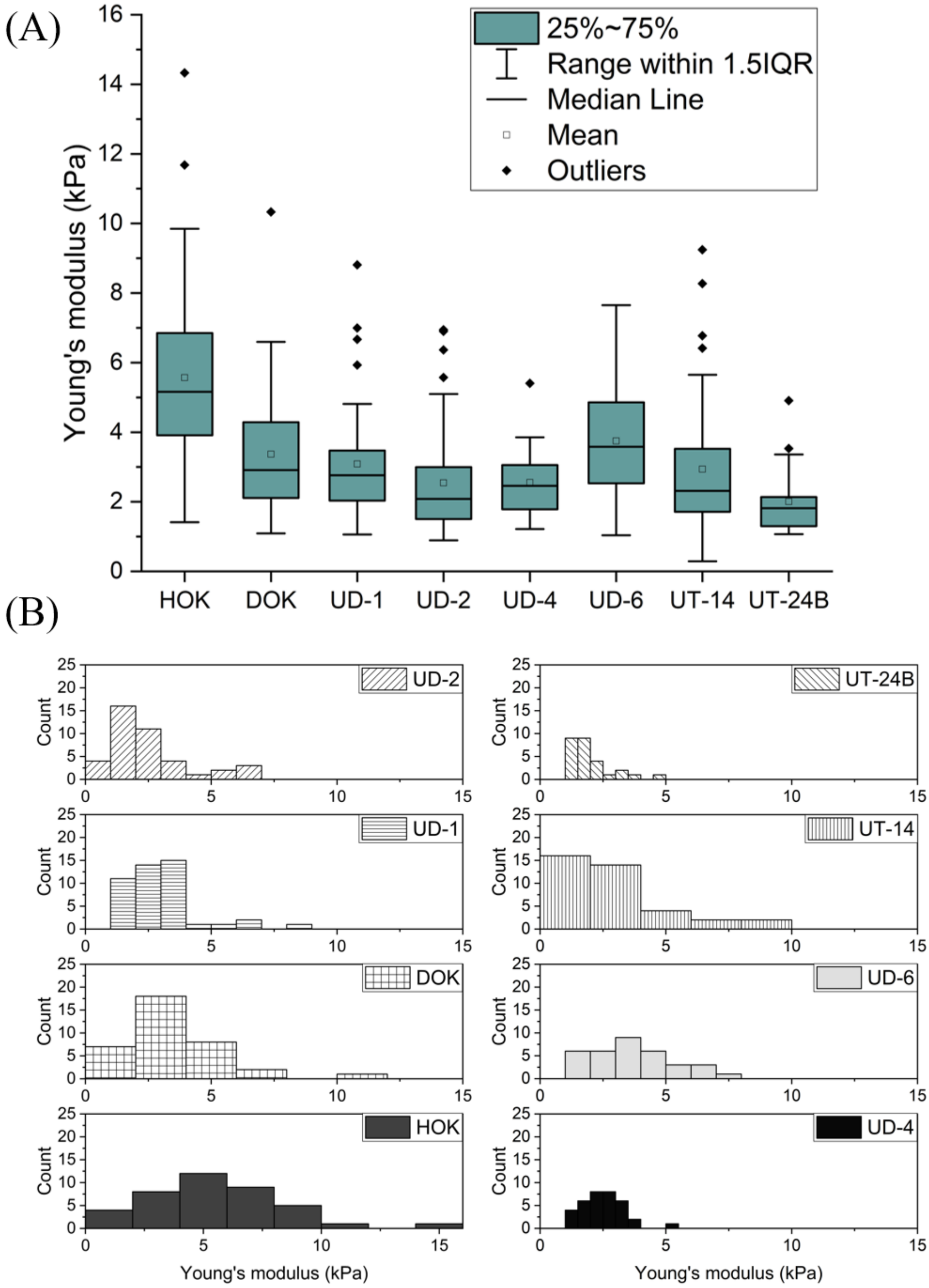

Figure 31: The boxplot and the histogram of nuclear Young's modulus. (A) The HOK has more spread both by the interquartile (IQR) range and the range. The variation of other oral cells is less with a narrow box. (B) The data distribution of HOK cells has a peak at 5 kPa, while data distributions of pathological cells have peaks at about 2 kPa

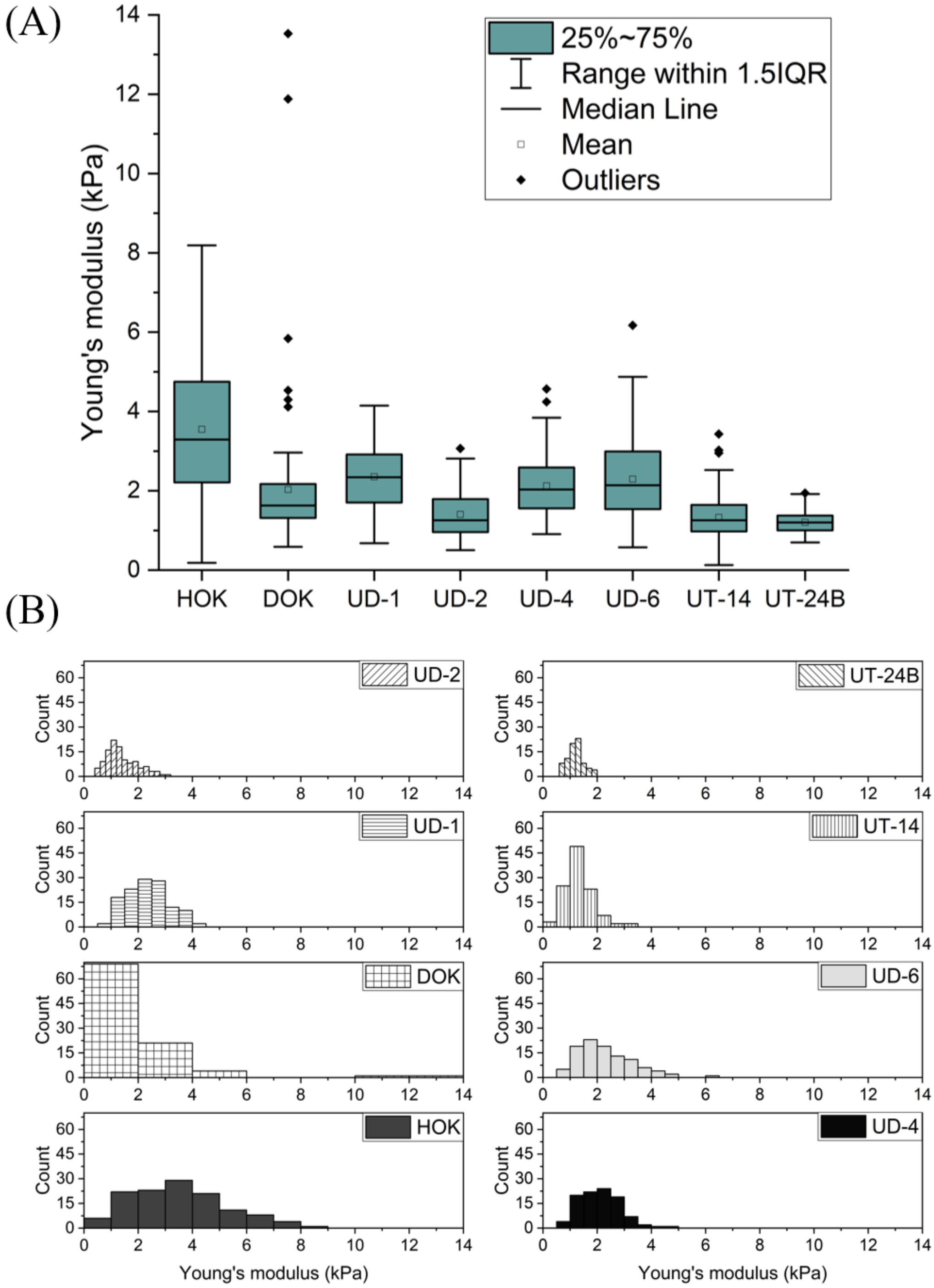

Figure 32: The boxplot and the histogram of Young's modulus in cells' peripheral regions. (A) The median value of healthy oral cells is higher than that of pathological oral cells. The level of variation of the healthy oral cells is high. (B) The pathological cells represent narrow data distributions, while the data distribution of HOK cells is boarder.

The dysplastic DOK cells are significantly stiffer than the metastatic UT-SCC-24B cells, but the DOK cells are significantly softer than the healthy HOK cells. Before cancer cells form in tissues of the body, the cells go through abnormal changes called hyperplasia (abnormal multiplication of cells) and dysplasia (abnormal changes in cellular shape, size, and organization). Moderate and severe dysplasia is considered precursors of cancers because of the high risk for progression to carcinoma. Cytological and architectural alterations are two features of oral epithelial dysplasia reflecting the loss of normal maturation and stratification pattern of the surface epithelium [62]. The cytoskeleton network can be readily revealed in living cells with AFM imaging. Indenting through the plasma membrane, the actin network and dense on the cellular surface can be displayed using AFM. The microtubules are generally concentrated at the deeper layer of cells compared to superficial layers and therefore it is difficult to detect under the imaging forces used [63].

From the AFM images, healthy HOK cells seem to process a pronounced network of actin filaments compared to dysplastic DOK cells. The sub-membrane structure of the HOK cells exhibits well-aligned actin filamentous structure as compared with the DOK cells where the F-actins appear as a randomly organized network and bundles are thinner. There is a distinguished cellular structural feature as healthy HOK cells transform to dysplastic DOK cells, which is manifested with a corresponding change in the mechanical properties. The topography of oral cells is shown in Figure 33.

The increasing deformability as compared to healthy cells due to biochemical alterations resulting from the onset of the disease: cancer. The determination of cell deformability indicates the potential use of Young's modulus as a quantitative biomarker of cancer-related changes.

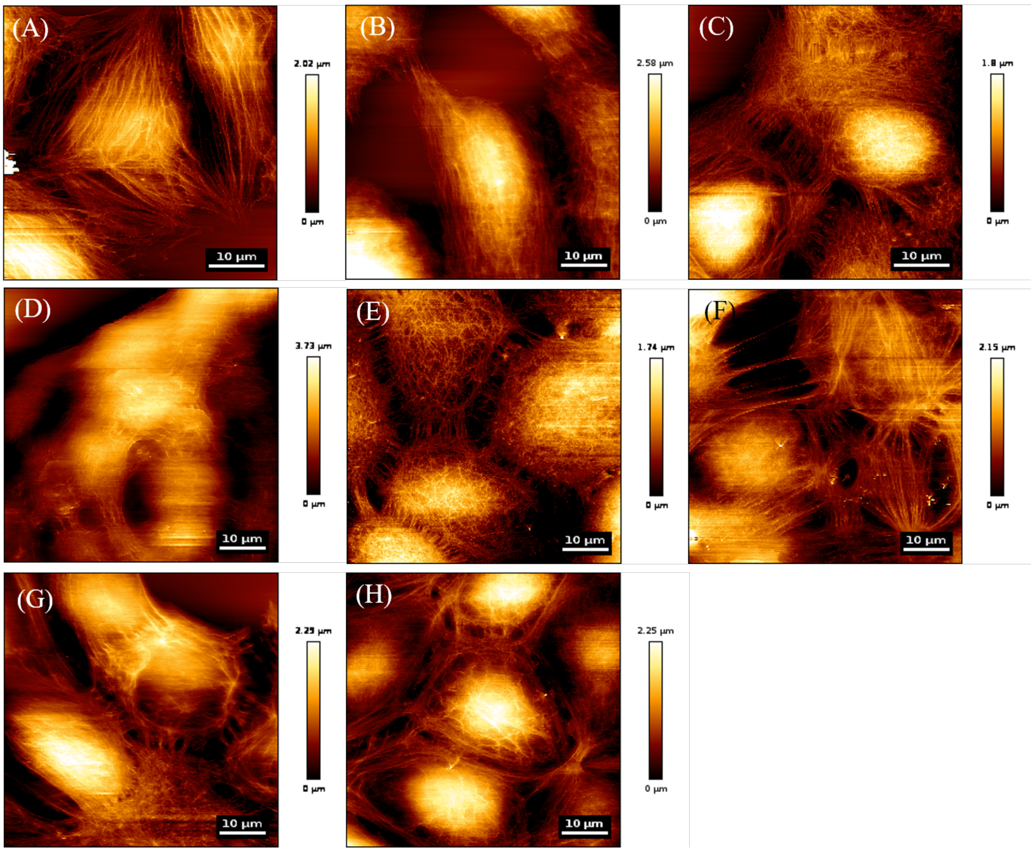

Figure 33: The topography of oral cells: (A) HOK (B) DOK (C) UD-SCC-1 (D) UD-SCC-2 (E) UD-SCC-4 (F) UD-SCC-6 (G) UT-SCC-14 (H) UT-SCC-24B cells. Healthy oral cells possess a denser, well-aligned F-actin with longer stress fibers relative to diseased oral cells. Benign, cancerous, and metastatic cells appear as a randomly organized actin network.

The data distribution of Young's modulus (Figure 30(B)) exhibits the narrowest distribution in metastatic cancer cells (UT-SCC-24B) comparing to the dysplastic cells (DOK) and the cancerous cells (UD-SCC1, UD-SCC-2, UD-SCC-4, UD-SCC-6, and UTSCC-14). In contrast, the normal cells (HOK) display a wide distribution of Young's Modulus. The metastatic cancer cells (UT-SCC-24B) are 40 % softer than dysplastic cells (DOK), and dysplastic cells (DOK) are 46 % softer than healthy cells (HOK). The outcome is due to the changes to the cell subcellular structure. The reduced stiffness of these metastatic cancer cells is due to a remarkable reduction in the well-defined F-actin filaments or their bundles (stress fibers), which results in a weaker cytoskeletal structure. The cytoskeletal remodeling is the major contributor to the observed differences in cell stiffness. A significant reduction in the thickness of F-actin cables and bundles was previously reported for different types of cancer cells, ovarian cells, dermal fibroblast cells, and breast cells [64, 65, 66].

The metastatic UT-SCC-24B cells have the smallest value of Young's modulus, with a narrow distribution, indicating a soft cellular structure (Figure 30(A)). Interestingly, the width distribution (Figure 30(B)) of elastic constants measured for each cell line gradually decreases with the increasing disease grades (in the order of healthy, dysplastic, cancerous, metastatic). The highly malignant cells might represent a good compromise in heterogeneous structures, and cytosol and cytoskeleton are less structured than their healthier counterparts, leading to a homogeneous cell body.

The correlation between fibrous structures and cellular elasticity has been discussed in detail [67, 68]. Studies have shown that cytoskeletal morphology directly controls cellular mechanical behavior [69]. The cellular cytoskeleton, composed of F-actin (actin filaments), microtubules, and intermediate filaments, is a highly cross-linked and dynamic network present in all cells cytoplasm [70, 71]. The three cytoskeletal components are organized into networks that resist deformation but can reorganize in response to externally applied forces, and they have important roles in arranging and maintaining the integrity of intracellular compartments. The polymerization and depolymerization of actin filaments and microtubules generate directed forces that drive changes in cell shape and, together with molecular motors that move along the actin filaments and microtubules, guide the organization of cellular components [72]. In addition, the effect of multiple drugs disrupting or stabilizing the integrity of different components of the cytoskeleton on the elasticity of two fibroblast cell lines was investigated by using the atomic force microscope (AFM) [68]. Among the two main types of cytoskeletal polymer, the actin network has a large contribution to cell integrity, or elasticity was suggested.

The cytoskeleton, an internal polymer network, in particular, determines a cells mechanical strength and morphology. The cytoskeleton evolves during the normal differentiation of cells, is involved in many cellular functions, and is characteristically altered in many diseases, including cancer [73]. In cancer cells, the cellular architecture is substantially modified by changes in associated protein and functional activity. As a consequence, cancer cells have distinctive mechanical properties from normal cells.

4.2.2 Non-metastatic head and neck squamous carcinoma cells

The stiffness of mammalian cells, as measured with AFM, varied from a few hundred Pa to a few kPa [74, 75, 76]. We measured the oral cell compressive strain to evaluate the Young's modulus; the measured values ranged from 1.5 to 4.6 kPa. We have already tried to avoid the possible physical factors which directly influence the AFM assessment. The quantitative discrepancy in elastic moduli depends on cells' disease stages, however, may also depend on the cells' inherent characteristics, such as cell origins, cell shape, and cell size. In this section, different non-metastatic HNSCC cell lines originating from different origins were investigated to show whether the inherent characteristics reflect an influence on the cellular stiffness.

The UD-SCC-1, the UD-SCC-2 cell lines originate from different lesions of the tonsil, of the hypopharynx, respectively. The UD-SCC-4, the UD-SCC-6, and the UT-SCC-14 cell lines are derived from squamous cell carcinomas of the tongue. The dissimilarity in origins might affect the elastic moduli. The results show that the UD-SCC-2 cells ((1.9 ± 0.9) kPa) are significantly softer than the UD-SCC-1 cells ((2.6 ± 1.1) kPa), and the UD-SCC-2 cells are also significantly softer than the UD-SCC-6 cells ((2.6 ± 1.1) kPa). No significant difference among the average Young's modulus of UD-SCC-1, of UD-SCC-4 ((2.1 ± 0.7) kPa), of UD-SCC-6, and the UT-SCC-14 ((2.0 ± 1.1) kPa) is found. The UD-SCC-4, UD-SCC-6, and UT-SCC-14 cell lines are all derived from patients' tongues expect the UD-SCC-1 cell line originates from the tonsil. Despite different cell origins, similar actin filament networks may cause similar cell elastic values. The boxplot and the histogram of cancerous cells' Young's modulus are shown in Figure 34.

The UD-SCC-2 cells have the smallest whole cell volume appearing smaller cellular radius while bigger cell size is observed in other cancerous oral cells. The UD-SCC-2 cells differ not only in their cell origin but also in cell size from other cancerous cell lines. These differences directly contribute to the smallest mechanical stiffness. The topography of oral cancerous cells is shown in Figure 35.

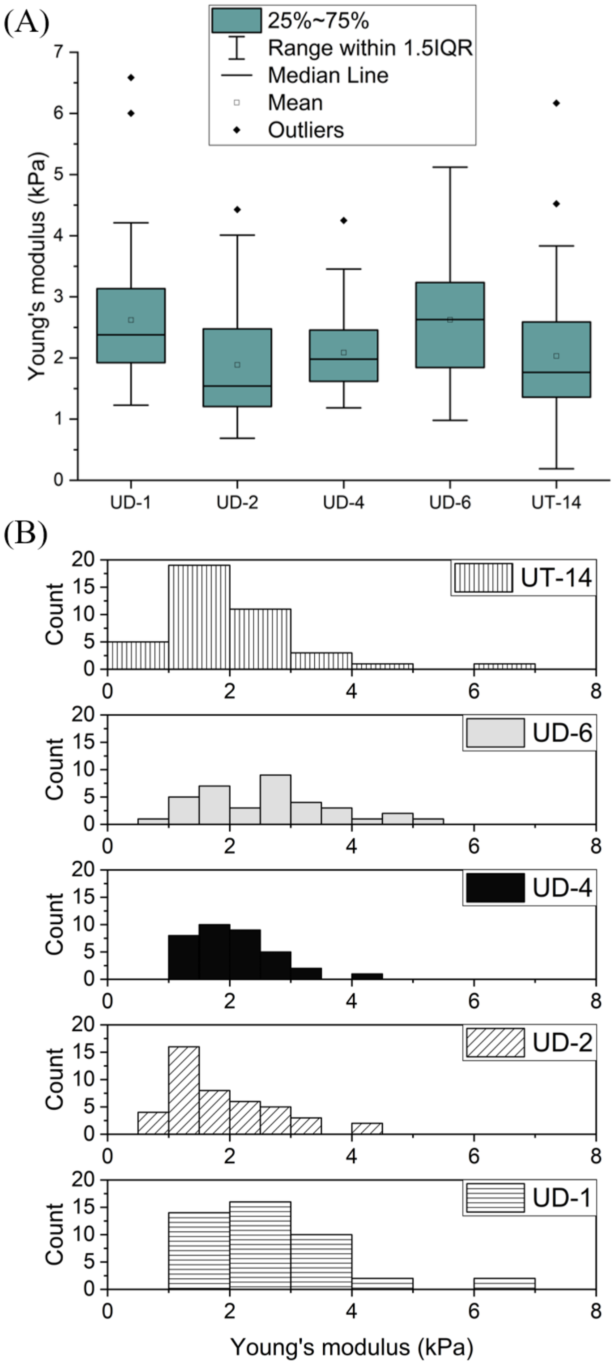

Figure 34: The boxplot and the histogram of cancerous cells' Young's modulus. (A) cancerous cells' Young's modulus reflects an interesting difference. Although the range of values is overlapping and somewhat comparable. The measures of central tendency are much lower in the UD-2 as compared to the UD-6 and UD-1. (B) The distribution of UD-4 cells is narrowest as compared to other cancerous oral cells.

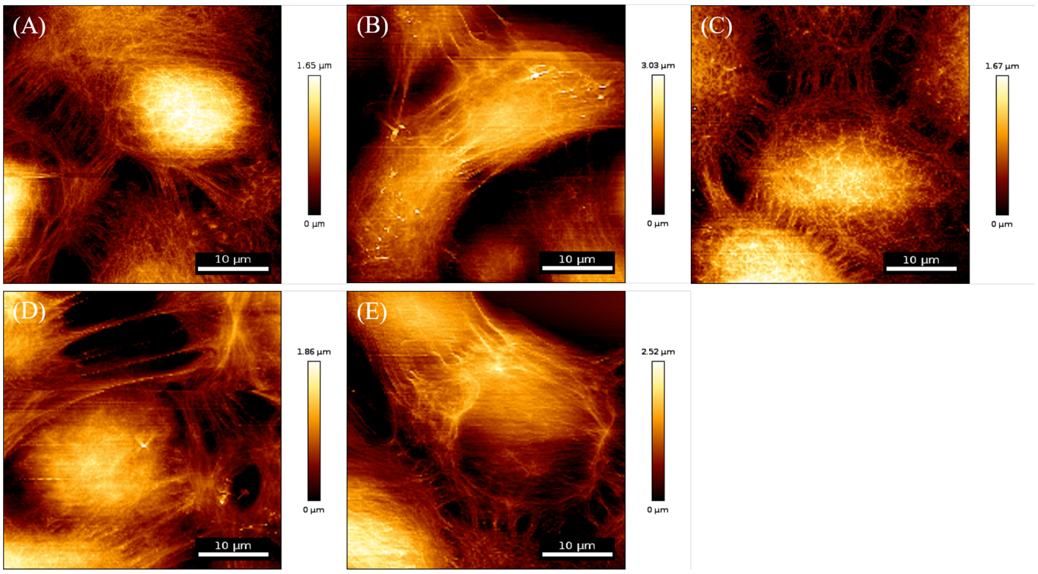

Figure 35: The topography of oral cancerous cells. (A) UD-SCC-1 (B) UD-SCC-2 (C) UD-SCC-4 (D) UD-SCC-6 (E) UT-SCC-14 cells. The actin filament structure of cancerous oral cells is various. Some of them exhibit dot-like filamentous network, while others organize with long-strands stress fibers.

Our results present that no significant difference in nuclear Young's modulus of UD-SCC-1 ((3.1 ± 1.6) kPa), of UD-SCC-2 ((2.5 ± 1.6) kPa), of UD-SCC-4 ((2.6 ± 0.9) kPa) and of UT-SCC-14 ((2.9 ± 2.0) kPa). Nevertheless, UD-SCC-6 nuclei ((3.7 ± 1.7) kPa) are significantly stiffer than both UD-SCC-2 nuclei and UD-SCC-4 nuclei. During the cell culture process, UD-SCC-6 cells clumped together, instead of as a monolayer growth, observed with optical microscopy. Despite during the sample preparation, the UD-SCC-6 cells and UD-SCC-4 cells have been filtered with cell strainer, cell clumping could still occur and further influence the AFM assessment. The boxplot and the histogram of nuclear Young's modulus of cancerous cells are shown in Figure 36.

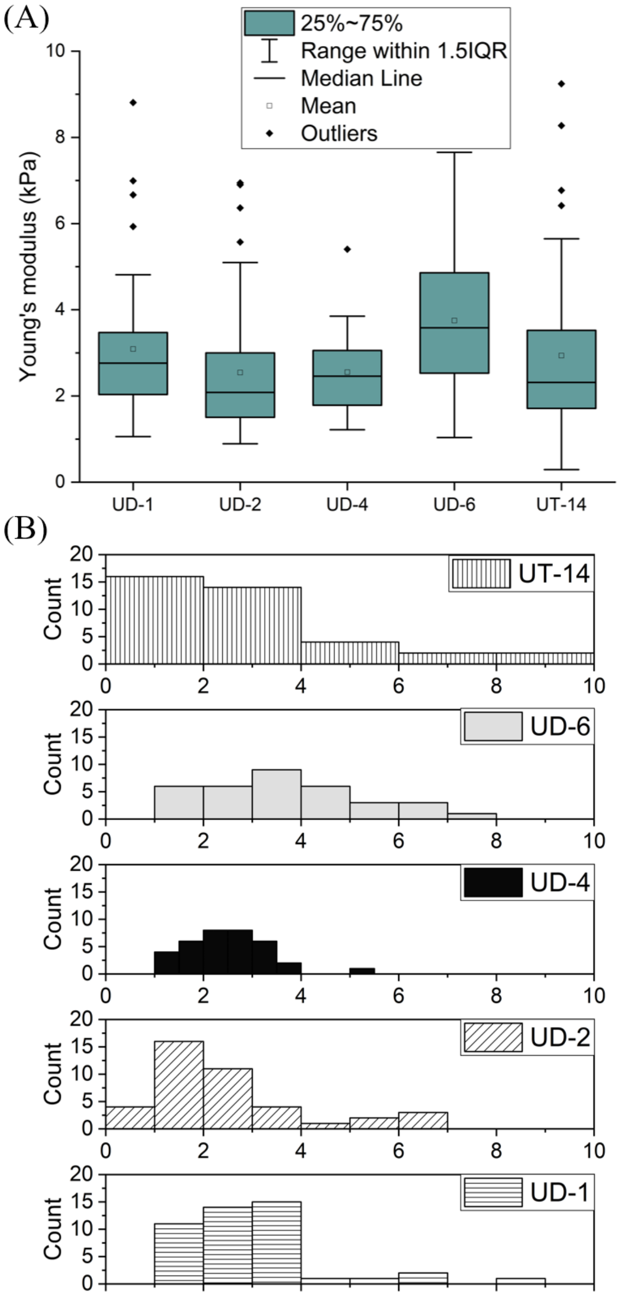

Figure 36: The boxplot and the histogram of nuclear Young's modulus. (A) The boxplot of the UD-6 is more spread out than the rest. The Young's value for UD-6 cells is comparable to the value of the UD-1 and of the UT-14. The data for the UD-6 boxplot is significantly higher than the values for the boxplot of data of the UD-2 and the UD-4. (B) The distribution of UD-4 cells is narrowest as compared to other cancerous oral cells.

We cannot find a clear connection or reasonable explanation for the stiffness of cancerous oral cells in peripheral regions. The peripheral regions are the most complex structures within the cells, the complexity resulting in the inhomogeneous results. But cancerous cells' peripheral regions are softer than cancerous cells' nuclei are observed. The boxplot and the histogram of Young's modulus in cells' peripheral regions of cancerous cells are shown in Figure 37.

Our results indicate that the Young's Modulus is influenced by the cells' features, especially the sample origin, the cell size, and the cell shape. The filamentous structures of oral cancer cells, detected by AFM imaging mode, reveal cancerous cells are comprised of a randomly organized actin network and short actin segments that leading to a weaker cytoskeleton.

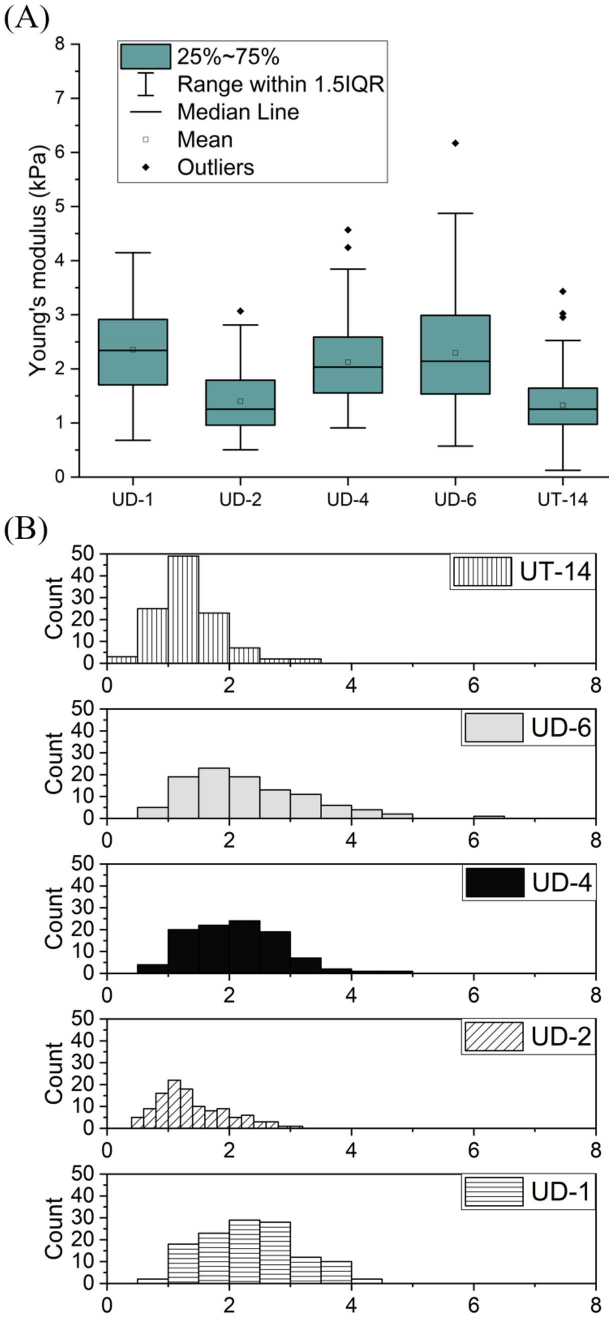

Figure 37: The boxplot and the histogram of Young's modulus in cells' peripheral regions. (A) The median value for the UD-1 is the highest. (B) The Young's modulus of the UD-1, the UD-4, and the UT-14 represent a relatively normal or bull-shaped distribution, while the shape of the UD-2 and the UD-6 is skewed.

4.2.3 Different disease states of tongue squamous carcinoma cells

AFM measurements measure the cell mechanical properties and reflect the real cytoskeletal alternations across different conditions. The measurements are influenced by the experimental conditions (the load speed, the number of force recorded at one place) from AFM, the stiffness of the substrates, and the cell's inherent characteristics. Hence, the elastic measurements were conducted under the same experimental conditions, such as same scanning speed, same cell culture substrates, and so on. We performed a comparative analysis of the elastic modulus derived from the indentation data obtained with AFM on human oral cells (both healthy and cancerous), and the oral cell lines derived from the same origin (tongue cancer) were used.

The forces curves were analyzed with the Hertz model to determine the values of Young's modulus. The HOK cells ((4.6 ± 2.2) kPa) are significantly stiffer than dysplastic cells (DOK: (2.5 ± 0.9) kPa), and cancerous cells (UD-SCC-4: (2.1 ± 0.7) kPa, UD-SCC-6: (2.6 ± 1.1) kPa and UT-SCC-14: (2.0 ± 1.1) kPa). HOK cells are also stiffer than metastatic cells (UT-SCC-24B: (1.5 ± 0.5) kPa). Metastatic UT-SCC-24B cells present a significant difference in Young's Modulus comparing with HOK cells, DOK cells, and UD-SCC-6 cells. The data distribution of cancerous UT-SCC-14 cells shows the widest range of up to 7 kPa while there is no occurrence of Young's moduli greater than 3 kPa for metastatic cells (UT-SCC-24B). The boxplot and histogram of tongue cells' Young's modulus are given in Figure 38.

Evaluating the elasticity of tongue cells' nuclei was carried out as well. The average E value of the HOK nuclei is (5.6 ± 2.7) kPa. The HOK nuclei are significantly stiffer than pathological cells' nuclei (DOK: (3.4 ± 1.8) kPa; UD-SCC-4: (2.6 ± 0.9) kPa; UD-SCC-6: (3.7 ± 1.7) kPa; UT-SCC-14: (2.9 ± 2.0) kPa; UT-SCC-24B: (2.0 ± 0.9) kPa).The boxplot and histogram of nuclear Young's modulus of tongue cells are shown in Figure 39.

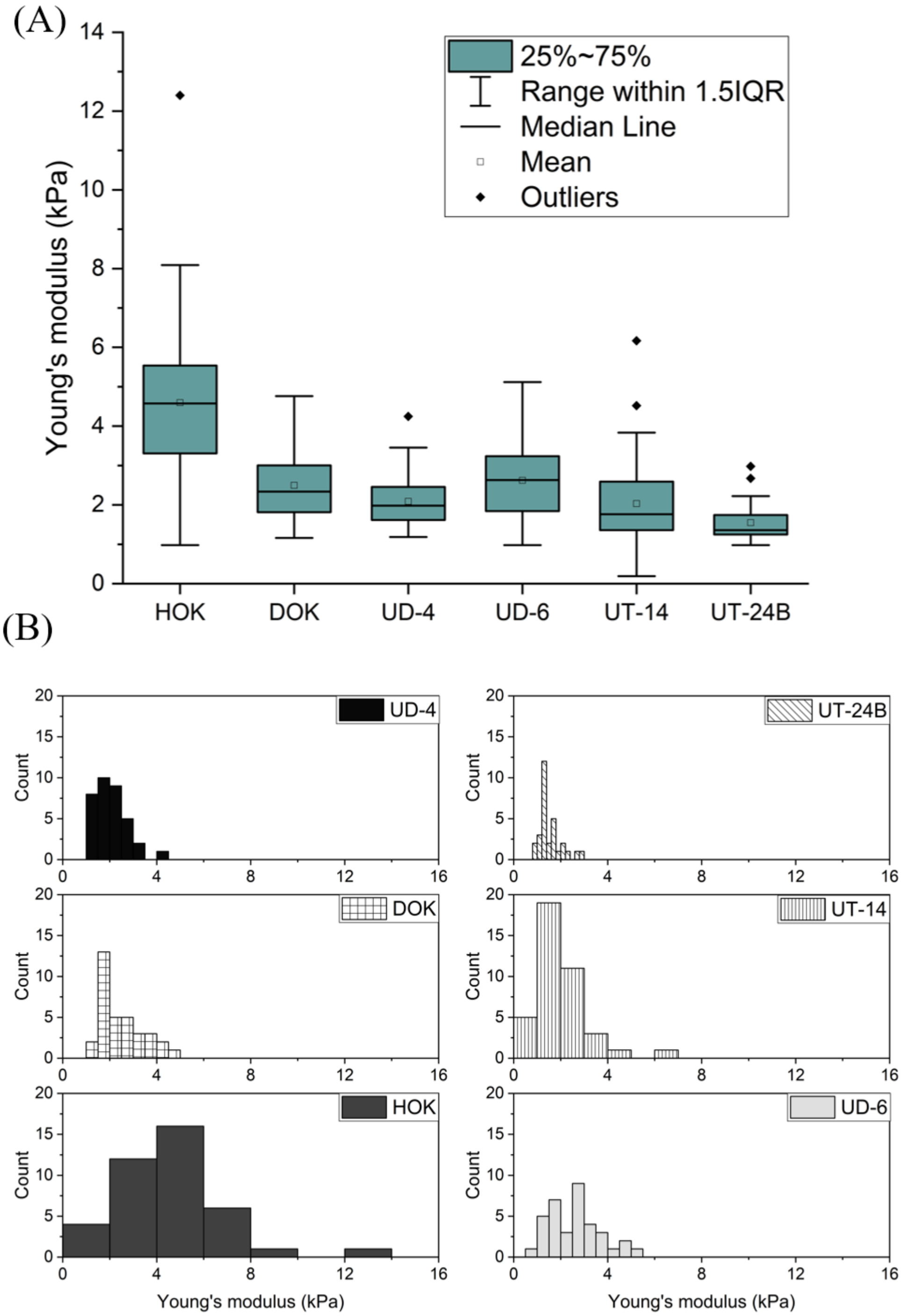

Figure 38: The boxplot and histogram of tongue cells' Young's modulus. (A) The median value of HOK cells' Young's modulus is greater than those of the pathological cells'. (B) The positive skewness can be found in HOK cells. The distribution of the healthy cells is broader.

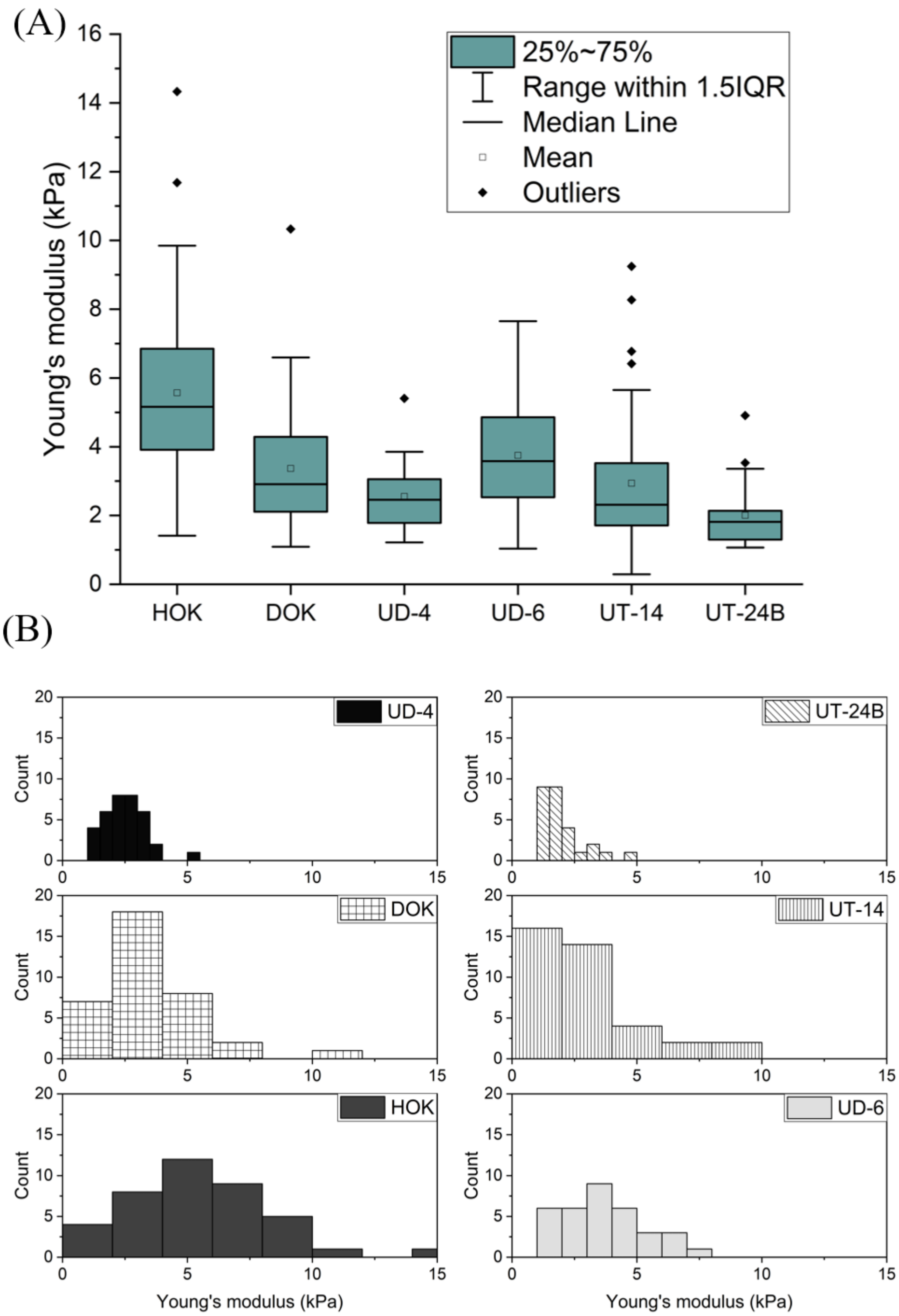

Figure 39: The boxplot and histogram of nuclear Young's modulus. (A) The median value of the HOK is the highest one, while the UT-24B exhibit the smallest median value. (B) The data distribution of the HOK is approximately symmetric, and a positively skewed distribution is observed in HOK cells.

The experimental results indicate that the cells lose connection to their neighbors and change their morphology from a cobblestone-like shape to an irregular shape, especially when oral cells are with higher cancer stages. The UT-SCC-24B cells emerge from a weaker cytoskeletal structure comprising of less well-defined filamentous structures and short segments. The topography of tongue cells is shown in Figure 40.

Metastatic UT-SCC-24B cells' periphery regions ((1.2 ± 0.3) kPa) are significantly softer than the healthy cells' (HOK: (3.6 ± 1.8) kPa), and metastatic UT-SCC-24B cells' periphery regions are also significantly softer than that of the dysplastic cells (DOK: (2.0 ± 1.8) kPa). The boxplot and histogram of Young's modulus in cells' peripheral regions of tongue cells are given in Figure 41.

The network of actin filaments, that are highly concentrated at the cytoplasm of the cells and associated actin-binding proteins, determines the cell shape and is involved in a variety of cell surface activities, including motility. The association of the actin cytoskeleton with the plasma membrane is thus central to the cell structure and the cell function. The reorganization of cell-cell junctions with an accompanying change in the structure of the actin cytoskeleton can be induced during oncogenesis.

Between the Young's modulus in peripheral regions of the tongue squamous carcinoma (TSCC) cells (UD-SCC-4: (2.1 ± 0.7) kPa; UD-SCC-6: (2.3 ± 1.0) kPa) and the Young's modulus in peripheral regions of the metastatic TSCC cells (UT-SCC-24B), a substantial difference is observed. No significant difference between the elastic values of UT-SCC-14 cells' peripheral regions ((1.3 ± 0.5) kPa) and the elastic values of UT-SCC-24B cells' peripheral regions is found. But the UT-SCC-14 cells' peripheral regions show a significant difference in the elastic moduli from the HOK cells', the DOK cells', the UD-SCC-4 cells', and the UD-SCC-6 cells'. The metastatic UT-SCC-24B tissue is collected from the cancer recurrence of the same patient. The results indicate that the TSCC cells (UT-SCC-14) with higher metastatic potential showed a decrease in the elastic moduli compared to TSCC cells (UD-SCC-4 and UD-SCC-6) with lower metastatic potential.

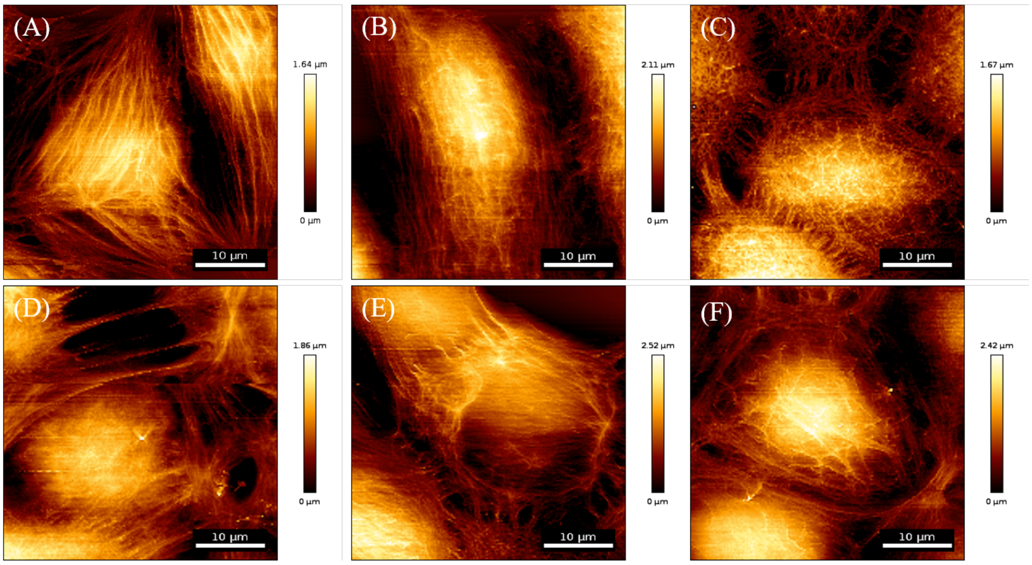

Figure 40: The topography of tongue cells. (A) HOK (B) DOK (C) UD-SCC-4 (D) UD-SCC-6 (E) UT-SCC-14 (F) UT-SCC-24B cells. Stress fiber organization of human tongue cells is more diffuse and weak with increasing disease states.

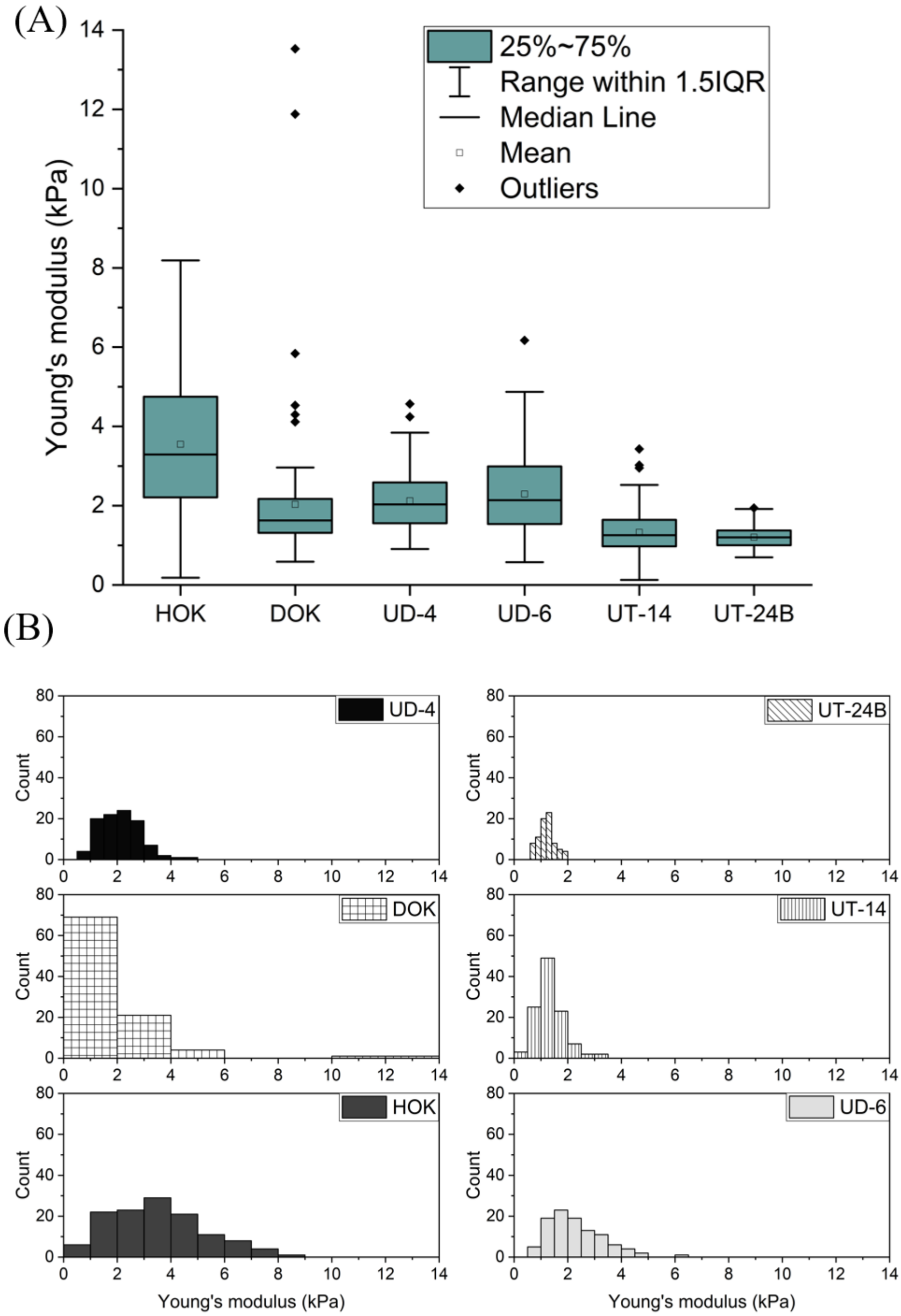

Figure 41: The boxplot and histogram of Young's modulus in cells' peripheral regions. (A) The UT-24B boxplot is condensed which presents more consistency, whereas the HOK boxplot shows the larger length of the boxplot. (B) The relative normal distribution is seen in the HOK, and the data distribution is broader is not seen in other oral cells.

The UT-SCC-24B cells exhibit significantly lower Young's modulus compared with the oral cells with various conditions of health (HOK), dysplasia (DOK), and carcinoma (UD-SCC-6). Dysplasia with the presence of abnormal cells is not usually classified as a malignant tumor, but they have great potential for preceding the development of cancer. The DOK cells referred to as mild to moderate are approximately 2-fold softer than the HOK cells but 1.67-fold stiffer than metastatic UT-SCC-24B cells. Our result is in agreement with those published studies on human cell lines, where cancer cells are characterized by enhanced deformability, which are exhibited in the reduction of the stiffness compared to their normal counterparts [66, 77, 78]. The malignant cells (breast cells and mesothelial cells) are softer than their counterparts by factors ranging from 2 to 4 [66, 78]. The variation in stiffness is due to the cytoskeletal instability from the onset of the tumor. The Young's modulus indicates that the deformation or compliance of individual cells is therefore important initiation of cancer, and the difference in elasticity is accompanied by alternations in cell structure.

The differences in elastic values of the healthy HOK and malignant oral cells are statistically significant. The disease cells, especially UT-SCC-24B cells appear more laterally mechanically homogeneous (less structured cytoskeleton led to a homogeneous body), whereas HOK cells presented more heterogeneous systems (cytosol and cytoskeleton are more structured than diseased cells) (Figure 40). Consistent with the previous study, which high malignant breast cancer cell line, MDA-MB-231 cells represented a good compromise in heterogeneity leading to a homogeneous cell body [79].

Biological functions and the pathophysiological state of living cells are closely related to local mechanical properties. It has been suggested that the mechanical properties of cells play a major role in oncogenic processes. The mechanical stability and integrity of biological cells are provided by the cytoskeleton. The reorganization of the network actin filament, which is known to contribute to cancer, has a strong association with the elastic modulus. The actin cytoskeleton may induce cell proliferation and activate oncogenes, resulting in tumorigenesis [80]. Increasing deformability and progression of the transformed phenotype from a non-tumorigenic oral cell line into a tumorigenic, metastatic cell line are closely related to the distinguishing remodel of the cytoskeleton [81]. Our findings indicate that the oral cells significantly alter the cellular elasticity as long as the progression of the abnormal development of cells (dysplasia) occurs. The AFM permits monitoring of biomechanical factors in diagnostic research for diseases offers great potential to find new diagnostic factors, particularly in the development of biomarkers to identify cancer cells and distinguish between differences involving normal tissues at an early stage of the disease.

4.3 Ultrasounds measurements of human oral healthy and cancer cells

The detailed mechanical properties of cells enable the potential treatment of diseased cells. Because the oral cells with different disease conditions have different degrees of cells' stiffness, the oral cells might have different cellular reactions to different resonant frequencies. The resonance frequency is mainly determined by the mechanical and morphological properties. The reflections of oral healthy and oral cancer cells from acoustic wave irradiation at different frequencies are observed under inverted microscopy (IX70). All US measurements were carried out together with students as a part of their bachelor or master theses [3].

4.3.1 The response of HOK cells to the ultrasonic waves

The healthy and cancerous cells (HOK and UD-SCC-1) were exposed to two different acoustic waves with exposure times 1, 3, and 5 minutes. The two different frequencies used were 24 kHz (150 mA) and 67 kHz (500 mA). The ultrasound probe was placed above the oral cells at different distances, a range of 0.5 mm to 0.05 mm. The oral cells (HOK and UD-SCC-1) were seeded at high density in order to present a tight confluent monolayer.

From cell images, the HOK cells responded to the resonance frequencies, neither at 24 kHz nor at 67 kHz. The HOK cellular morphology remained intact after exposure to the resonance frequency of 24kHz with exposure times 1, 3, and 5 minutes. The measurement results of HOK cells are shown in Figure 42.

No abnormal behavior was observed in HOK cells after exposure to the fre-

---

[3] Simon Sommerhage, Monika Illenseer

quency of 67 kHz. The two different ultrasonic waves' radiations did not induce a resonance catastrophe and do not destroy the HOK cells or change cells' behavior. HOK cell images before and after the acoustic waves irradiation are shown in Figure 43).

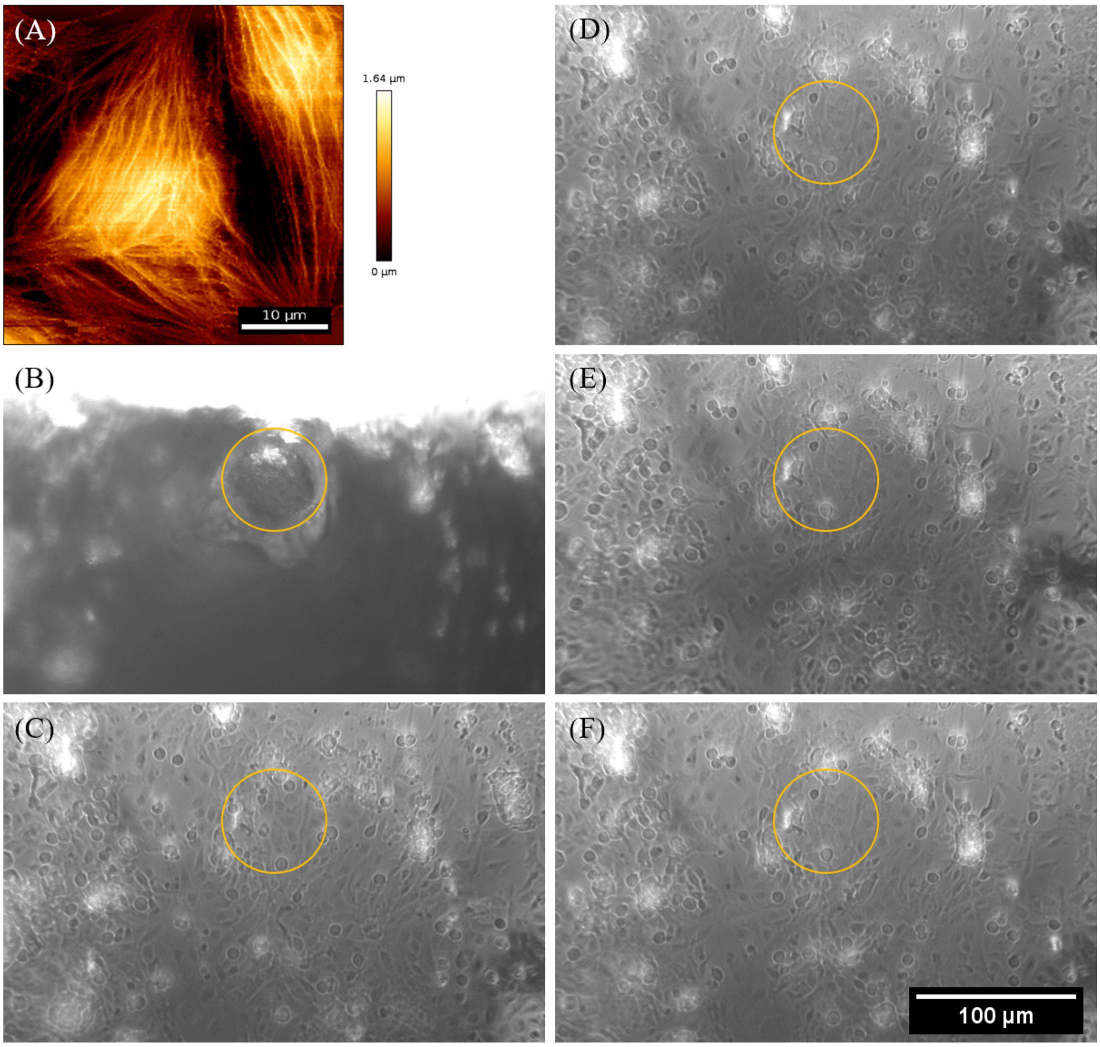

Figure 42: HOK cells were exposed under the frequency of 24 kHz. The sonotrode was placed over the cell at a distance of 0.05 mm. (A) the AFM height image (B) the tip of sonotrode with the diameter of 65 μm (C) before irradiation (D) after 1 min irradiation (E) after 3 mins irradiation (F) after5 mins irradiation. Under the exposure of 24 kHz, no cell death was observed.

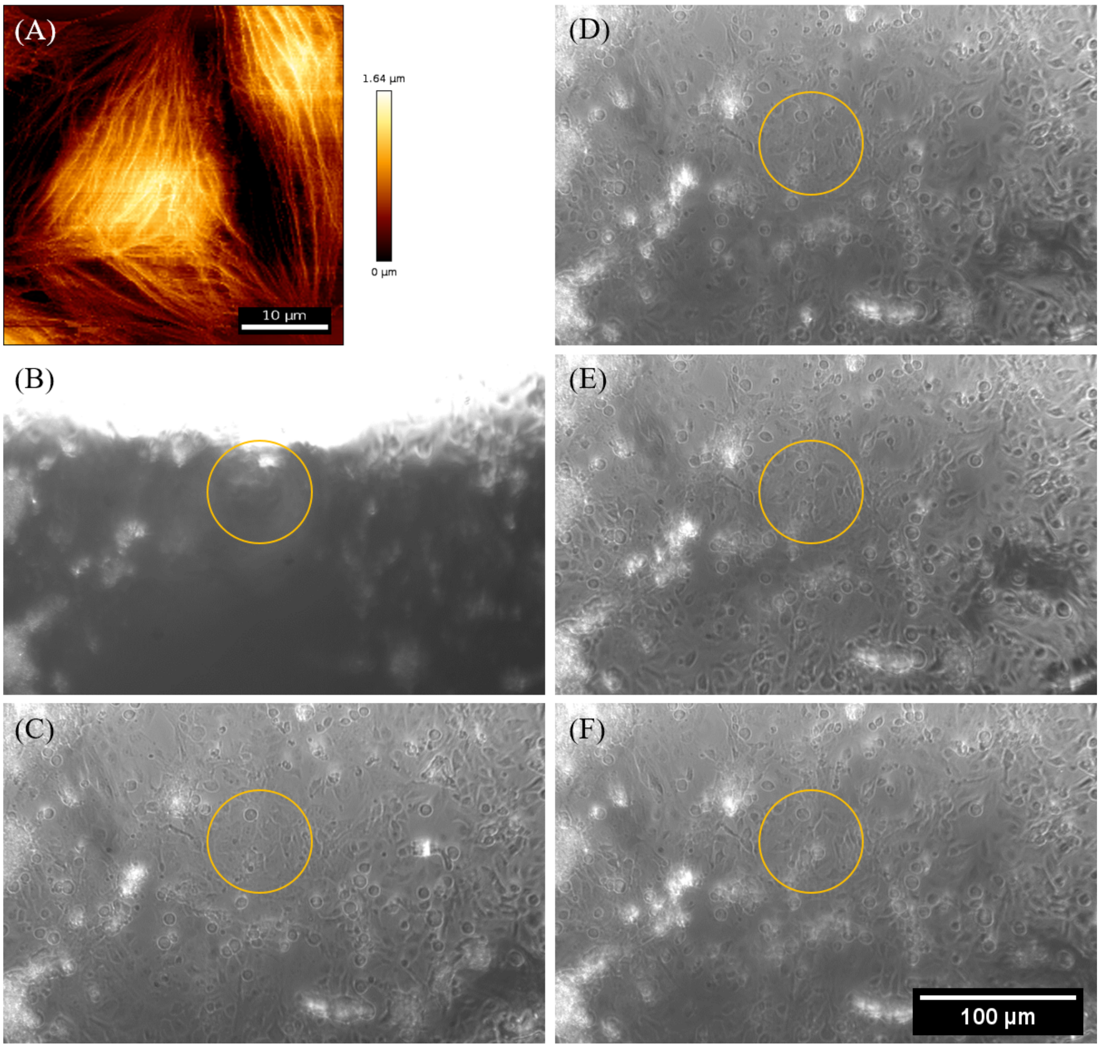

Figure 43: HOK cells were exposed under the frequency of 67 kHz. The sonotrode was placed over the cell at a distance of 0.05 mm. (A) the AFM height image (B) the tip of sonotrode with the diameter of 65 μm (C) before irradiation (D) after 1 min irradiation (E) after 3 mins irradiation (F) after 5 mins irradiation. Under the exposure of 67 kHz, no cell death or cell damage was observed.

4.3.2 The response of UD-SCC-1 cells to the ultrasonic waves

The reaction of UD-SCC-1 cells to the frequency of 24 kHz was observed. However, the oral cancerous cells only reacted to the acoustic wave as the probe was placed at a short distance of 0.05 mm over the cells. After a 3-min treatment with acoustic waves of 24 kHz frequency, cell death was observed in the US-SCC-1 cells.

Subsequently increasing expose time to 5 mins, the acoustic waves sufficiently disrupted more cancer cells as shown. UD-SCC-1 cell images before and after the acoustic waves irradiation are shown in Figure 44

Interestingly, the UD-SCC-1 cells first changed the cellular morphology in response to 67 kHz, 1 min, as shown in Figure 45(D). The cells in the highlighted area shrank and swelled. The round yellow circles mark the irradiation areas. The cell death took place with an increased exposure time of 67kHz to 3 mins, as shown in Figure 45. And more cell death was observed after 5-min exposed to the frequency (Figure 45(F)).

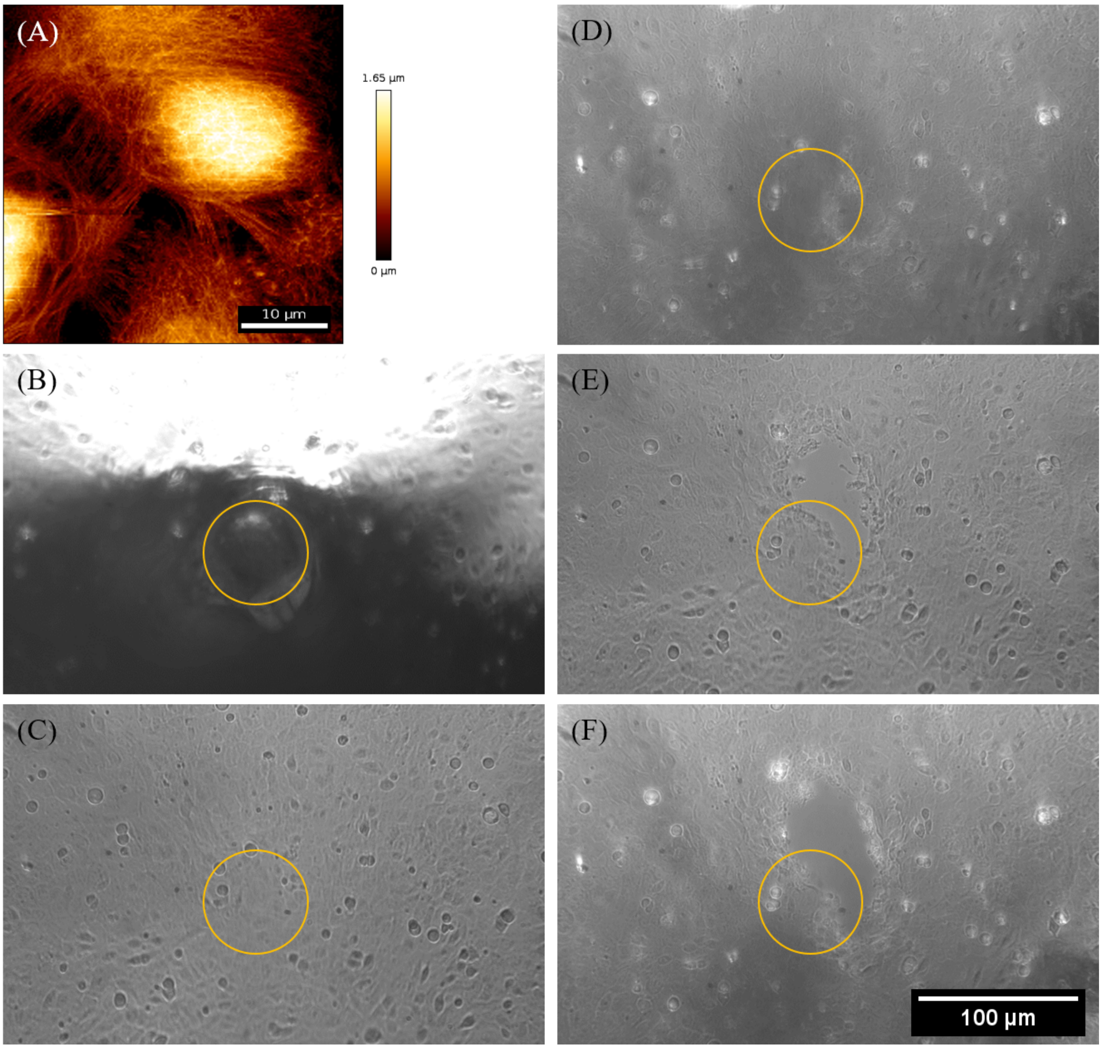

Figure 44: UD-SCC-1 cells were exposed under the frequency of 24 kHz. The sonotrode was placed over the cell at the distance of 0.05 mm. (A) the AFM height image (B) the tip of sonotrode with the diameter of 65 μm (C) before irradiation (D) after 1 min irradiation (E) after 3 mins irradiation (F) after 5 mins irradiation. Cells exposed to the frequency of 24 kHz, did indeed induce cell death.

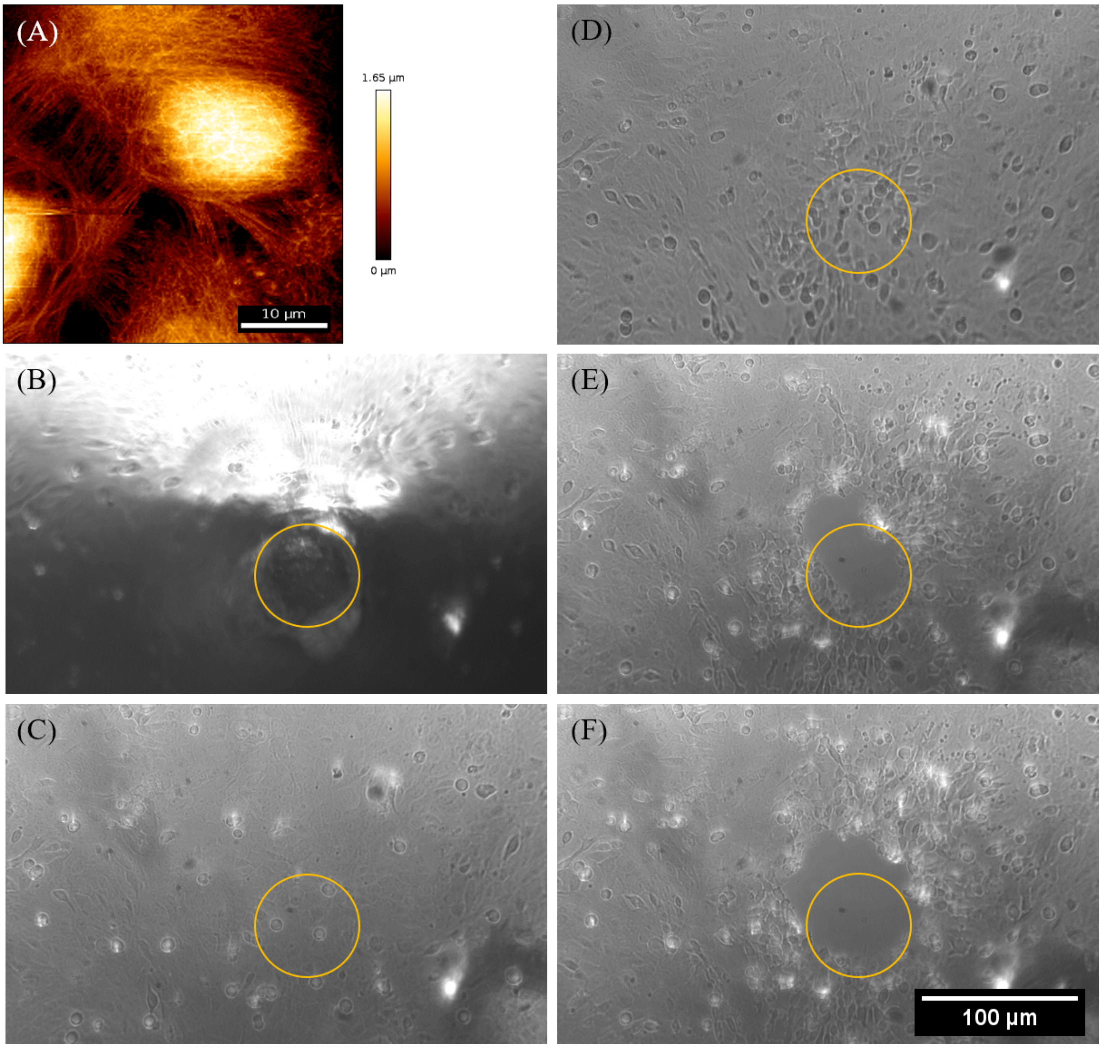

Figure 45: UD-SCC-1 cells were exposed under the frequency of 67 kHz. The sonotrode was placed over the cell at the distance of 0.05 mm. (A) the AFM height image (B) the tip of sonotrode with the diameter of 65 μm (C) before irradiation (D) after 1 min irradiation (E) after 3 mins irradiation (F) after 5 mins irradiation. The 67 kHz exposure on cells altered cell behaviors and further leading to cell death.

The resonance frequency is proportional to the Young's modulus, which is a measure of elasticity and is mainly determined by mechanical and morphological properties. The elastic properties of our oral cells were conducted utilizing the AFM showing a decrease in Young's modulus from healthy to cancerous cells. Owing to the divergence in mechanical properties and morphology [37], the natural frequencies at which local resonance occurs are expected to differ between healthy and cancerous cells. A normal mode analysis in the harmonic range [82] reveals the existence of a healthy-to-cancerous spectral gap in ground frequency of the order of 36.6 kHz. [83]. Besides, the growth rate of the resonance response of cancerous cells is faster than that of healthy cells, which is an important requirement for selectively targeting cancerous tissues.

The acoustic waves irradiation can induce a resonance catastrophe and destroy the cancerous cells while leaving healthy cells intact. Our results demonstrate that acoustic waves exhibiting low frequencies (of 24 kHz or 67 kHz) induced high amplitude oscillations in cancerous cells. The different reactions of cancerous and healthy cells enable the cell-selective treatment. Cell types' response to resulting mechanical stress depends on their biophysical properties. Our experimental system might fulfill the clinical demand for non-invasive tumor ablation, complementing the molecular targeting approach.

4.4 Human dermal cells

Mutations in the nuclear lamina can cause genome instability and subsequently disrupt nuclear architecture, chromatin organization, and gene expression [84]. These alterations are often associated with rapid telomere erosion and cellular aging. The HGPS is due to a mutation in the LMNA gene encoding lamin A and results in premature aging. However, the fundamental mechanism of rapid telomere erosion in HGPS patients remains elusive.

To analyze whether nuclear lamina abnormalities affect the cell mechanics, normal and HGPS fibroblasts were probed using an AFM to characterize the mechanical features. Subsequently, the cellular phenotype of progeria cells is improved by telomere elongation by means of retroviral hTERT infection with the catalytic subunit human telomerase, which successively elongates the shortened telomeres. Both normal and HGPS immortalized fibroblasts are further investigated utilizing AFM to indicate whether the modification changes the cellular mechanical properties after the immortalization.

4.4.1 Human normal and HGPS dermal cells

Force curve mapping where force curves are collected over an area is used to calculate the mechanical properties of cells. The stiffness of cells is determined from the force mapping that is required for calculation of the Young's modulus. Elastic measurements of normal and HGPS fibroblasts cultured uncoated Petri dishes were performed. AFM contact images were obtained in liquids using cantilevers with pyramidal tips.

The adherently grown human fibroblasts display a typical elongated fibroblast morphology (spindle-shaped or stellate-shaped). The HGP164 and the N20 are both in an elongated shape, however, they exhibit a wider cell body in comparison with other fibroblast cells. The N20 fibroblasts from the skin biopsy of a 50-year-old individual display the appearance of HGPS-like abnormal morphology. Nevertheless, the anomalous features are not as severe as those of progeria HGP164 fibroblasts. The observed dissimilarities in morphology might influence cell mechanical response result in different mechanical properties of fibroblasts. The topography of human fibroblasts is shown in Figure 46.

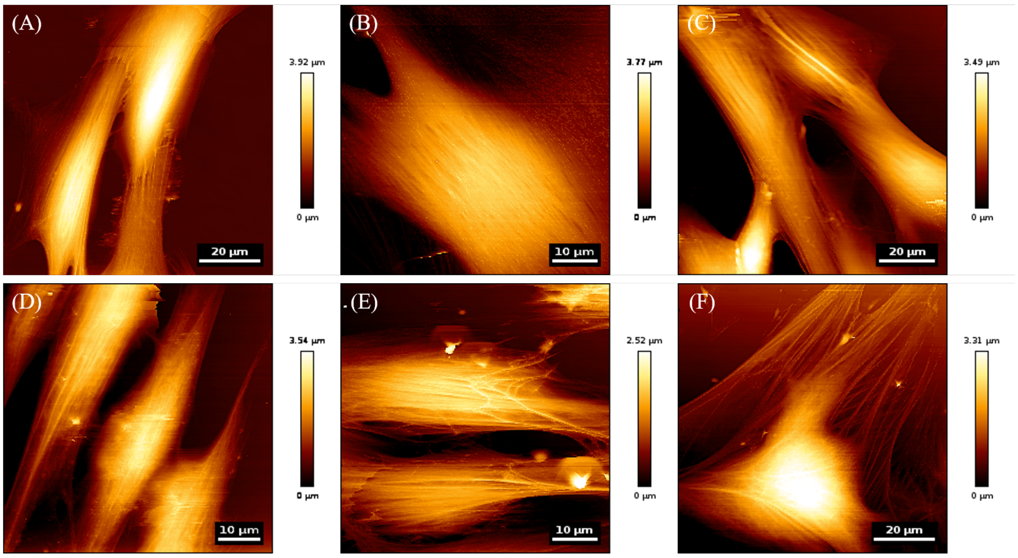

Figure 46: The topography of human fibroblasts established from skin biopsies of (A, B, and C) three patients with HGPS, (D) a young donor and (E and F) two old donors; A: HGP003, B: HGP164, C: HGP178, D: 811, E: N14, F: N20. The fibroblasts have an elongated cell shape. The HGP164 and the N20 cells appear an elongated, but wider shape compared to other fibroblasts.

The 811 fibroblasts ((5.3 ± 2.0) kPa) show no significant difference in Young's modulus as compared to the HGP164 cells ((6.2 ± 2.9) kPa). But, 811 cells are significantly softer than HGP003 cells ((11.3 ± 5.1) kPa) and than HGP178 cells ((10.3 ± 4.1) kPa). The N14 cells ((7.1 ± 3.0) kPa) are significantly softer than the HGP003 cells. The N14 cells show no substantial difference in the elastic values from the HGP164 cells nor the HGP178 cells. The N20 cells ((10.1 ± 7.1) kPa) present no statistically significant discrepancy in Young's modulus from HGP003 cells, as well as from HGP174 cells. Skin fibroblasts from a healthy donor, aged around 50, are significantly stiffer than the HGP164 cells. The boxplot and the histogram of fibroblasts' Young's modulus are given in Figure 47.

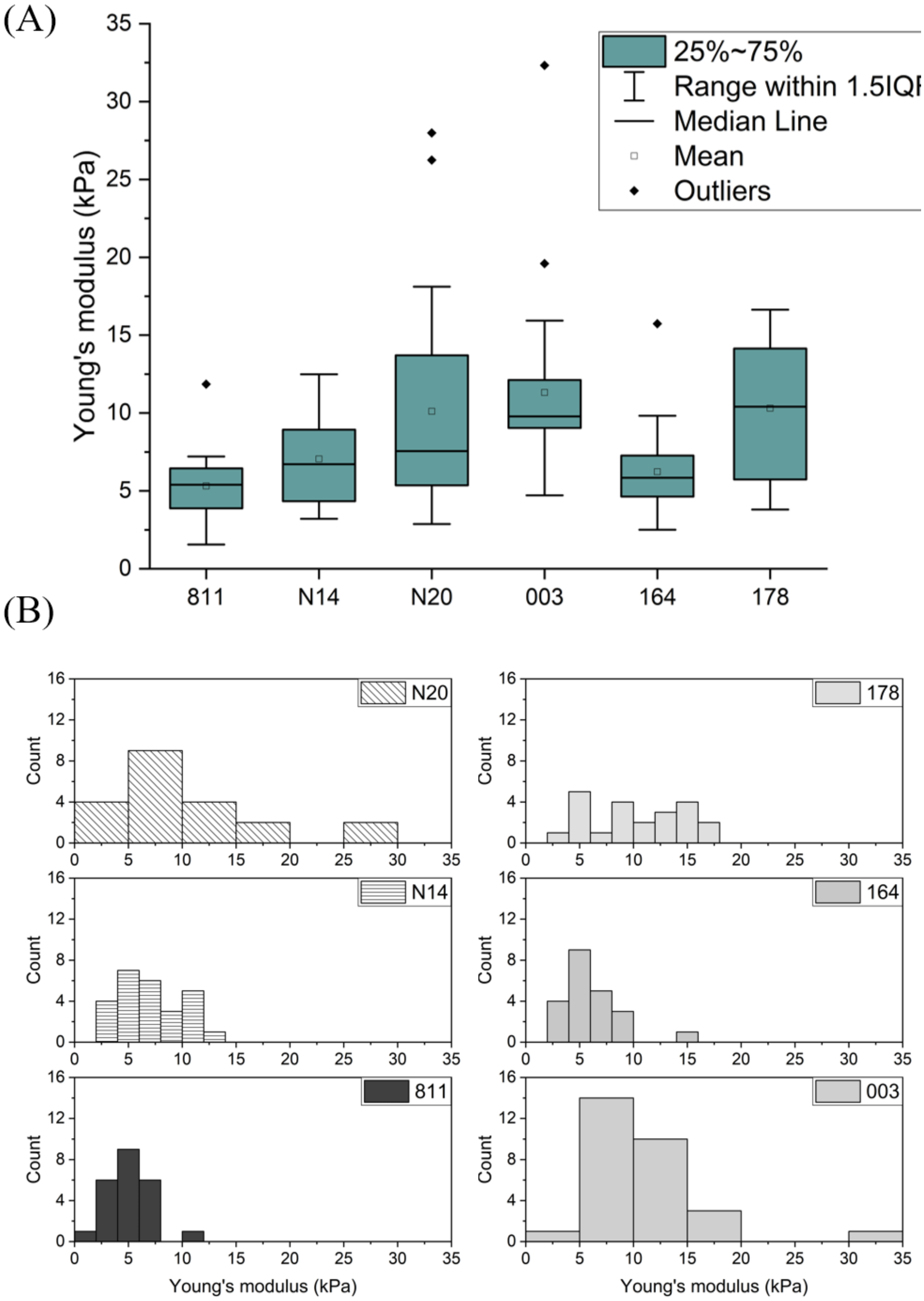

Figure 47: The boxplot and the histogram of fibroblasts' Young's modulus. (A) The median value of the groups of the healthy old donors is about 7, and about 9 for the groups of the patients. (B) The data of the fibroblasts from a young donor shows a narrow distribution as compared to the data of the fibroblasts from old donors and patients. The fibroblasts were derived from patients with HGPS (003, 164, and 178), a young donor (811), and two old donors (N14 and N20).

The HGP003 fibroblasts show no significant difference in Young's modulus comparing to the HGP178 cells. Surprisingly, the HGP164 cells have a substantial difference in elastic values comparing to the HGP003 cells, and the HGP164 cells are significantly softer than HGP178 cells. No remarkable difference in elastic values between N14 cells and 811 cells is observed. Between N20 cells and N14 cells, there is also no significant discrepancy in Young's modulus. N20 cells are distinctly stiffer than 811 cells.

The results indicate that a clear trend towards increasing elastic modulus with increasing age. Aged fibroblasts and HGPS fibroblasts are stiffer comparing to young fibroblasts. The distribution of the Young's modulus for the fibroblasts given in Figure 47(B) indicates that the data obtained from the young fibroblasts (from a young donor) has smaller variation than aged or HGPS fibroblasts.

A single gene mutation is responsible for progeria. The gene, known as lamin A (LMNA), makes a protein necessary for holding the center (nucleus) of a cell together. When this gene has a defect (mutation), an abnormal form of the lamin A protein called progerin is produced and makes cells unstable. This appears to lead to progeria's aging process. As shown in Figure 48, the nuclei of HGPS fibroblasts (HGP003, HGP164, and HGP178) are stiffer than of normal fibroblasts' (811). Not only HGPS fibroblasts but also fibroblasts from the old donors (N14 and N20) have stiffer nuclei than the 811 fibroblasts' nuclei. Data from nuclear elastic values of 811 fibroblasts demonstrates a left-skewed distribution with a single peak around 5 kPa. The data distribution (Figure 48) of old donors and HGPS patients' nuclear stiffness exhibit a broad range and a few of them show a bimodal distribution.

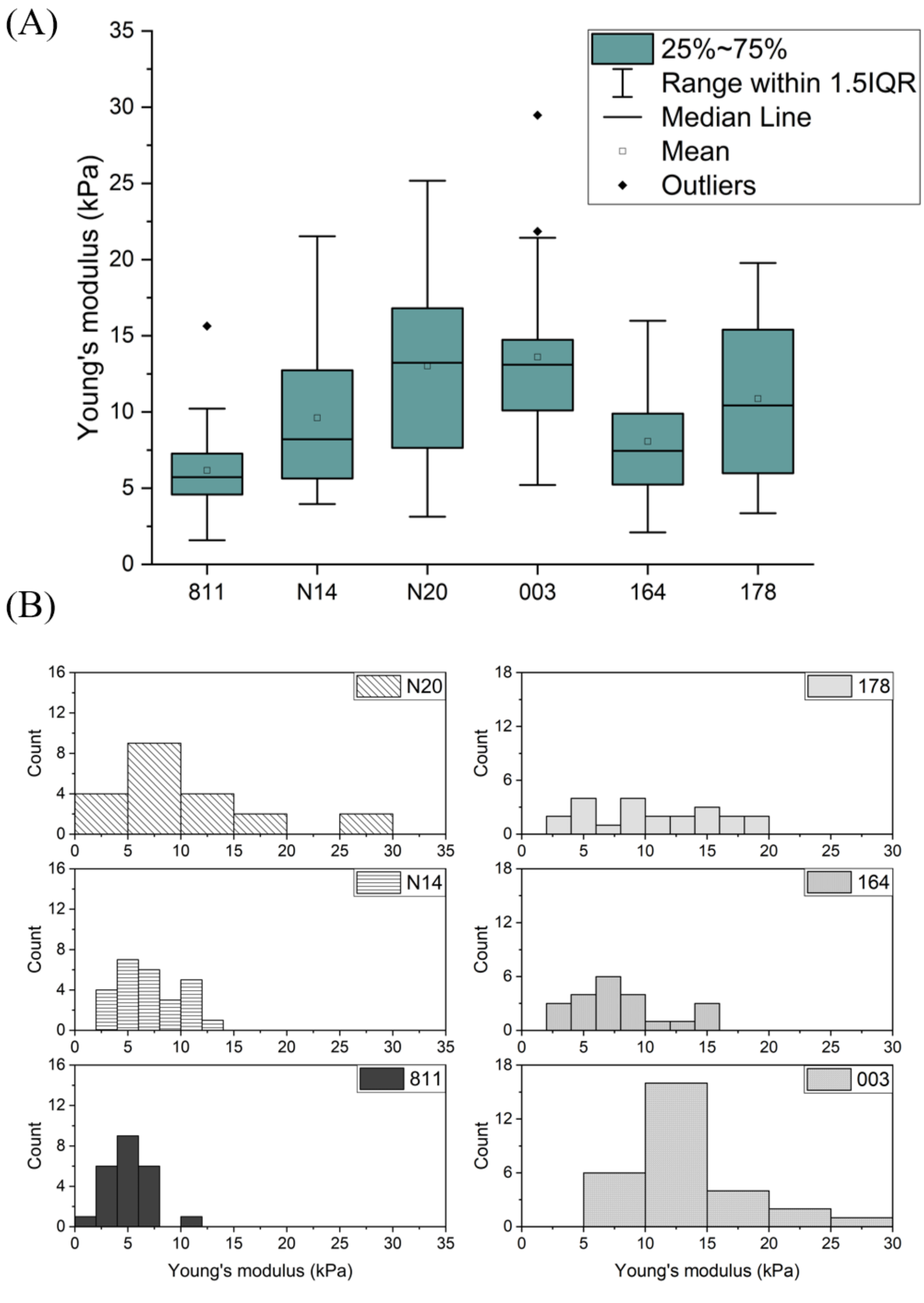

Figure 48: The boxplot and the histogram of fibroblast nuclear Young's modulus. (A) The median values of Young's modulus are not similar, and some groups are more variable than others. (B) The data distribution of 811 is narrow as compared to the others. The fibroblasts were derived from patients with HGPS (003, 164, and 178), a young donor (811), and two old donors (N14 and N20).

The presence of the altered protein makes the nuclear envelope unstable and progressively damages the nucleus. The nuclear abnormalities might also affect the mechanical properties of cells' peripheral regions. Hence, the stiffness of cells' peripheral regions was analyzed from the same set of force curves. Fibroblasts' peripheral regions are defined as the zone without the nuclei. In Figure 49, the average E values in periphery regions of both normal and HGPS fibroblasts are in the range of 5.5 kPa to 9.5 kPa. The average elastic moduli of aged and HGPS fibroblasts' peripheral regions are higher than that of the young fibroblasts'. The data distribution (Figure 49) of aged fibroblasts' elastic moduli in peripheral regions shows a broad distribution, where HGPS fibroblasts (HGP164 and HGP178) reveal a bimodal distribution. The elastic results (Figure 48 and Figure 49) obtained from fibroblasts reveal that the cells' peripheral regions are softer than nuclear regions.

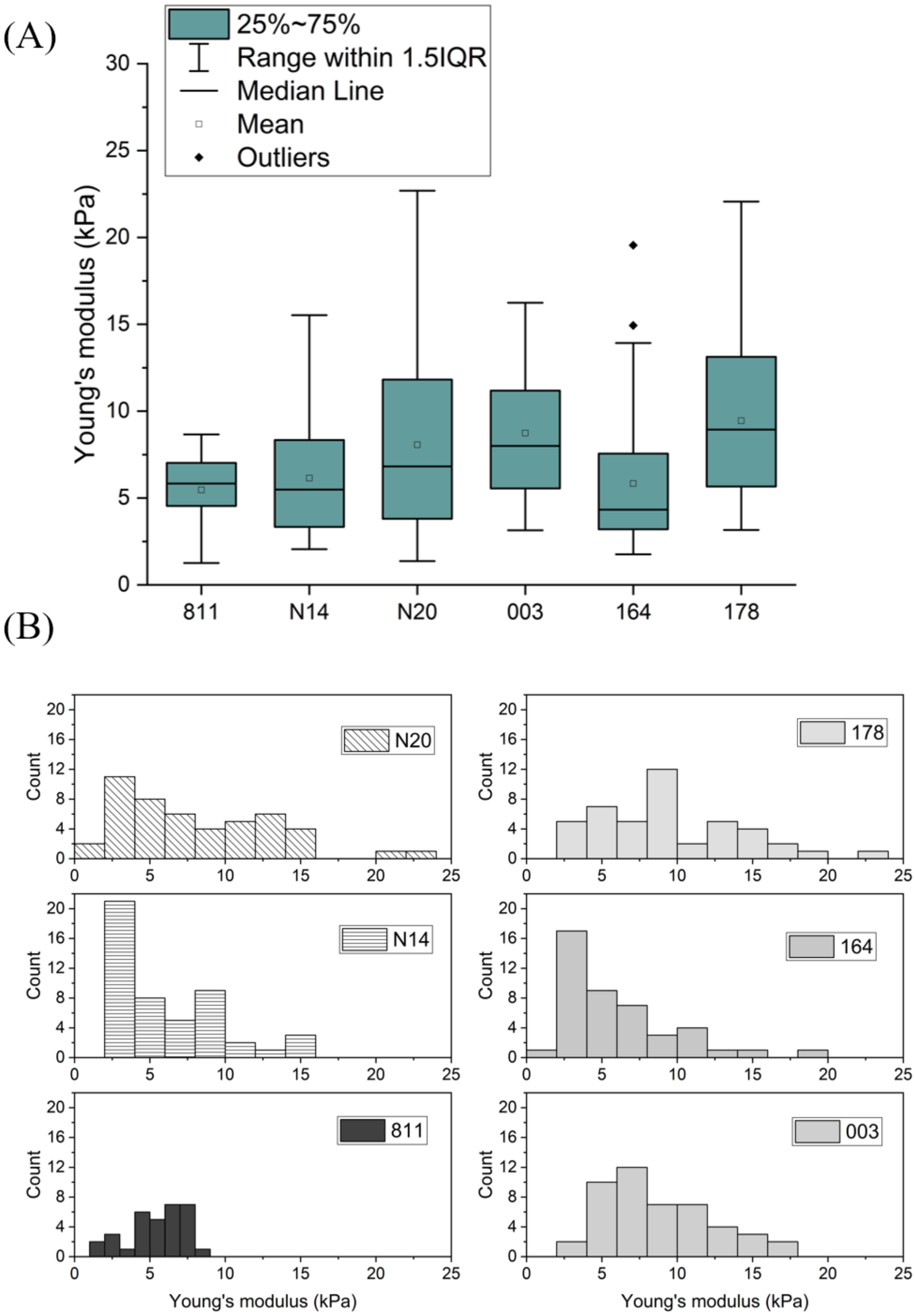

Figure 49: The boxplot and the histogram of Young's modulus in fibroblasts' periphery regions. (A) The median value of Young's modulus are not similar, and some groups are more variable than others. (B) The distribution of values for the 811 group is narrow as compared to the other groups. The fibroblasts were derived from patients with HGPS (003, 164, and 178), a young donor (811), and two old donors (N14 and N20).

The experimental system allows the comparison of fibroblasts from the healthy individuals with the patients' fibroblasts in presence of the mutant lamin A. We found that the higher cellular stiffness from the healthy donors is observed with increasing age. Fibroblasts from patients and old donors exhibit higher elastic moduli and broader data distribution than fibroblasts from the young donor, and some of these differences are statistically significant. The nuclei of fibroblasts from old donors (N14 and N20) and HGPS patients (HGP003, HGP164, and HGP178) reveal higher stiffness compared to nuclei from the young donor (811). The fibroblasts from the old donors (N14 and N20) indicate similar nuclear mechanical properties as the HGPS fibroblasts.

The cell nuclei from old individuals display HGPS-like defects, leading to multiple morphological anomalies of cell nuclei and disturbances in heterochromatin organization mitosis, DNA replication and repair, and gene transcription [84]. The mutations (progerin) in the nuclear lamin A cause the premature aging syndrome HGPS. Interestingly, progerin transcript also presents in cells of normal (healthy) individuals during normal aging [85]. Accumulation of progerin is observed with increasing age, indicating a role of progerin in natural cellular aging [86]. A suggestion is that progerin-dependent mechanisms act in natural aging, and the excessive activity of the same mechanisms may be the main cause of premature aging in HGPS [86].

Progerin accumulates in the nuclear envelope, disrupting nuclear architecture, chromatin organization, and gene expression. These alterations are often associated with rapid telomere erosion and cellular aging, making telomere size reduction one of the primary hallmarks of aging. The telomere length of individual chromosomes is variable; none of them have predictable shorter or predictable longer telomeres. A report showed that telomere shortens with each cell division and telomere erosion is seen in all human tissues [87]. Another study showed that during normal human aging, alterations of the nuclear lamina and generation of a mutant prelamin A protein called progerin have been detected [85, 88]. Progerin expression in normal human fibroblasts accelerates the loss of telomeres. Telomere length (TL) shortening is associated with age [89]. However, the fundamental mechanism of rapid telomere erosion in HGPS patients remains elusive.

4.4.2 Introduction of hTERT into human normal and HGPS dermal cells

Some studies have shown that the transient transfection of human telomerase (TERT) extended HGPS cellular lifespan and rescues proliferative defects associated with progerin [90, 91]. By means of retroviral hTERT infection with the catalytic subunit human telomerase might partially restore telomere length and reverse some of the senescent phenotypes of patient cells and may represent a therapeutic avenue for HGPS. The effect of the retroviral hTERT infection with the catalytic subunit human telomerase on the biomechanics of fibroblasts is investigated by AFM. AFM represents a powerful tool to relate mechanical changes to cellular function and structure. All immortalized cell lines were compared with the uninfected cells to demonstrate the ability of infection with the catalytic subunit hTERT to reverse manifestations of cellular senescence.

The retroviral hTERT infection with the catalytic subunit human telomerase lengthened the telomeres. There is no significant increase in the average Young's modulus of the 811 fibroblasts after the hTERT treatment (811: (5.3 ± 2.0) kPa; 811-T: (6.3 ± 3.2) kPa). No remarkable difference in elastic values between the N14 fibroblasts and the N14-T fibroblasts is observed (N14: (7.1 ± 3.0) kPa; N14-T: (6.8 ± 3.6) kPa). But a significant difference in cell elasticity is found in the N20 fibroblasts after the immortalization (N20: (10.1 ± 7.1) kPa; N20-T: (5.5 ± 3.0) kPa). Table 6 shows the quantitative elastic moduli of human normal and HGPS fibroblasts.

The HGP003-T fibroblasts infected with vectors encoding the human telomerase catalytic subunit are stiffer ((12.4 ± 6.4) kPa) in comparison to telomerase-negative control HGP003 fibroblasts ((11.3 ± 5.1) kPa), but the difference is not statistically significant. The cell stiffness of the immortalized FN164-T fibroblasts is significantly higher ((12.4 ± 3.6) kPa) than that of the HGP164 fibroblasts ((6.2 ± 2.9) kPa). After the hTER treatment, the average elastic modulus value of the introduction hTERT in HGP178 fibroblasts decreases (HGP178: (10.3 ± 4.1) kPa; HGP178-T: (6.8 ± 2.5) kPa), but the decrease is not significant. The boxplot and the histogram of fibroblasts' Young's modulus are given in Figure 50.

Table 6: The Young's modulus of human dermal cells

Cell lines (on uncoated substrate)	Relative telomere length (T/S ratio)	Average Young's modulus of cells' nuclei (kPa)	Average Young's modulus of cells' bodies (kPa)	Average Young's modulus of cells' peripheral regions (kPa)
HGP003	≈1.75 (low PD)	13.6 ± 5.1 (n = 29)	11.3 ± 5.1 (n = 29)	8.7 ± 3.6 (n = 47)
HGP003-T	≈2.25 (low PD)	14.0 ± 6.0 (n = 21)	12.4 ± 6.4 (n = 21)	11.3 ± 5.3 (n = 41)
HGP164	≈0.625 (high PD)	8.1 ± 3.7 (n = 22)	6.2 ± 2.9 (n = 22)	5.8 ± 3.8 (n = 44)
FN164-T	≈1.4 (middle PD)	14.5 ± 4.6 (n = 27)	12.4 ± 3.6 (n = 27)	13.2 ± 4.2 (n = 50)
HGP178	≈1.625 (middle PD)	10.9 ± 5.1 (n = 22)	10.3 ± 4.1 (n = 22)	9.5 ± 4.6 (n = 44)
HGP178-T	≈3.375 (low PD)	7.9 ± 3.1 (n = 25)	6.8 ± 2.5 (n = 25)	7.3 ± 3.3 (n = 48)
811	≈0.53 (middle PD)	6.2 ± 2.9 (n = 23)	5.3 ± 2.0 (n = 23)	5.5 ± 1.9 (n = 32)
811-T	≈1.17 (middle PD)	7.6 ± 3.8 (n = 22)	6.3 ± 3.2 (n = 22)	6.9 ± 4.6 (n = 43)
N14	≈1.25 (middle PD)	9.6 ± 4.8 (n = 26)	7.1 ± 3.0 (n = 26)	6.1 ± 3.5 (n = 49)
N14-T	≈2.625 (middle PD)	9.2 ± 4.8 (n = 22)	6.8 ± 3.6 (n = 22)	6.0 ± 3.7 (n = 41)
N20	≈1.375 (middle PD)	13.0 ± 6.7 (n = 21)	10.1 ± 7.1 (n = 21)	8.1 ± 5.1 (n = 48)
N20-T	≈4.0 (middle PD)	6.5 ± 4.1 (n = 25)	5.3 ± 3.0 (n = 25)	5.2 ± 4.1 (n = 50)

Cell lines (on uncoated substrate)	Relative telomere length (T/S ratio)	Median Young's modulus of cells' nuclei (kPa)	Median Young's modulus of cells' bodies (kPa)	Median Young's modulus of cells' peripheral regions (kPa)
HGP003	≈1.75 (low PD)	13.1 ± 5.1 (n = 29)	9.8 ± 5.1 (n = 29)	8.0 ± 3.6 (n = 47)
HGP003-T	≈2.25 (low PD)	14.4 ± 6.0 (n = 21)	14.8 ± 6.4 (n = 21)	12.5 ± 5.3 (n = 41)
HGP164	≈0.625 (high PD)	7.5 ± 3.7 (n = 22)	5.8 ± 2.9 (n = 22)	4.3 ± 3.8 (n = 44)
FN164-T	≈1.4 (middle PD)	13.2 ± 4.6 (n = 27)	11.7 ± 3.6 (n = 27)	12.7 ± 4.2 (n = 50)
HGP178	≈1.625 (middle PD)	10.4 ± 5.1 (n = 22)	10.4 ± 4.1 (n = 22)	8.9 ± 4.6 (n = 44)
HGP178-T	≈3.375 (low PD)	7.6 ± 3.1 (n = 25)	6.8 ± 2.5 (n = 25)	7.2 ± 3.3 (n = 48)
811	≈0.53 (middle PD)	5.7 ± 2.9 (n = 23)	5.4 ± 2.0 (n = 23)	5.8 ± 1.9 (n = 32)
811-T	≈1.17 (middle PD)	7.1 ± 3.8 (n = 22)	5.5 ± 3.2 (n = 22)	5.9 ± 4.6 (n = 43)
N14	≈1.25 (middle PD)	8.2 ± 4.8 (n = 26)	6.7 ± 3.0 (n = 26)	5.5 ± 3.5 (n = 49)
N14-T	≈2.625 (middle PD)	8.5 ± 4.8 (n = 22)	6.6 ± 3.6 (n = 22)	5.0 ± 3.7 (n = 41)
N20	≈1.375 (middle PD)	13.2 ± 6.7 (n = 21)	7.6 ± 7.1 (n = 21)	6.8 ± 5.1 (n = 48)
N20-T	≈4.0 (middle PD)	5.5 ± 4.1 (n = 25)	4.9 ± 3.0 (n = 25)	4.2 ± 4.1 (n = 50)

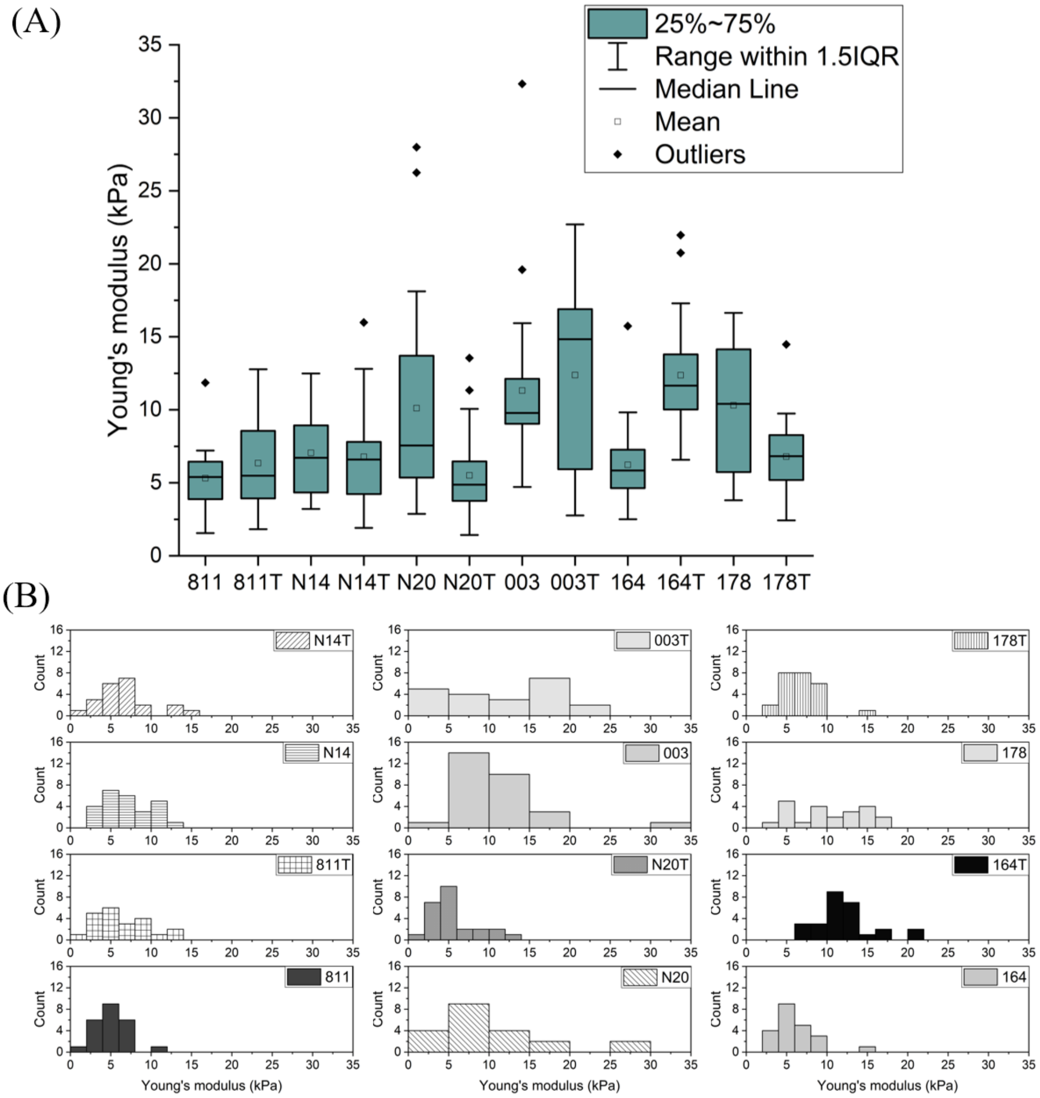

Figure 50: The boxplot and the histogram of fibroblasts' Young's modulus. (A) The median values of the groups of HGPS patients are generally higher than the other groups of healthy donors. The values in the data of some groups are spread out (N20, 003T, and 178). (B) The data distribution of the 811 group is narrow as compared to the other groups. The fibroblasts were derived from patients with HGPS (003, 164, and 178), a young donor (811), and two old donors (N14 and N20). After the immortalization of fibroblasts, the cells are additionally marked with T, such as 003T, 164T, and 178T for progeria fibroblasts and 811T, N14T, and N20T for normal fibroblasts.

The nuclear Young's modulus of the infected 811-T fibroblasts ((7.6 ± 3.8) kPa) does not show a significant difference in Young's modulus from the uninfected 811 fibroblasts ((6.2 ± 2.9) kPa). No considerable difference in the elastic moduli is found between the N14 nuclei ((9.6 ± 4.8) kPa) and the N14-T nuclei ((9.2 ± 4.8) kPa). Before the treatment of hTERT, the N20 fibroblasts' nuclei ((13.0 ± 6.7) kPa) are significantly stiffer than the nuclear stiffness of immortalized N20 fibroblasts' (N20-T: (6.5 ± 4.1) kPa). The stiffness of HGP003-T fibroblasts' nuclei ((14.0 ± 6.0) kPa) is not substantially different from the stiffness of HGP003 fibroblasts' nuclei ((13.6 ± 5.1) kPa). Between the HGP178 and HGP178-T fibroblasts, no significant difference in the nuclear elastic moduli is observed (HGP178: (10.9 ± 5.1) kPa; HGP178-T: (7.9 ± 3.1) kPa). But, there is a remarkable difference between the nuclear elasticity of HGP164 fibroblasts ((8.1 ± 3.7) kPa) and of FN164-T fibroblasts ((14.5 ± 4.6) kPa). The boxplot and the histogram of fibroblast nuclear Young's modulus are shown in Figure 51.

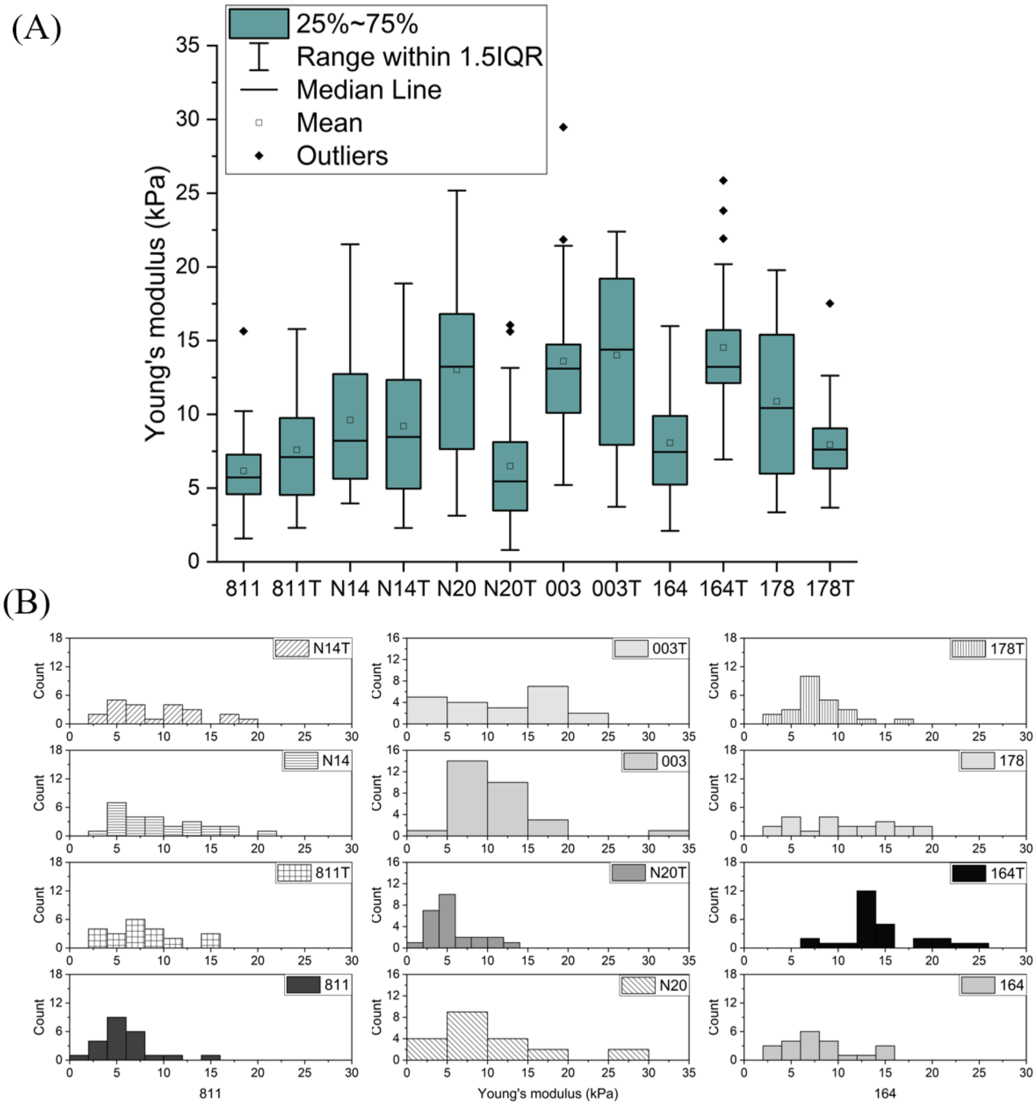

Figure 51: The boxplot and the histogram of fibroblast nuclear Young's modulus. (A) The median values of the groups of HGPS fibroblasts are generally higher than the other groups of normal fibroblasts. The values in some groups are spread out (N20, 003T, and 178). (B) The distribution of values for the 811 group is narrow as compared to the other groups. The fibroblasts were derived from patients with HGPS (003, 164, and 178), a young donor (811), and two old donors (N14 and N20). Progeria cells (003T, 164T, and 178T) and normal dermal cells (811T, N14T, and N20T) are infected with a retro virus.

The data distribution of E values in peripheral regions is given in Figure 52. A broad distribution for aged fibroblasts are observed, while the data for HGPS fibroblasts exhibit a bimodal distribution. After the infection of the catalytic subunit hTERT, the Young's modulus in peripheral regions of the HGPS fibroblasts indicates that there is no clear difference in Young's modulus between HGP003 and HGP003-T fibroblasts (HGP003: (8.7 ± 3.6) kPa; HGP003-T: (11.3 ± 5.3) kPa. The same trend in Young's modulus in peripheral regions can be seen in HGP178 fibroblasts: HGP178: (9.5 ± 4.6) kPa; HGP178-T: (7.3 ± 3.3) kPa). But the statistical analysis indicates that the elastic values of HGP164 fibroblasts' peripheral regions are significantly different from that of FN164-T fibroblasts' (HGP164: (5.8 ± 3.8) kPa; FN164-T: (13.2 ± 4.2) kPa). In cell peripheral regions, the stiffness of fibroblasts from healthy donors (811 and N14) do not dramatically change after the immortalization (811: (5.5 ± 1.9) kPa; 811-T: (6.9 ± 4.6) kPa; N14: (6.1 ± 3.5) kPa; N14-T: (6.0 ± 3.7) kPa). However, the cytoplasmic regions of uninfected N20 fibroblasts (N20: (8.1 ± 5.1) kPa) are stiffer than those of immortalized N20-T fibroblasts (N20-T: (5.2 ± 4.1) kPa).

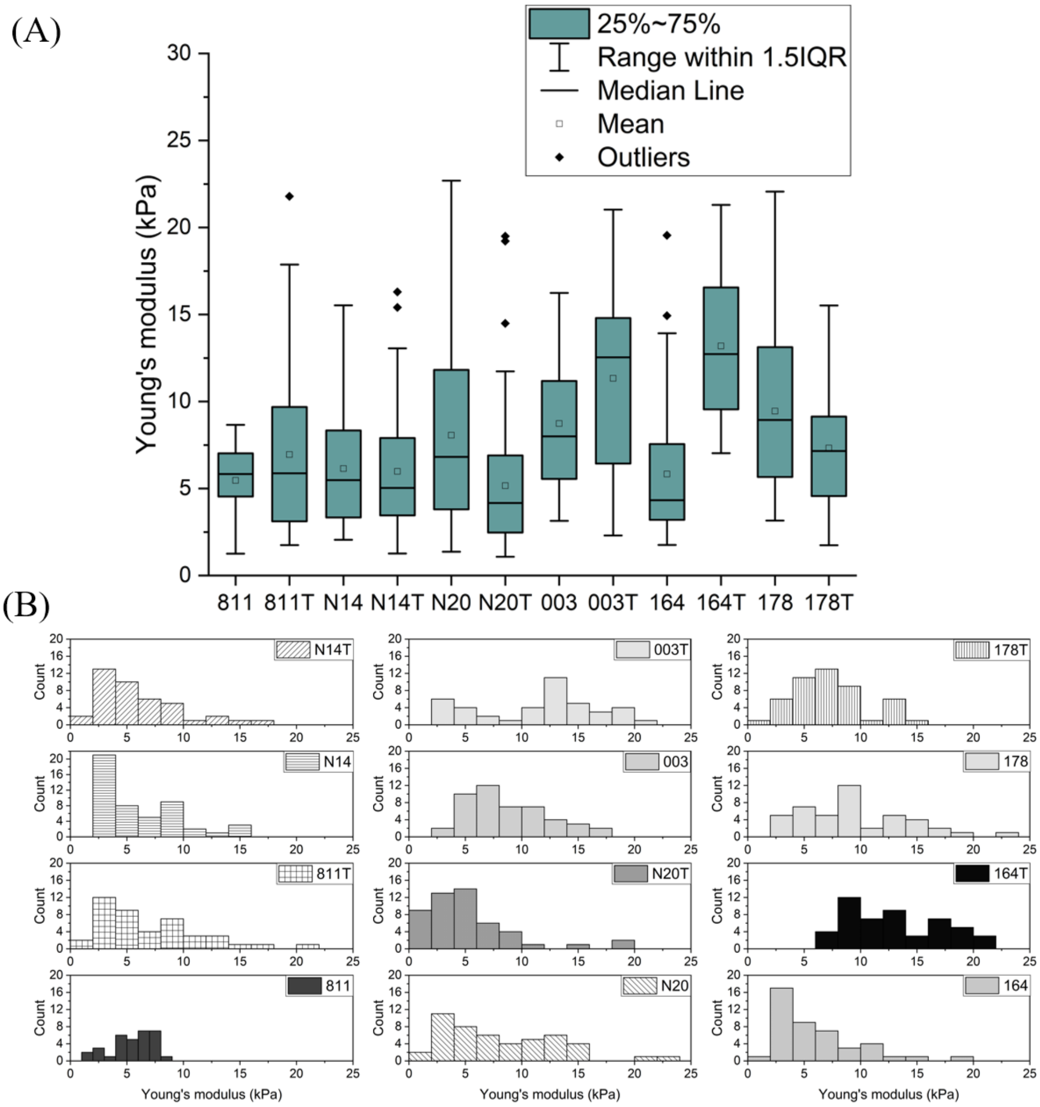

Figure 52: The boxplot and the histogram of Young's modulus in fibroblasts' peripheral regions. (A) The median value of Young's modulus of fibroblasts is not similar, some groups are more variable than others. (B) The data distribution of the 811 group is narrow as compared to the other groups. The fibroblasts were derived from patients with HGPS (003, 164, and 178), a young donor (811), and two old donors (N14 and N20). The telomere length of transfected cell lines 003T, 164T, 178T, 811T, N14T, and N20T) are longer after the retroviral hTERT infection with the catalytic subunit human telomerase.

The results indicate the retroviral hTERT infection with the catalytic subunit hTERT alters dermal fibroblasts' morphology, resulting in the differences in elastic values that can been seen not only in the cell nuclei but also in the cell bodies, as well as in cells' peripheral regions of fibroblasts. The two different cell lines, the HGP164 fibroblasts and the normal N20 fibroblasts exhibit a great difference in Young's modulus after the immortalization (Lamin A, a major component of the nuclear lamina, is responsible for nuclear stiffness, and B-type lamins for nuclear integrity [92]).

Except the fibroblast mechanical properties, we also investigated subcellular morphologies with the use of AFM. With nano-mechanical measurements, the cellular surface features are revealed and shown in Figure 53. The organization of the cytoskeleton in some fibroblasts has visually changed after the immortalization. Both HGP164 fibroblasts and N20 fibroblasts present the divergence in morphological features, after the immortalization. The FN164-T fibroblasts are elongated and spindle-shaped, whereas the HGP164 fibroblasts are flatter and in irregular cellular shape. The stress fibers in FN164-T fibroblasts are thick, while HGP164 fibroblasts contain thinner and fewer stress fibers. Not only HGP164 fibroblasts but also N20 fibroblasts appear as another morphology feature after hTERT treatment. The N20 fibroblasts' bodies are broader than N20-T fibroblasts'. The N20-T fibroblasts infected with the retro virus have visibly increased stress fibers (actin filament bundles) relative to control N20 fibroblasts. The formation of actin filaments in other fibroblasts might slightly be reorganized after the hTERT treatment, but the reorganization is not considerable. The reorganization of stress fibers in fibroblasts leads to differences in cell stiffness.

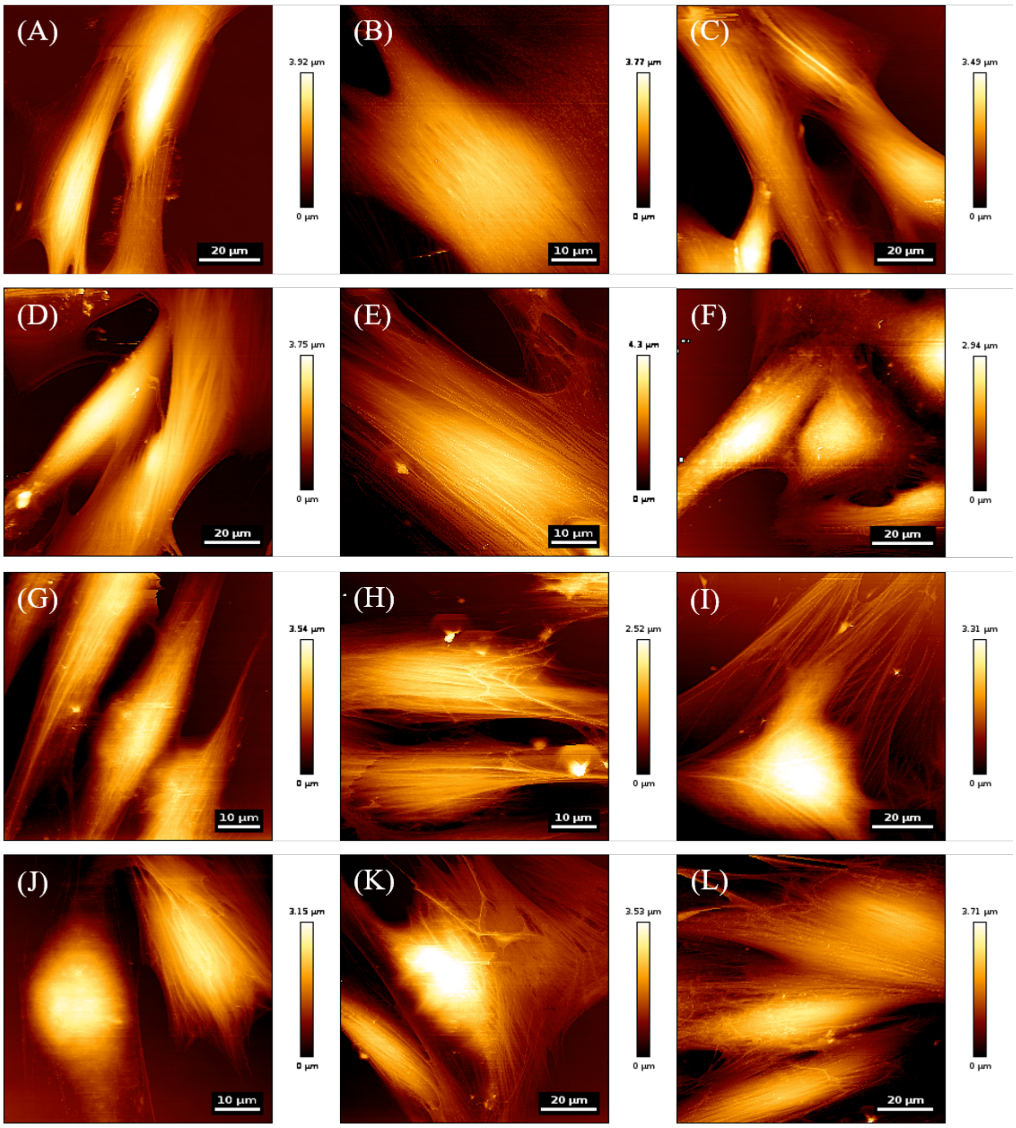

Figure 53: The topography of human dermal fibroblasts and hTERT-immortalized human dermal fibroblasts. (A, B, and C) HGPS fibroblasts, (D, E, and F) HGPS fibroblasts infected with the catalytic subunit hTERT, (G, H, and I) normal fibroblasts and (J, K, and L) normal fibroblasts infected with thecatalytic subunit hTERT; A: HGP003, B: HGP164, C: HGP178, D: HGP003-T, E: HGP164-T, F: HGP178-T, G: 811, H: N14, I: N20, J: 811-T, K: N14-T, L: N20-T.

The relative length of telomeres (T/S ratio) is estimated before to indicate if telomerase expression elongated or restored the length of telomeres of human fibroblasts [4]. Before the immortalization, the fibroblasts derived from two old individuals have short telomeres, (N14: 1.25 and N20: 1.375). The HGPS fibroblasts also have short telomeres (HGP003: 1.75, HGP164: 0.625, and HGP178: 1.625). The relative telomere length of the young donor (811) is surprisingly the shortest one with the number of 0.53. By the mean of retroviral hTERT infection with the catalytic subunit human telomerase, all the human dermal fibroblasts revealed a longer telomere length. In addition, the relative telomere length of the normal fibroblasts (811, N14, and N20) increased two times more than before the infection with the catalytic subunit. The relative telomere length of fibroblasts in detail is shown in Appendix J.1.

Previous reports indicated that the nuclear morphology of HGPS fibroblasts did improve nuclear morphology after the hTERT treatment [91]. Without the hTERT treatment, HGPS fibroblasts exhibited characteristic nuclear blebs and wrinkles [93]. Nuclear mechanics are tightly coupled to cytoskeletal mechanics via lamin A/C. The results suggest that the process of immortalization may indirectly alter the cytoskeleton contributing to differences in the mechanical properties. From the AFM images, HGP164 fibroblasts and N20 fibroblasts, both reveal an unorthodox fibroblast morphology, normally fibroblasts display an elongated morphology (spindle-shaped). The abnormal cell structure might due to the altered nuclear shape that progerin accumulation induced increasing nuclear envelope invaginations [25, 94]. The thick and bundled stress fibers can be observed in both transfected fibroblasts (the FN164-T and the N20-T). The distinguishable morphological alterations result in changing biomechanical responses. Still how the infection with the catalytic subunit hTERT affects cell mechanical properties remains ambiguous.

Our results indicate that the E value of some HGPS fibroblasts increased after the infection of hTERT, whereas other HGPS fibroblasts are softer or remain their mechanical properties after the hTERT treatment. The hTERT treatment does not have a significant effect on the biomechanical properties of normal fibroblasts, except the N20, at least no substantial difference in elasticity or cellular morphology is observed. The immortalized N20-T fibroblasts are significantly softer than the uninfected N20 fibroblasts. Both HGP178 fibroblasts and N20 fibrob-

---

[4] Anna Maria Haschke, Kathrin Jäger

lasts have a decrease in Young's modulus after the hTERT treatment. After the hTERT treatment, HGPS fibroblasts (HGP003 and HGP164) show an increase in Young's modulus. The results indicate that the hTERT treatment changes HGPS fibroblasts' mechanical properties indicating an increase or a decrease in Young's modulus. In HGPS cell lines characterized by short telomeres, the infection with the catalytic subunit hTERT increase telomere length, increase proliferative capacity and cellular lifespan and increase (or decrease) cell elasticity. The hTERT immortalization elicits genome reorganization not only in disease cells but also in the normal cells, such that whole chromosome territories normally located at the nuclear periphery in proliferating fibroblasts become mislocalized in the nuclear interior [95]. Through hTERT immortalization, the telomere length of HGPS cell lines increases [91], but may present other unexpected genomic instability.

The potential role of telomere elongation as a preventive or therapeutic intervention for several genetic and age-related diseases linking telomere shortening has been proposed [96, 97, 98]. Transient expression of purified human telomerase (hTERT) mRNA might partially restore telomere length and reverse some of the senescent phenotypes of HGPS fibroblasts[90, 91]. Our results show re-expression of telomerase did change the elasticity of human dermal fibroblasts, however, there are still numerous challenges ahead to understand the complex biological process.

Numerous aspects at the biochemical, cellular, and organismal level have suggested telomeres interact directly and indirectly with lamins and with lamin interacting proteins, via strictly telomeric proteins and telomere-associated factors [99]. The depletion of or mutations in LMNA can alter telomere distribution within the nucleus [100, 101]. Lamins also regulate multiple aspects of telomere function, including intranuclear diffusion, replication, elongation, heterochromatic organization, and processing by non-homologous end joining (NHEJ) upon dysfunction, processes that, in turn, are intertwined among them [99]. Altogether these observations imply an interplay between lamins and telomeres in different cellular processes, including epigenetics, telomere dynamics, telomere homeostasis, and DNA repair at dysfunctional telomeres, which, actually, in turn, are among them interconnected [99].

The connection between telomere and lamins may affect nuclear function by altering mechanotransduction or the activity of mechanosensitive genes through currently unknown mechanisms. The nuclear lamina is coupled to the cytoskeleton via connections mediated by the inner nuclear membrane (INM) and outer nuclear membrane (ONM) proteins, termed the linker of nucleoskeleton and cytoskeleton (LINC) complex [102]. The LINC complex spans the inner and outer nuclear membranes of the nuclear envelope and connects components of the cytoskeleton, providing a physical coupling between the nucleoskeleton and cytoskeleton that mediates the transfer of physical forces across the nuclear envelope [103]. In mammals, forces that move telomeres are generated in the cytoplasm by microtubule-associated motor proteins and transduced into the nucleus through the LINC complexes of the nuclear envelope [104]. Some studies showed that actin regulates chromatin dynamics under normal conditions in nonmigrating S-phase fibroblasts [105], whereas others reported with observations that microtubules play the dominant role in regulating chromatin dynamics regardless of the presence of DNA damage [106]. Regulation of telomere dynamics that is mediated by the intrinsic cytoskeletal fluctuations could play a major role in the maintenance of telomere integrity. Understanding telomere dynamics in the context of laminopathies, cytoskeleton-related diseases, and cancers may improve our knowledge of the pathophysiology of lamin-related diseases [107].

Cancer is also considered an age-related disease, as its risk increases with age. Several studies have investigated the relationship between telomere length and cancer risk or prognosis [108]. In normal cells, telomere shortening is associated with cellular senescence and is implicated in tumorigenesis and cancer [109]. Critically short telomeres activate the DNA damage response, which can lead to a growth arrest (cellular senescence) or apoptosis. The telomere attrition represents a (proliferative) barrier to tumor tumorigenesis, but also to aging phenotypes by limiting tissue regeneration [110]. However, the shortening of human telomeres has two opposing effects during cancer development. On the one hand, telomere loss may act as a tumor suppressor mechanism [111]. On the other hand, the human telomerase is reactivated in cancer indicating that telomerase is required for the proliferation of cells toward malignancy [112, 113]. Although much has been learned in recent years about the role of telomere in cancer development, many basic questions remain. Further research efforts are still needed to reveal the mechanisms underlying the complexity of the cancer genome.

5 Conclusion and outlook

Human oral cell

In this project oral cells with different disease stages are studied and used for the experiments. The influences of the different cultivation substrates are investigated by AFM. Substrates with different stiffness have a strong influence on both cell morphology and elasticity, especially on cells' peripheral regions. In other words, cell substructure and elasticity are cultivation substrate-dependent. Except for cultivation substrate, cell origins and sizes impinge on AFM assessment. The cancerous cells (UD-SCC-2) from the hypopharynx exhibit the smallest diameter, and the small cell body consequently results in the lowest cellular stiffness comparing to other cancerous cells from different origins, such as the tongue or tonsil (UD-SCC-1, UD-SCC-4, UD-SCC-6, and UD-SCC-14).

AFM scanning in liquid allows real-time observations of living cells and reveals the high resolution of the surface filaments of the cytoskeleton. The cytoskeleton of diseased cells is visually reorganized, and the change is more perspicuous accompanied by severe disease conditions. Cells with cancer alter not only the organization of the cytoskeleton but also the stiffness of cell bodies. The healthy cells (HOK) are with a significantly higher elasticity as compared to the cancerous cells (UD-SCC-4, UD-SCC-6, and UT-SCC-14), and the metastatic cells (UD-SCC-24B) have the softest cell bodies.

Moreover, benign cells are in general considered healthy cells. However, by consideration of AFM measurement, the benign cells (DOK) present significantly different cell behaviors as healthy cells. Thus, DOK cells are considered cancerous cells in this study, they have a higher potential for cancer development.

Besides, the cancerous tongue cells (UT-SCC-14) with high metastatic potential also behave differently than other cancerous cells that cellular elasticity is lower than other cancerous tongue cells (UD-SCC-4, UD-SCC-6) with lower malignancy.

Owing to the inherent characteristics, oral cells can react differently to two different resonance frequencies. The resonance frequency is proportional to the Young's modulus, which is a measure of elasticity and is mainly determined by cellular mechanical and morphological properties. Irradiation of cancerous cells (UD-SCC-1) with both 24 kHz and 67 kHz, resonance frequencies induce cell death, whereas normal cells (HOK) remained intact.

Outlook

The goal of the project is to develop a cell-selective therapy for tumor ablation. This therapeutic method is based on mechanical resonances instead of cavitation that affects surrounding tissue. If cells are irradiated with acoustic waves which force the cells to oscillate with their resonance frequencies, a resonance catastrophe is initiated. The resonance frequency is mainly determined by the mechanical and morphological properties of cells. With knowledge of the mechanical and morphological properties of cells, we did successfully induced cell death in cancerous cells, while normal cells remained entire. However, how acoustic waves affect benign and metastatic cells remain obscure. Moreover, co-cultivation of normal and pathological cells should be tested as well to simulate the human tissue that is normally surrounding by both normal and cancer cells that exist simultaneously.

Human dermal cells (fibroblasts)

The project begins with observations on biomechanical properties and surface characterization of fibroblasts with a mutation in the LMNA gene, and fibroblasts without genetic disorders. A mutation in the LMNA gene has been found in most patients with HGPS that causes the dramatic appearance of aging beginning in childhood. The characterization of biomechanics is investigated by AFM. The AFM assessment indicates that normal fibroblasts from old donors have some similarities to fibroblasts from patientswith HGPS. The cell elasticity of N20 fibroblasts shows comparable results from HGPS fibroblasts (HGP003, and HGP178). Not only elasticity, but the AFM images present that the N20 fibroblasts have a wider shape which is also perceived in HGPS fibroblasts (HGP164). In addition, the normal fibroblasts from a young donor (811) have softer cell bodies and softer nuclei than that of both old donors (N14 and N20) and patients with HGPS (HGP003, HGP164, and HGP178). Our results indicate that normal fibroblasts become stiffer with aging, and aged fibroblasts behavior HGPS fibroblasts alike.

Progeria syndrome is associated with accelerated telomere erosion. By means of retroviral hTERT infection with the catalytic subunit human telomerase can restore telomere length of HGPS fibroblasts without transforming fibroblasts. Transfection is a technique that delivers nucleic acids to specific subcellular cells. The method is recently suggested as a potential treatment for Progeria to prevent cell cycle arrest and senescence. The results from AFM measurements present a decrease or an increase in cell elasticity after the hTERT treatment. After hTERT treatment, the cytoskeleton filaments became thicker in HGPS fibroblasts, whereas no obvious cytoskeleton alternations in normal fibroblasts are noticed. However, how the retroviral hTERT infection with the catalytic subunit human telomerase affect in the biomechanics of fibroblasts remains elusive. The impact of the hTERT treatment on the cellular mechanics and on cytoskeleton structures is observed using AFM, but the hTERT treatment might at the same time affects the stability of the chromosome in the cell nucleus; as a result, different cellular processes are disturbed.

Outlook

The object of the project is to investigate the biomechanics and cytoskeleton of HGPS fibroblasts and their normal counterpart and seek a possible treatment for the rare disease. From the AFM results, HGPS fibroblasts have different cell mechanics and different surface characterization after the hTERT treatment. Still because of the patient diversity more samples have to be examined using AFM. More measurement techniques can be utilized in order to understand the mechanisms behind, such as cell staining, PCR, etc. It is also interesting to examine the effect of transfection not only on fibroblasts but also on cardiac cells or muscle cells. After all, patients with HGPS suffer from aging-associated symptoms including lack of subcutaneous fat, hair loss, joint contractures, and a cardiovascular disease resembling atherosclerosis.

A Appendix

A.1 Approximate amount of cells seeded in a Petri dish

Table A.1: Approximate amount of cells seeded in a Petri dish three days before measurements

Cell lines	Amount of cells	Comment
UD-SCC-1	300 - 400 μml of 9 ml	
UD-SCC-2	300 - 400 μml of 9 ml	
UD-SCC-4	200 - 300 μml of 9 ml	strain through 40 μm cell strainer
UD-SCC-6	300 - 500 μml of 9 ml	strain through 40 μm cell strainer
UT-SCC-14	200 - 400 μml of 9 ml	strain through 40 μm cell strainer
UT-SCC-24B	200 - 400 μml of 9 ml	strain through 40 μm cell strainer
DOK	200 - 400 μml of 9 ml	
HOK	100 - 200 μml of 4 ml	
HGP003	100 - 200 μml of 2 ml	
HGP003-T	100 - 200 μml of 3 ml	
HGP164 (FN164)	300 μml of 2 ml	low growth rate
HGP164-T (FN164-T)	100 μml of 3 ml	
HGP178	100 - 200 μml of 3 ml	
HGP178-T	100 - 200 μml of 3 ml	
811	200 - 300 μml of 3 ml	
811-T	400 - 500 μml of 4 ml	
N14	100 - 200 μml of 2 ml	
N14-T	200 - 300 μml of 3 ml	
N18	-	
N18-T	100 μml of 3 ml	strain through 40 μm cell strainer
N20	300 μml of 2 ml	low growth rate
N20-T	200 - 300 μml of 3 ml	

B Appendix

B.1 The calibration curve of the ultrasound probe

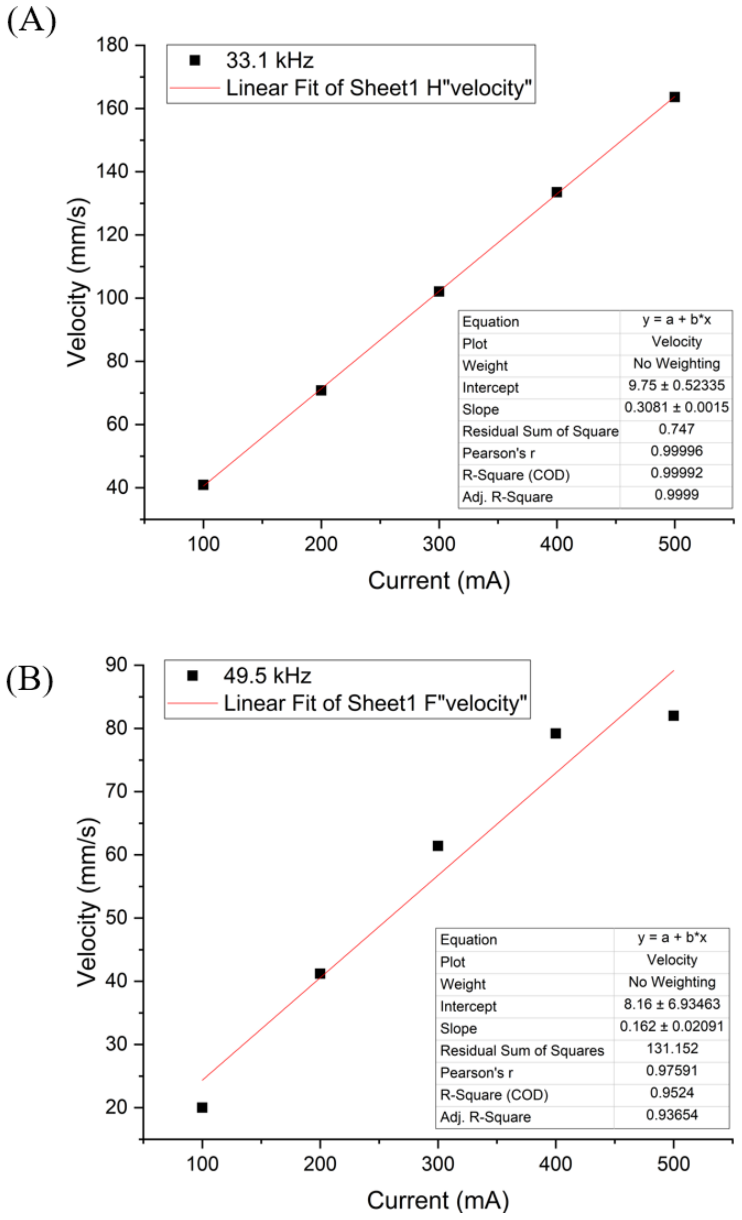

Figure B.1: Vibration velocity- target current characteristics of the two resonances according to the measurements using laser Doppler vibrometer: (A) at the resonance frequency of 33.1 kHz (B) at the resonance frequency of 49.5 kHz

C Appendix

C.1 The average Young's modulus of human oral cells

Table C.1: The average Young's modulus of human oral cells with different cancer stages

Cell lines	Sample Origin	Young's modulus of cells' nuclei (kPa)	Young's modulus of cells' bodies (kPa)	Young's modulus of cells' peripheral regions (kPa)
UD-SCC-1 (on uncoated substrate)	Oropharynx (Tonsil)	3.8 ± 2.3 (n = 35)	3.4 ± 2.5 (n = 35)	3.3 ± 1.7 (n = 109)
UD-SCC-1 (on gelatin-coated substrate)	Oropharynx (Tonsil)	3.1 ± 1.6 (n = 45)	2.6 ± 1.1 (n = 45)	2.4 ± 0.8 (n = 124)
Cell lines	Sample Origin	Young's modulus of cells' nuclei (kPa)	Young's modulus of cells' bodies (kPa)	Young's modulus of cells' peripheral regions (kPa)
UD-SCC-1	Oropharynx (Tonsil)	3.1 ± 1.6 (n = 45)	2.6 ± 1.1 (n = 45)	2.4 ± 0.8 (n = 124)
UD-SCC-2	Hypopharynx	2.5 ± 1.6 (n = 41)	1.9 ± 0.9 (n = 44)	1.4 ± 0.6 (n = 116)
UD-SCC-4	Oropharynx (Tongue)	2.6 ± 0.9 (n = 35)	2.1 ± 0.7 (n = 35)	2.1 ± 0.7 (n = 100)
UD-SCC-6	Oral cavity (Tongue)	3.7 ± 1.7 (n = 34)	2.6 ± 1.1 (n = 36)	2.3 ± 1.0 (n = 103)
UT-SCC-14	Oral cavity (Tongue)	2.9 ± 2.0 (n = 38)	2.0 ± 1.1 (n = 40)	1.3 ± 0.5 (n = 111)
UT-SCC-24B	Oral cavity (Tongue)	2.0 ± 0.9 (n = 27)	1.5 ± 0.5 (n = 30)	1.2 ± 0.3 (n = 79)
DOK	Dorsal tongue	3.4 ± 1.8 (n = 36)	2.5 ± 0.9 (n = 34)	2.0 ± 1.8 (n = 96)
HOK	Oral mucosa	5.6 ± 2.7 (n = 40)	4.6 ± 2.2 (n = 40)	3.6 ± 1.8 (n = 125)

C.2 The median Young's modulus of human oral cells

Table C.2: The median Young's modulus of human oral cells with different cancer stages

Cell lines	Sample Origin	Young's modulus of cells' nuclei (kPa)	Young's modulus of cells' bodies (kPa)	Young's modulus of cells' peripheral regions (kPa)
UD-SCC-1 (on uncoated substrate)	Oropharynx (Tonsil)	2.8 ± 2.3 (n = 35)	2.6 ± 2.5 (n = 35)	2.9 ± 1.7 (n = 109)
UD-SCC-1 (on gelatin-coated substrate)	Oropharynx (Tonsil)	2.8 ± 1.6 (n = 45)	2.3 ± 1.1 (n = 45)	2.3 ± 0.8 (n = 124)

Cell lines	Sample Origin	Young's modulus of cells' nuclei (kPa)	Young's modulus of cells' bodies (kPa)	Young's modulus of cells' peripheral regions (kPa)
UD-SCC-1	Oropharynx (Tonsil)	2.8 ± 1.6 (n = 45)	2.3 ± 1.1 (n = 45)	2.3 ± 0.8 (n = 124)
UD-SCC-2	Hypopharynx	2.1 ± 1.6 (n = 41)	1.5 ± 0.9 (n = 44)	1.3 ± 0.6 (n = 116)
UD-SCC-4	Oropharynx (Tongue)	2.5 ± 0.9 (n = 35)	2.0 ± 0.7 (n = 35)	2.0 ± 0.7 (n = 100)
UD-SCC-6	Oral cavity (Tongue)	3.6 ± 1.7 (n = 34)	2.6 ± 1.1 (n = 36)	2.1 ± 1.0 (n = 103)
UT-SCC-14	Oral cavity (Tongue)	2.3 ± 2.0 (n = 38)	1.8 ± 1.1 (n = 40)	1.3 ± 0.5 (n = 111)
UT-SCC-24B	Oral cavity (Tongue)	1.8 ± 0.9 (n = 27)	1.4 ± 0.5 (n = 30)	1.2 ± 0.3 (n = 79)
DOK	Dorsal tongue	2.9 ± 1.8 (n = 36)	2.3 ± 0.9 (n = 34)	1.6 ± 1.8 (n = 96)
HOK	Oral mucosa	5.2 ± 2.7 (n = 40)	4.6 ± 2.2 (n = 40)	3.3 ± 1.8 (n = 125)

D Appendix

D.1 The Young's modulus images of human oral cells with different cancer stages

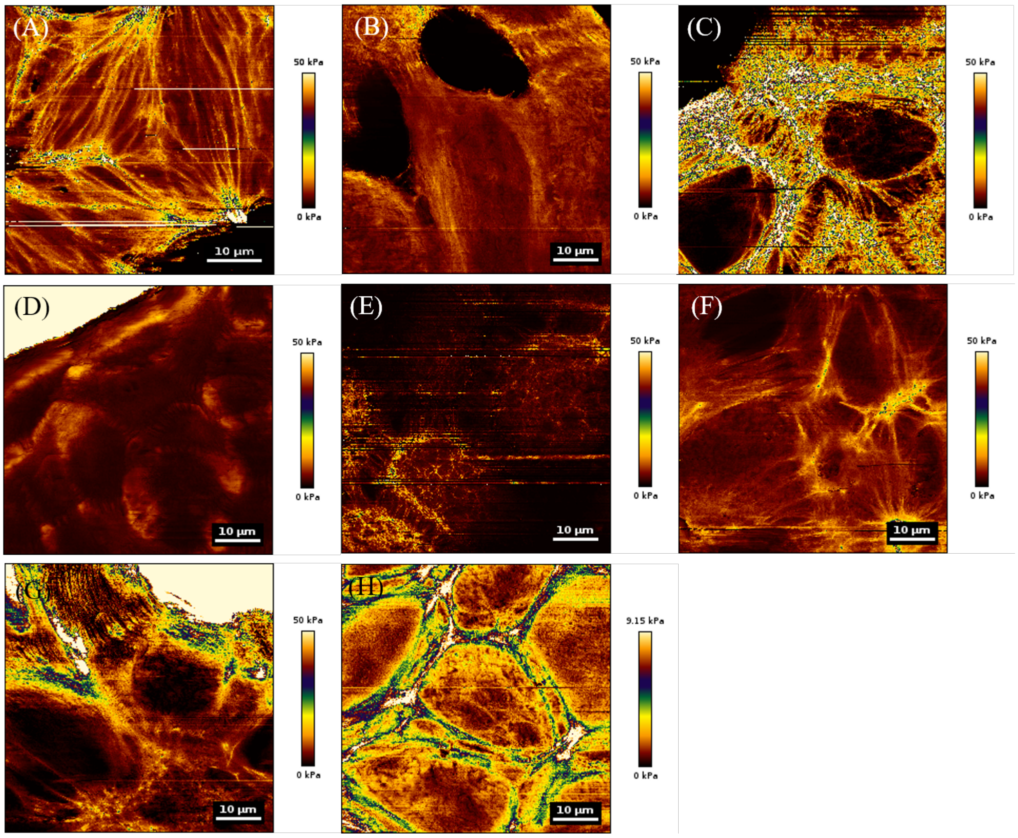

Figure D.1: The Young's modulus images of human oral cells. (A) HOK (B) DOK (C) UD-SCC-1 (D) UD-SCC-2 (E) UD-SCC-4 (F) UD-SCC-6 (G) UT-SCC-14 (H) UT-SCC-24B cells. The images are for visualizing information related to the stiffness. A flexible material has low Young's modulus and changes its shape considerably. By measuring the elastic properties of cancerous cells compared to normal cells, may help identify diseases detectable with elasticity imaging, and even may aid differential diagnosis based on quantitative elastic modulus data for different pathological processes.

E Appendix

E.1 The AFM height images of UD-SCC-1 cells cultured on the uncoated substrate

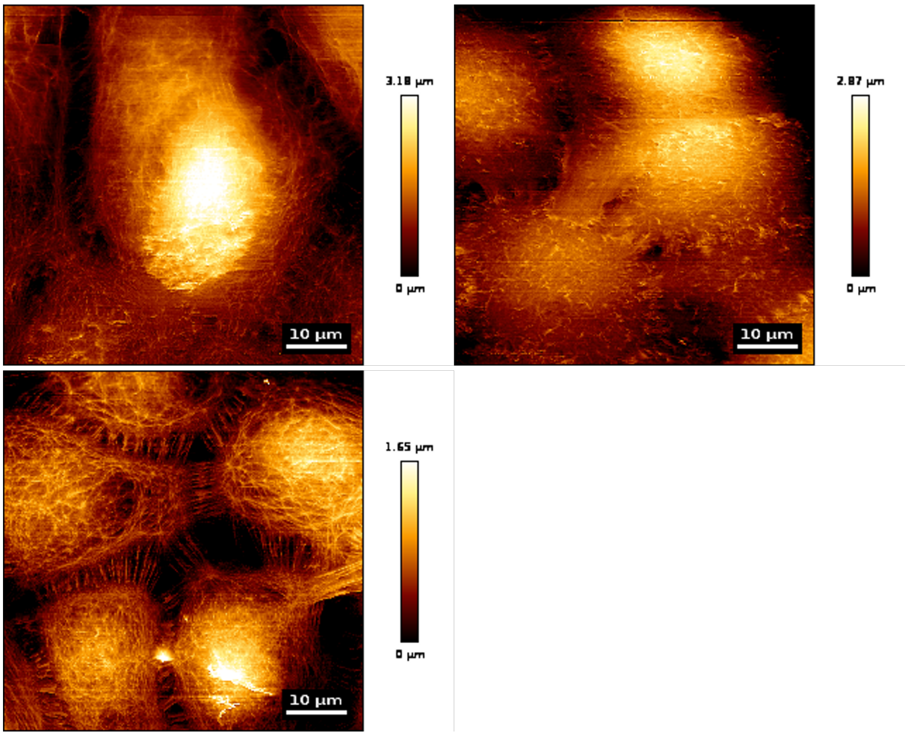

Figure E.1: The AFM height images of UD-SCC-01 cells cultured on the uncoated substrate. The cell height of UD-SCC-01 on the stiff (uncoated) substrate is in the range of 1.65 μm to 3.18 μm. Actin filaments of UD-SCC-01 are not organized and F-actin bundles are oriented randomly with short segments.

E.2 The AFM height images of UD-SCC-1 cells cultured on the gelatin-coated substrate

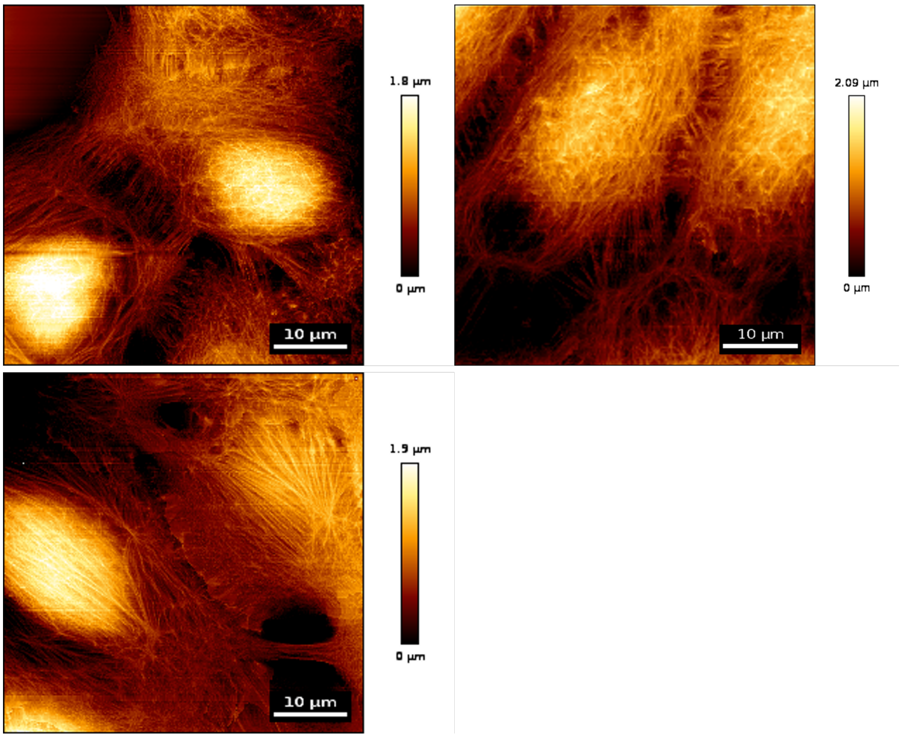

Figure E.2: The AFM height images of UD-SCC-01 cells cultured on the gelatin-coated substrate. The UD-SCC-01 cells on soft (gelatin-coated) substrate possess a cell height of 1.8 μm to 2.09 μm. UD-SCC-01 cells present short actin filaments.

E.3 The AFM height images of squamous carcinoma UD-SCC-2 cells

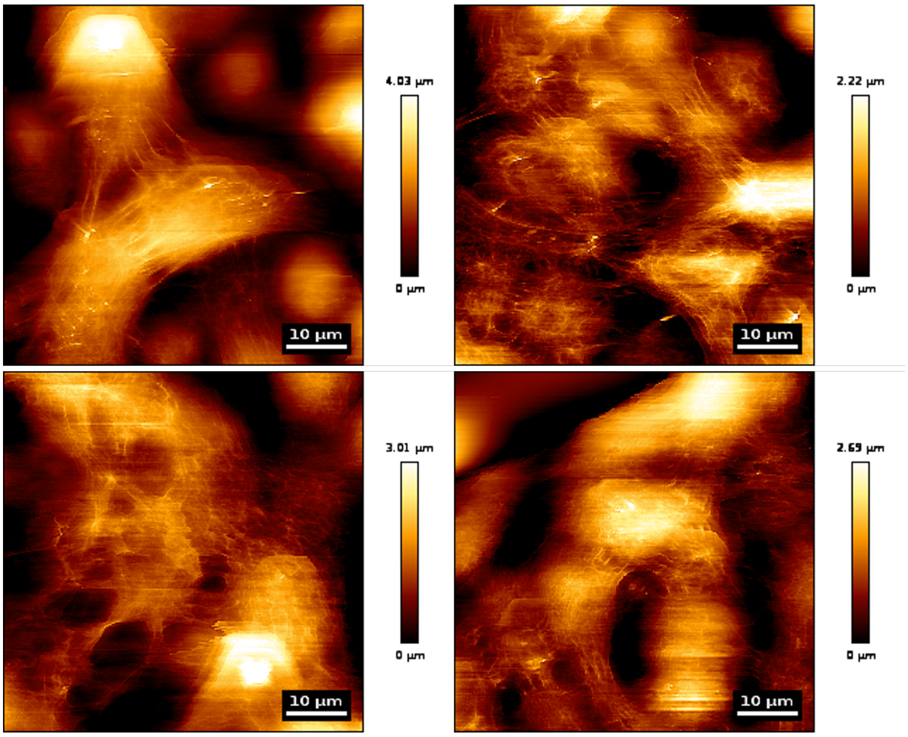

Figure E.3: The AFM height images of UD-SCC-02 cells cultured on the gelatin-coated substrate. UD-SCC-02 cells present small spheroid cell bodies and form clusters containing stress fibers.

E.4 The AFM height images of tongue squamous carcinoma UD-SCC-4 cells

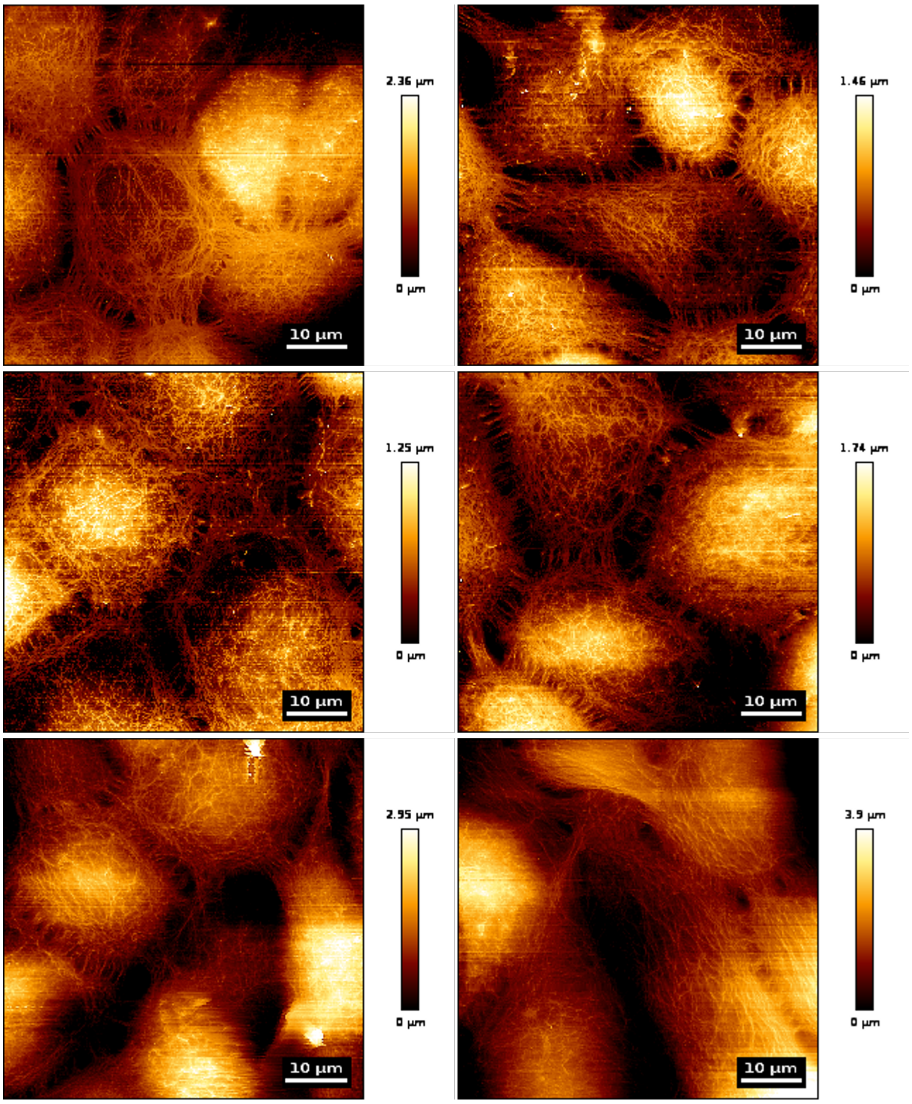

Figure E.4: The AFM height images of UD-SCC-04 cells cultured on the gelatin-coated substrate. In UD-SCC-04 cells, the microfilaments form a web-like meshwork, and actin aggregates are dot-like and arranged in short strands that look like broken or poorly assembled actin structures.

E.5 The AFM height images of tongue squamous carcinoma UD-SCC-6 cells

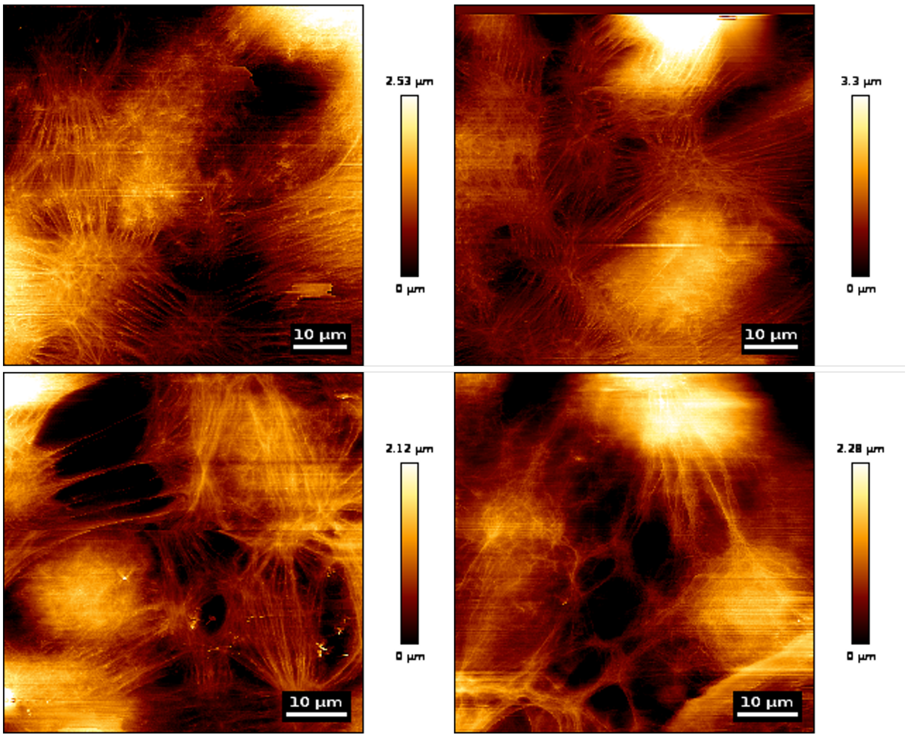

Figure E.5: The AFM height images of UD-SCC-06 cells cultured on the gelatin-coated substrate. UD-SCC-06 cells reveal long, but less-organized microfilaments. The stress fibers are straight and spread disorderly.

E.6 The AFM height images of tongue squamous carcinoma UT-SCC-14 cells

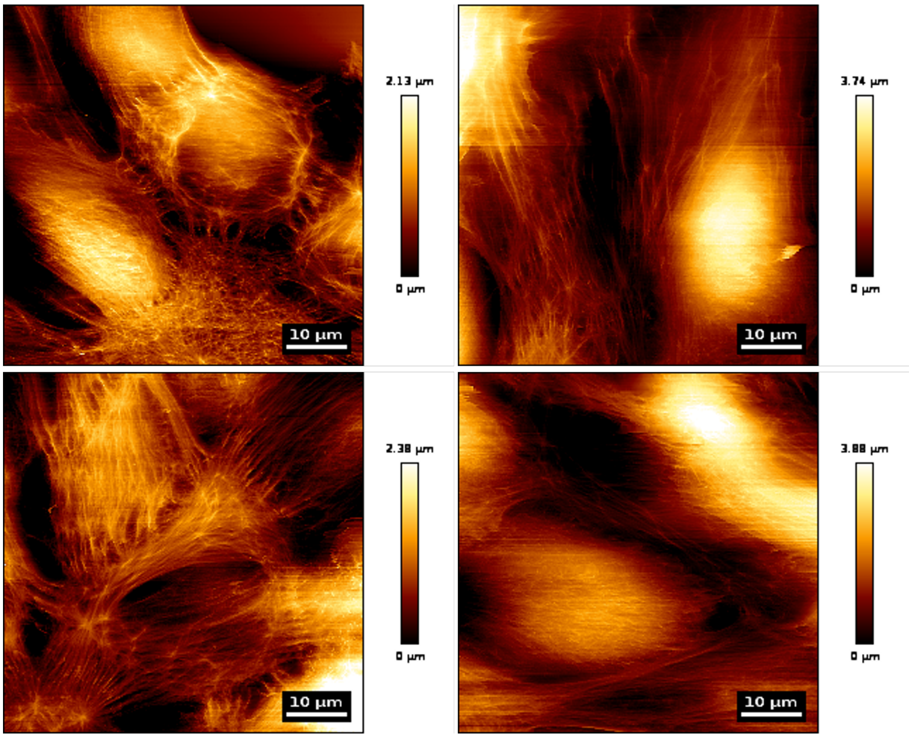

Figure E.6: The AFM height images of UT-SCC-14 cells cultured on the gelatin-coated substrate. A weak actin network is observed in UT-SCC-14 cells. F-actin arranges in a less parallel pattern in the spreading area of the cell surface.

E.7 The AFM height images of metastatic tongue squamous carcinoma UT-SCC-24B cells

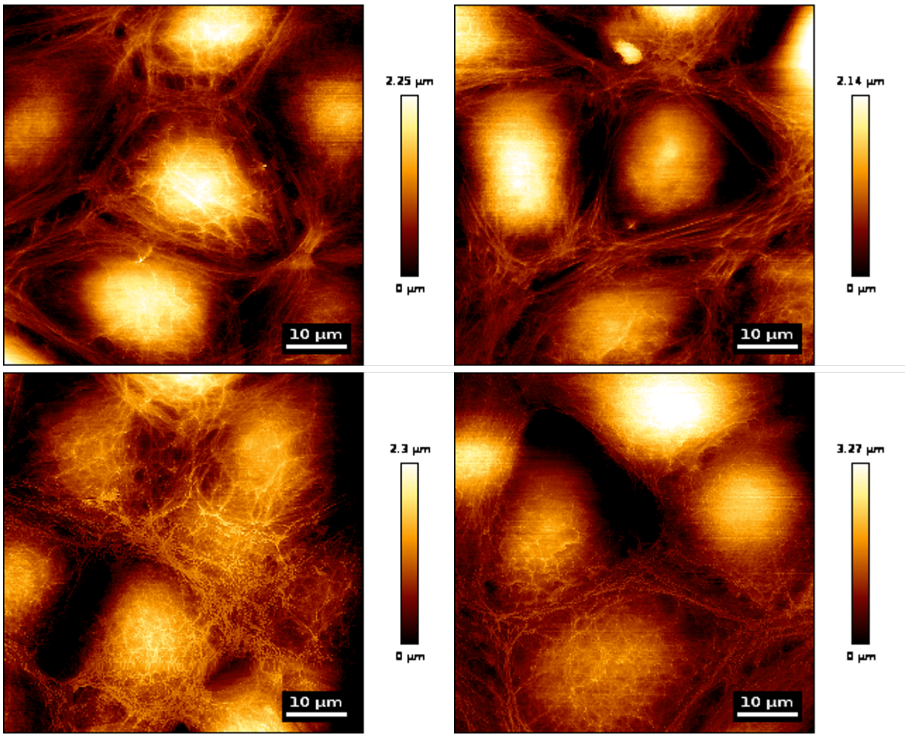

Figure E.7: The AFM height images of UT-SCC-24B cells cultured on the gelatin-coated substrate. Diffused microfilaments are conspicuous in UT-SCC24B cells. The stress fibers arrange in short strands, dotted actin structures form ring-like surrounding the cell body.

E.8 The AFM height images of human dysplastic oral mucosa cells

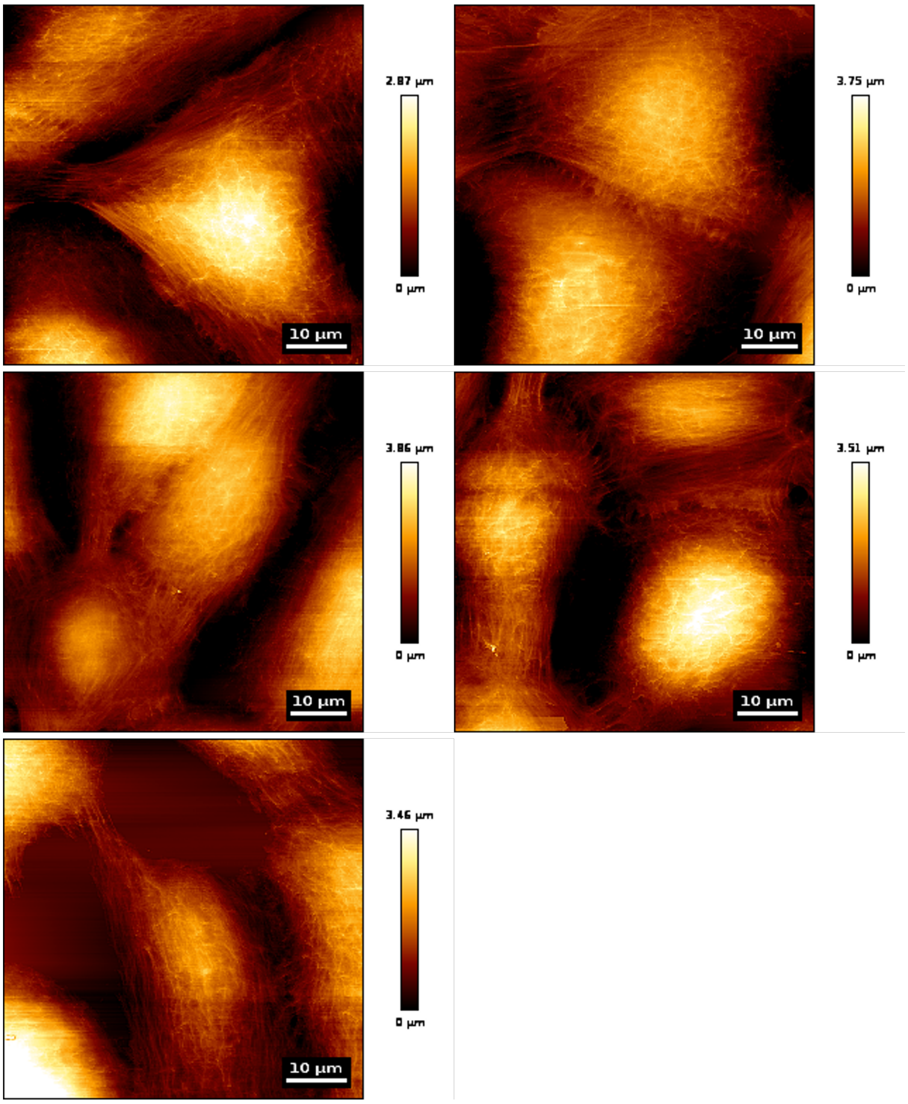

Figure E.8: The AFM height images of DOK cells cultured on the gelatin-coated substrate. A degraded matrix of the actin network is observed in DOK cells. F-actin filaments are thin and fragmented.

E.9 The AFM height images of human oral keratinocyte cells

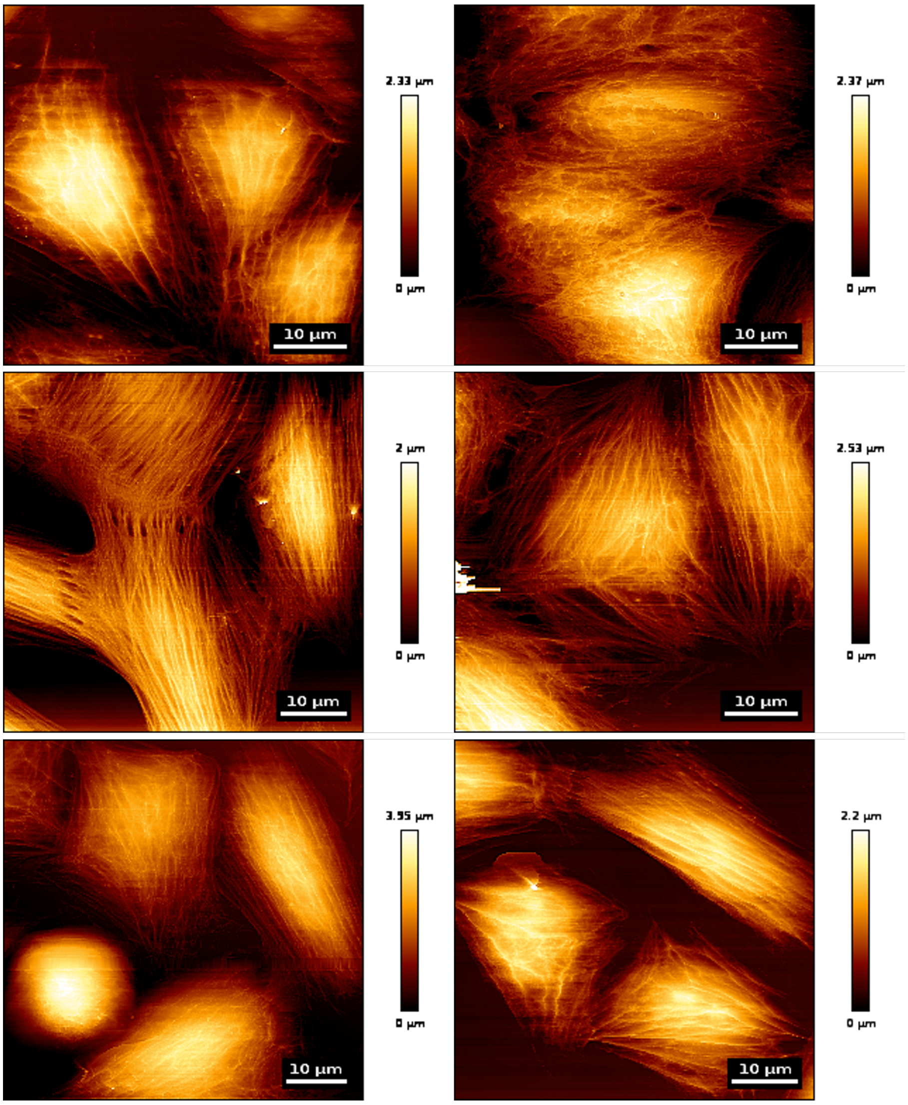

Figure E.9: The AFM height images of HOK cells cultured on the gelatin-coated substrate. HOK cells display a tight filamentous network, the bundles of actin filaments are large, thick-straight, and well-organized. The actin cytoskeleton runs across the cell in a parallel direction.

F Appendix

F.1 The response of UD-SCC-1 cells to the resonance frequency of 24 kHz

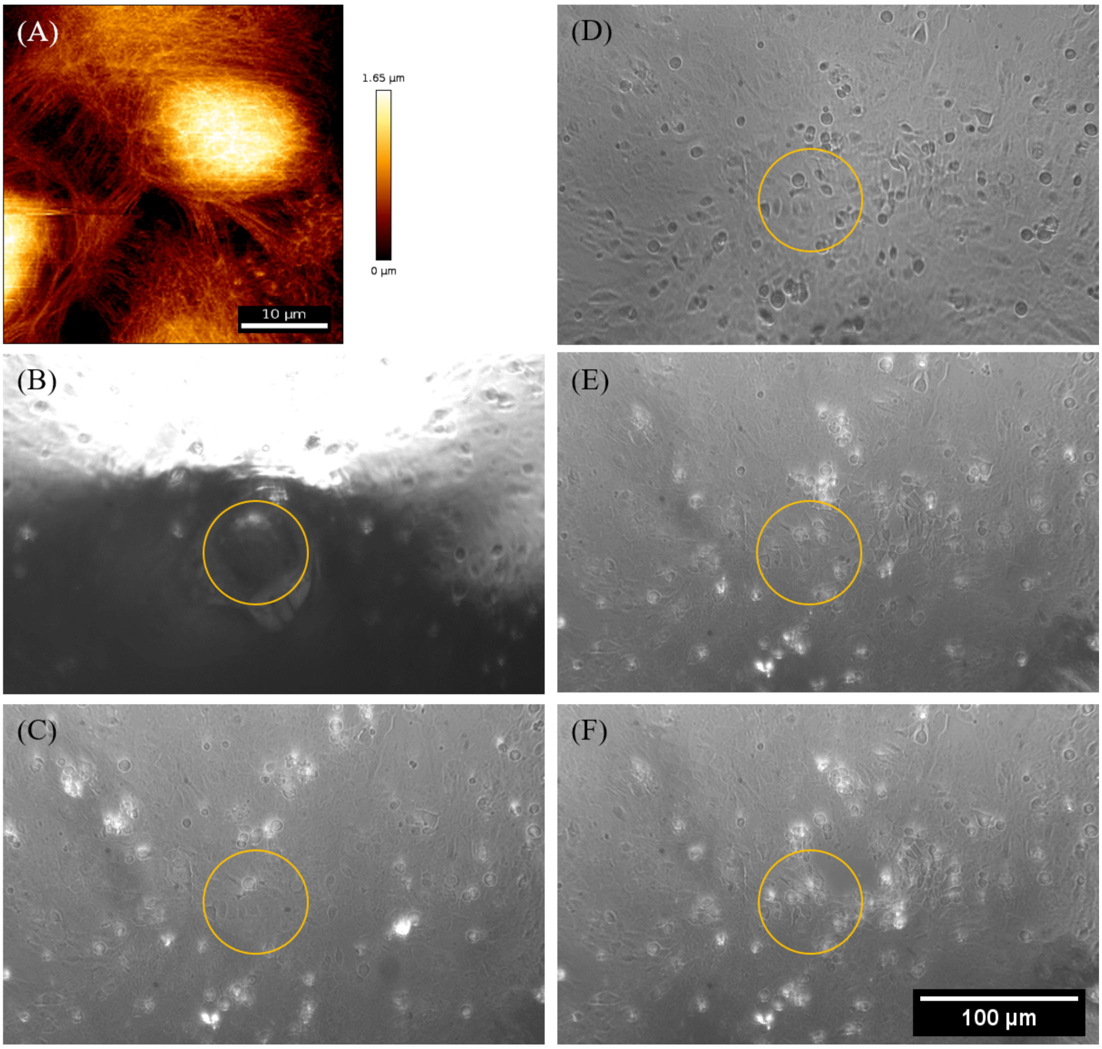

Figure F.10: UD-SCC-1 cells are exposed under the frequency of 24 kHz. The sonotrode is placed over the cell at the distance of 0.05 mm. (A) the AFM height image (B) the tip of sonotrode with the diameter of 65 μm (C) before irradiation (D) after 1 min irradiation (E) after 3 mins irradiation (F) after 5 mins irradiation. Cells exposed to the frequency of 24 kHz, the irradiation-induced cell death.

F.2 The response of UD-SCC-1 cells to the resonance frequency of 67 kHz

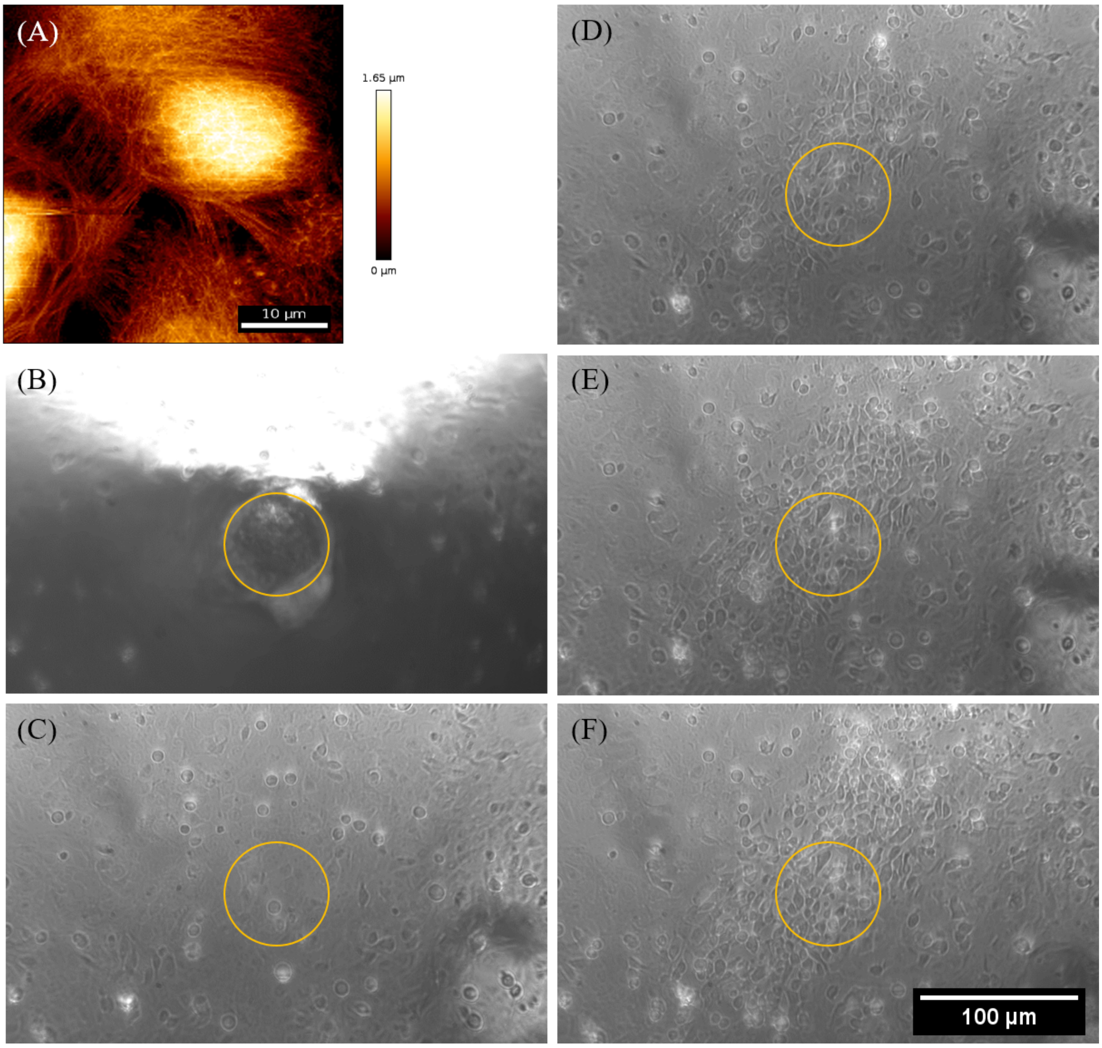

Figure F.11: UD-SCC-1 cells are exposed under the frequency of 67 kHz. The sonotrode is placed over the cell at the distance of 0.05 mm. (A) the AFM height image (B) the tip of sonotrode with the diameter of 65 μm (C) before irradiation (D) after 1 min irradiation (E) after 3 mins irradiation (F) after 5 mins irradiation. When cells were exposed to the frequency of 67 kHz, they changed their cellular morphology.

G Appendix

G.1 The average Young's modulus of human dermal cells

Table G.1: The average Young's modulus of human dermal cells with different conditions

Cell lines (on uncoated substrate)	Relative telomere length (T/S ratio)	Young's modulus of cells' nuclei (kPa)	Young's modulus cell' bodies (kPa)	Young's modulus of cells' peripheral regions (kPa)
HGP003	≈1.75 (low PD)	13.6 ± 5.1 (n = 29)	11.3 ± 5.1 (n = 29)	8.7 ± 3.6 (n = 47)
HGP003-T	≈2.25 (low PD)	14.0 ± 6.0 (n = 21)	12.4 ± 6.4 (n = 21)	11.3 ± 5.3 (n = 41)
HGP164	≈0.625 (high PD)	8.1 ± 3.7 (n = 22)	6.2 ± 2.9 (n = 22)	5.8 ± 3.8 (n = 44)
FN164	≈0.75 (middle PD)	8.3 ± 5.5 (n = 23)	6.5 ± 5.0 (n = 23)	5.8 ± 5.4 (n = 55)
FN164-T	≈1.4 (middle PD)	14.5 ± 4.6 (n = 27)	12.4 ± 3.6 (n = 27)	13.2 ± 4.2 (n = 50)
HGP178	≈1.625 (middle PD)	10.9 ± 5.1 (n = 22)	10.3 ± 4.1 (n = 22)	9.5 ± 4.6 (n = 44)
HGP178-T	≈3.375 (low PD)	7.9 ± 3.1 (n = 25)	6.8 ± 2.5 (n = 25)	7.3 ± 3.3 (n = 48)
811	≈0.53 (middle PD)	6.2 ± 2.9 (n = 23)	5.3 ± 2.0 (n = 23)	5.5 ± 1.9 (n = 32)
811-T	≈1.17 (middle PD)	7.6 ± 3.8 (n = 22)	6.3 ± 3.2 (n = 22)	6.9 ± 4.6 (n = 43)
N14	≈1.25 (middle PD)	9.6 ± 4.8 (n = 26)	7.1 ± 3.0 (n = 26)	6.1 ± 3.5 (n = 49)
N14-T	≈2.625 (middle PD)	9.2 ± 4.8 (n = 22)	6.8 ± 3.6 (n = 22)	6.0 ± 3.7 (n = 41)
N18	≈1.0 (middle PD)	-	-	-
N18-T	≈2.5 (middle PD)	6.5 ± 4.3 (n = 24)	5.8 ± 3.8 (n = 24)	6.2 ± 3.7 (n = 48)
N20	≈1.375 (middle PD)	13.0 ± 6.7 (n = 21)	10.1 ± 7.1 (n = 21)	8.1 ± 5.1 (n = 48)
N20-T	≈4.0 (middle PD)	6.5 ± 4.1 (n = 25)	5.3 ± 3.0 (n = 25)	5.2 ± 4.1 (n = 50)

G.2 The median Young's modulus of human dermal cells

Table G.2: The median Young's modulus of human dermal cells with different conditions

Cell lines (on uncoated substrate)	Relative telomere length (T/S ratio)	Young's modulus of cells' nuclei (kPa)	Young's modulus cell' bodies (kPa)	Young's modulus of cells' peripheral regions (kPa)
HGP003	≈1.75 (low PD)	13.1 ± 5.1 (n = 29)	9.8 ± 5.1 (n = 29)	8.0 ± 3.6 (n = 47)
HGP003-T	≈2.25 (low PD)	14.4 ± 6.0 (n = 21)	14.8 ± 6.4 (n = 21)	12.5 ± 5.3 (n = 41)
HGP164	≈0.625 (high PD)	7.5 ± 3.7 (n = 22)	5.8 ± 2.9 (n = 22)	4.3 ± 3.8 (n = 44)
FN164	≈0.75 (middle PD)	7.6 ± 5.5 (n = 23)	5.8 ± 5.0 (n = 23)	3.4 ± 5.4 (n = 55)
FN164-T	≈1.4 (middle PD)	13.2 ± 4.6 (n = 27)	11.7 ± 3.6 (n = 27)	12.7 ± 4.2 (n = 50)
HGP178	≈1.625 (middle PD)	10.4 ± 5.1 (n = 22)	10.4 ± 4.1 (n = 22)	8.9 ± 4.6 (n = 44)
HGP178-T	≈3.375 (low PD)	7.6 ± 3.1 (n = 25)	6.8 ± 2.5 (n = 25)	7.2 ± 3.3 (n = 48)
811	≈0.53 (middle PD)	5.7 ± 2.9 (n = 23)	5.4 ± 2.0 (n = 23)	5.8 ± 1.9 (n = 32)
811-T	≈1.17 (middle PD)	7.1 ± 3.8 (n = 22)	5.5 ± 3.2 (n = 22)	5.9 ± 4.6 (n = 43)
N14	≈1.25 (middle PD)	8.2 ± 4.8 (n = 26)	6.7 ± 3.0 (n = 26)	5.5 ± 3.5 (n = 49)
N14-T	≈2.625 (middle PD)	8.5 ± 4.8 (n = 22)	6.6 ± 3.6 (n = 22)	5.0 ± 3.7 (n = 41)
N18	≈1.0 (middle PD)	-	-	-
N18-T	≈2.5 (middle PD)	5.4 ± 4.3 (n = 24)	5.3 ± 3.8 (n = 24)	5.6 ± 3.7 (n = 48)
N20	≈1.375 (middle PD)	13.2 ± 6.7 (n = 21)	7.6 ± 7.1 (n = 21)	6.8 ± 5.1 (n = 48)
N20-T	≈4.0 (middle PD)	5.5 ± 4.1 (n = 25)	4.9 ± 3.0 (n = 25)	4.2 ± 4.1 (n = 50)

H Appendix

H.1 The Young's modulus images of human dermal cells with different conditions

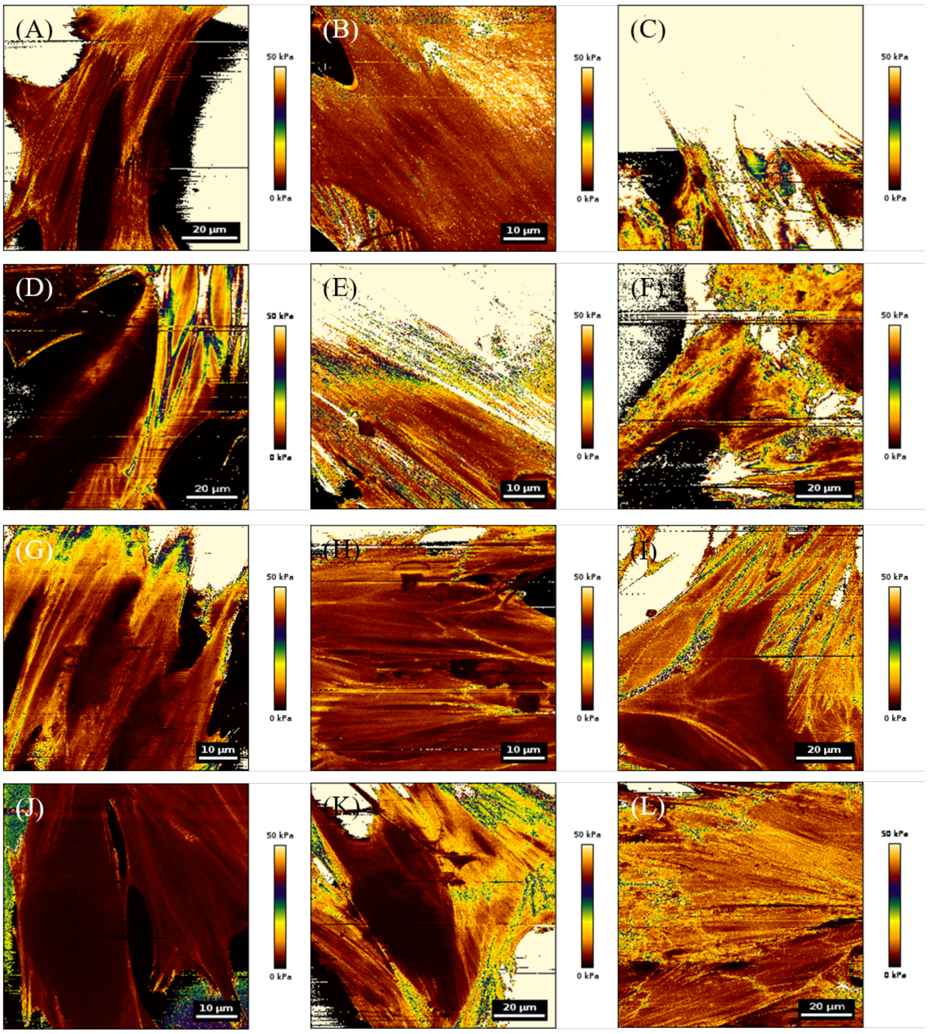

Figure H.1: The Young's modulus images of human dermal cells. (A) HGP003 (B) HGP164 (C) HGP178 (D) HGP003-T (E) FN164-T (F) HGP178-T (G) 811 (H) N14 (I) N20 (J) 811-T (K) N14-T (L) N20-T cells. The Young's modulus is a measure of describing the stiffness or rigidity of a material. The pale-yellow in the images indicates the area of culture substrates, whereas the brown color area points out the location of the cell body.

I Appendix

I.1 The AFM height images of human dermal cells from HGPS003 patient

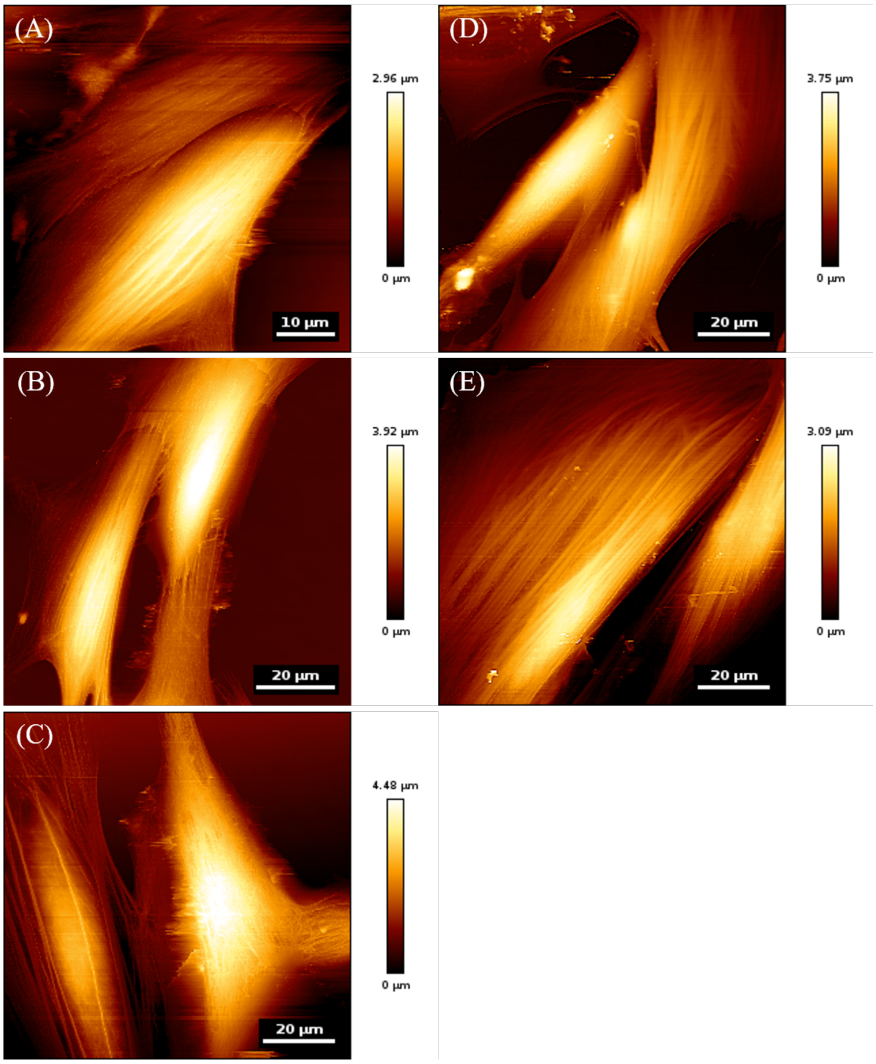

Figure I.2: The AFM height images of HGP003 and HGP003-T fibroblasts cultured on the uncoated substrate. (A-C): HGP003; (D-F): HGP003-T. In presence of hTERT or absence of hTERT, the actin cytoskeleton of fibroblasts presents an extensive network of long stress fibers running across the cell body in the same direction.

I.2 The AFM height images of human dermal cells of HGPS164 patient

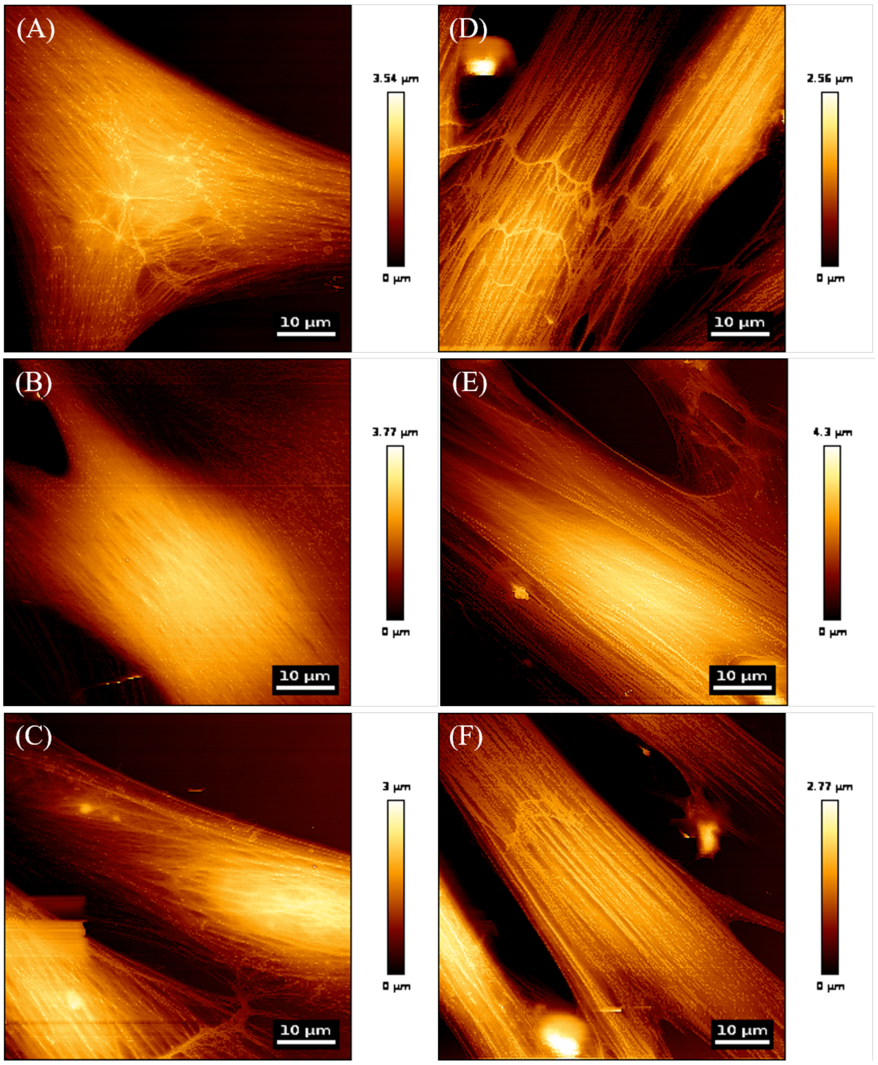

Figure I.3: The AFM height images of HGP164 and FN164-T fibroblasts cultured on the uncoated substrate. (A-C): HGP164; (D-F): FN164-T. Fibroblasts contain a network of thick microfilaments after hTERT treatment.

I.3 The AFM height images of human dermal cells from HGPS178 patient

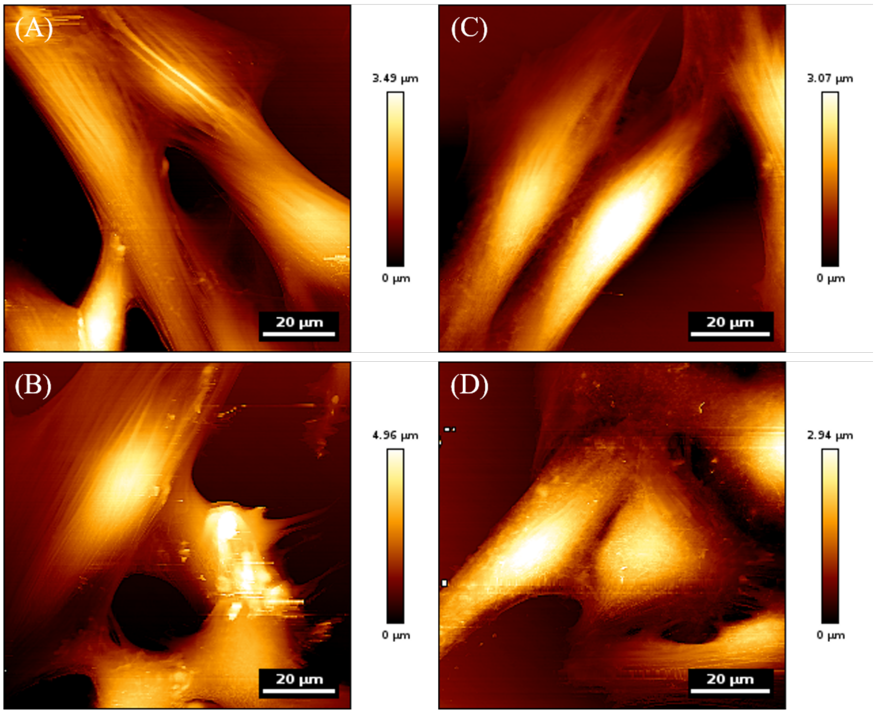

Figure I.4: The AFM height images of HGP178 and 178-T fibroblasts cultured on the uncoated substrate. (A and B): HGP178; (C and D): HGP178-T. The images reveal a slight reorganization of the actin cytoskeleton after the immortalization.

I.4 The AFM height images of human dermal cells from 811 young donor

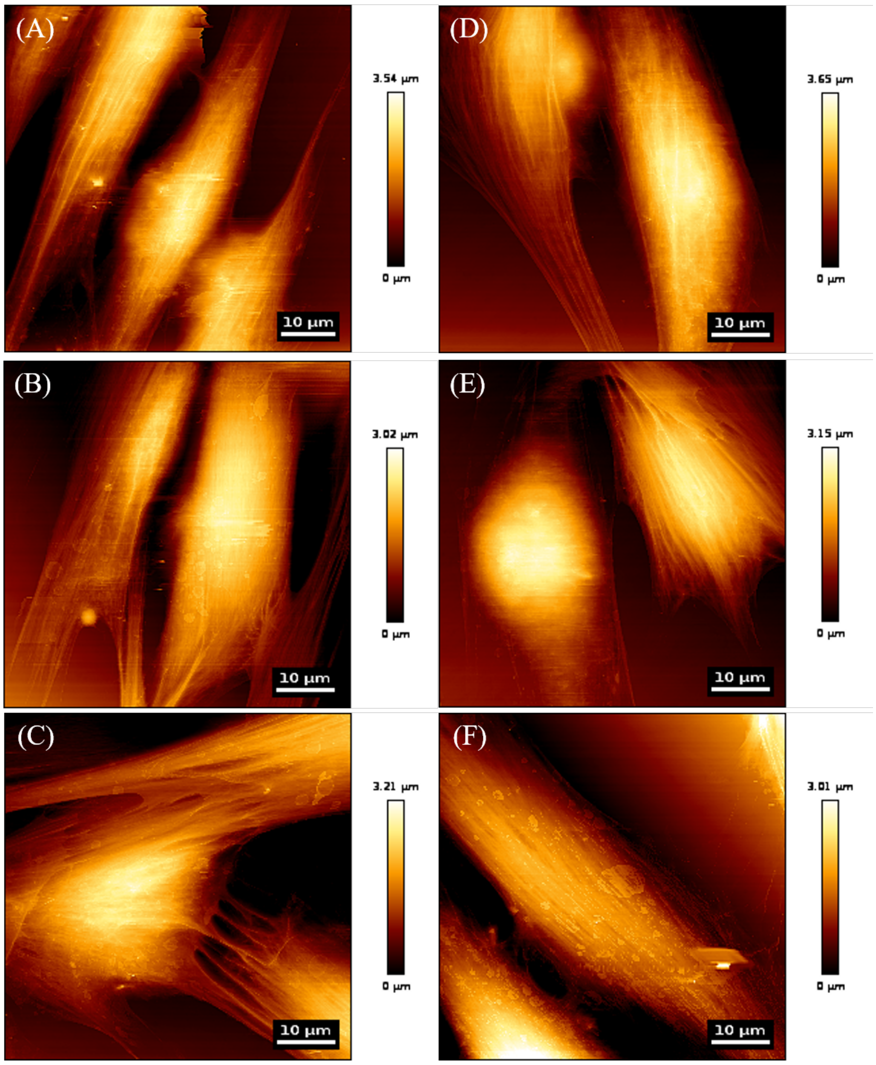

Figure I.5: The AFM height images of 811 and 811-T fibroblasts cultured on the uncoated substrate. (A-C): 811; (D-F): 811-T. Fibroblasts have a typical spindle shape with numerous stress fibers commonly found in spread cells. The immortalization did not dramatically alter the actin filament network.

I.5 The AFM height images of human dermal cells from N14 old donor

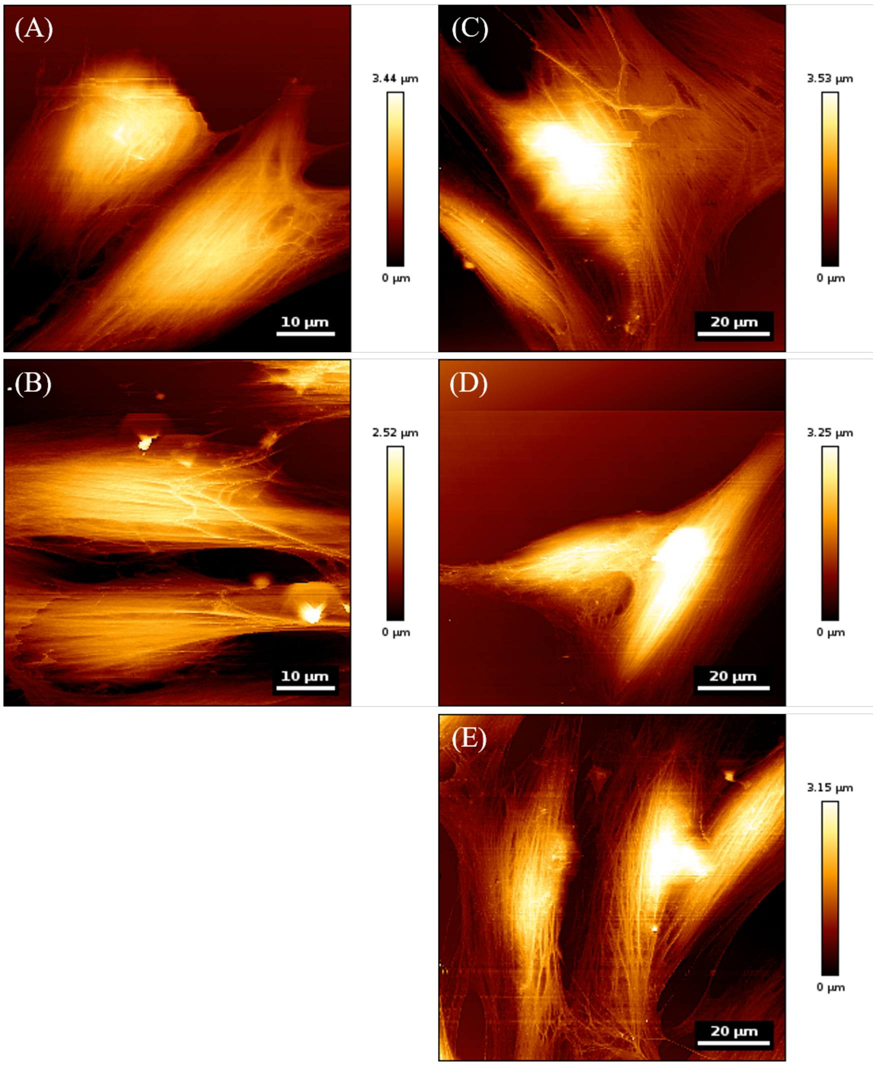

Figure I.6: The AFM height images of N14 and N14-T fibroblasts cultured on the uncoated substrate. (A and B): N14; (C-E): N14-T. The images indicate that the microfilament system did not strongly respond to hTERT treatment.

I.6 The AFM height images of human dermal cells from N18 old donor

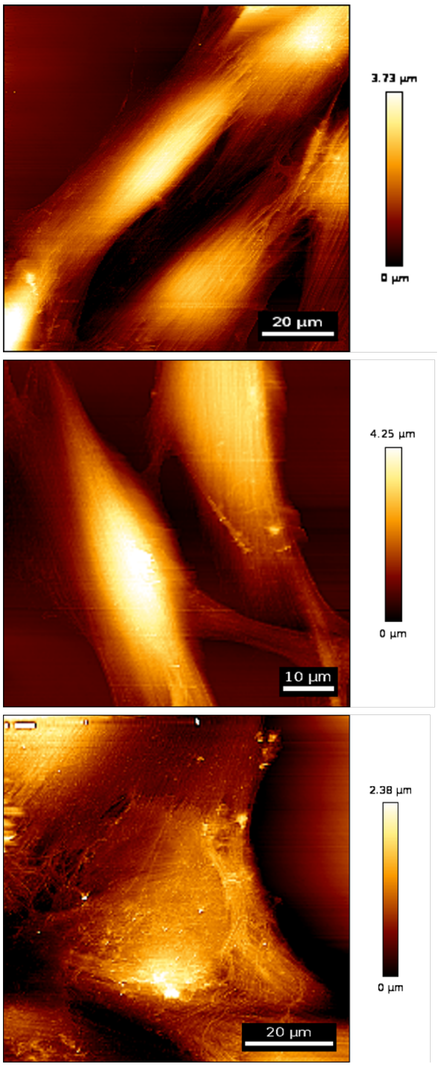

Figure I.7: The AFM height images of N18-T fibroblasts cultured on the uncoated substrate. The fibroblasts appear as spindle-shaped morphology and cells process multilayer structures.

I.7 The AFM height images of human dermal cells from the N20 old donor

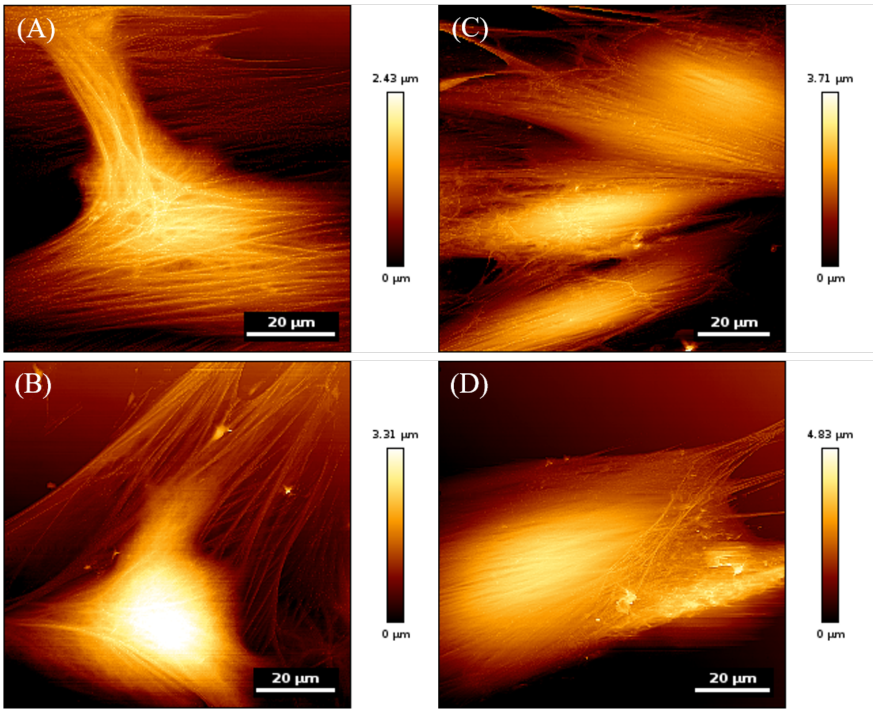

Figure I.8: The AFM height images of N20 and N20-T fibroblasts cultured on the uncoated substrate. (A and B): N20; (C and D): N20-T. Actin structures of N20 cells exhibit an extensive network of long and curved stress fibers through the cell in various directions, whereas the actin filaments are reorganized in N20-T cells, formation is directional.

J Appendix

J.1 The relative telomere length of the human dermal cells

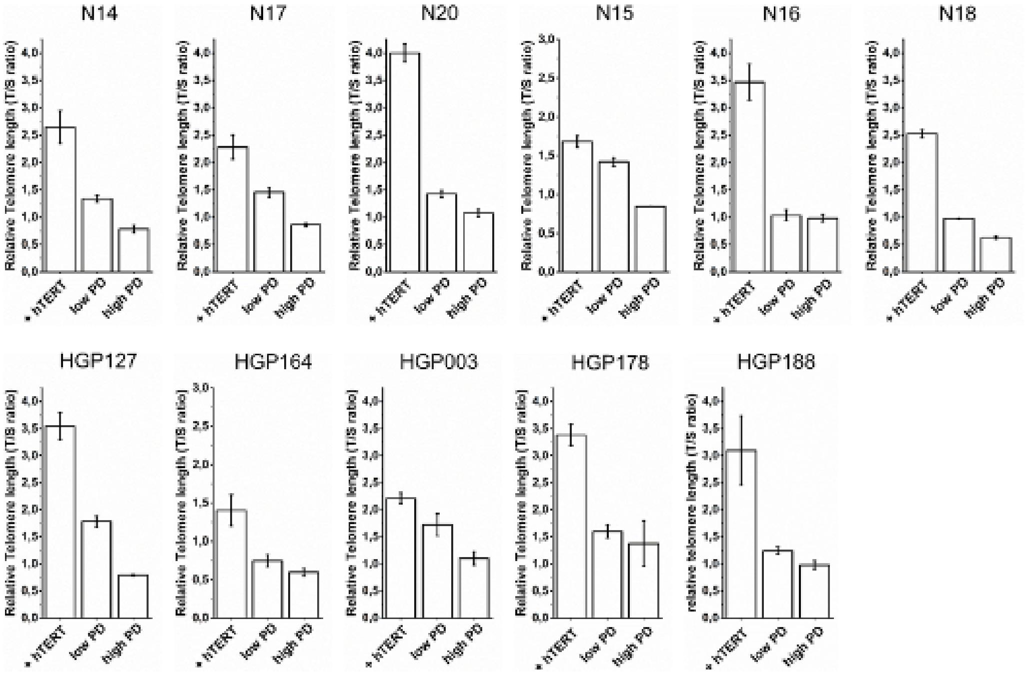

Figure J.1: The relative telomere length (T/S ratio) of fibroblasts.The cellular phenotype of progeria cells is improved by telomere elongation by means of retroviral hTERT infection with the catalytic subunit human telomerase, which successively elongates the shortened telomeres. The image is provided by the group of Prof. Dr. med. Michael Walter. (+hTERT: presenting immortalized cells with elongated telomeres; low PD: telomere length of cells at the low passage before hTERT treatment; high PD: telomere length of cells at the high passage before hTERT treatment; low PD is defined as less than the passage number of 20, while high PD is taken as cells at above passage 40)

K Appendix

K.1 The boxplots and the histogram of human normal and HGPS fibroblasts before-and-after the hTERT treatment

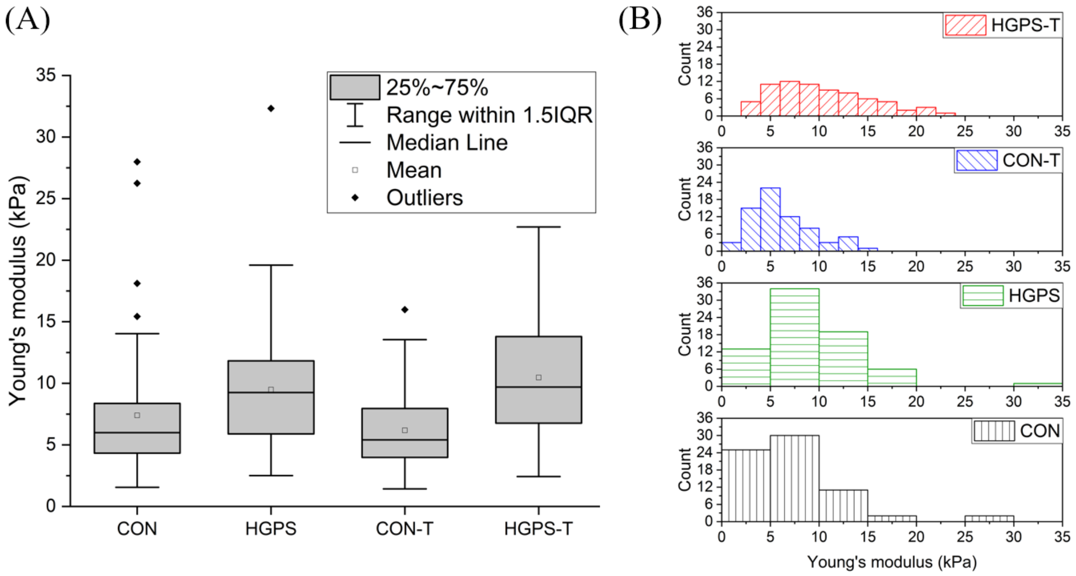

Figure K.1: The boxplots and the histogram of normal and HGPS human fibroblasts. (A) The median value of HGPS fibroblasts is significantly greater than that of normal fibroblasts dspite the hTERT treatment. (B) The data distribution of HGPS fibroblasts is broader than that of normal fibroblasts. CON: fibroblasts from healthy donors; HGPS: fibroblasts from Progeria patients; CON-T: normal fibroblasts after the hTERT treatment; HGPS-T: HGPS fibroblasts after the hTERT treatment.

K.2 The boxplots and the histogram of human fibroblasts before-and-after the hTERT treatment

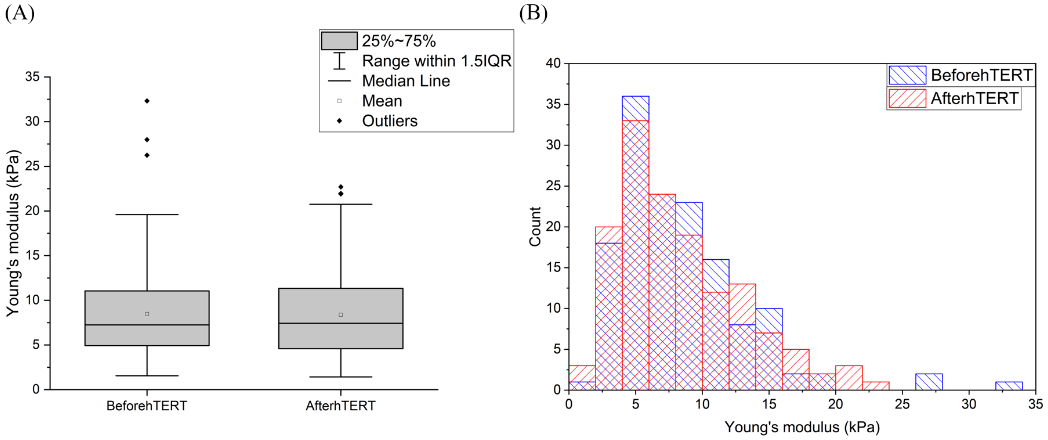

Figure K.2: The boxplots and the histogram of human fibroblasts before-and-after the hTERT treatment (A) No significant differences are found within the groups (B) The data distribution seems not to skew after the treatment. BeforehTERT: HGPS- and normal-fibroblasts before the hTERT treatment; AfterhTERT: HGPS- and normal-fibroblasts after the hTERT treatment.

References

[1] M. H. Pope, “Giovanni alfonso borelli-the father of biomechanics,” *Spine*, vol. 30, no. 20, pp. 2350–2355, 2005.

[2] D. Knudson, *Fundamentals of Biomechanics.* Springer, 2007.

[3] G. Y. Lee and C. T. Lim, “Biomechanics approaches to studying human diseases,” *Trend in biotechnology*, vol. 25, no. 3, pp. 111–118, 2007.

[4] V. De Laurenzi, C. Di Ilio, V. Graziano, N. Allocati, and B. Favaloro, “Role of apoptosis in disease,” *Aging*, vol. 4, no. 5, pp. 330–349, 2012.

[5] X. Su, L. Zhang, H. Kang, B. Zhang, G. Bao, and J. Wang, “Mechanical, nanomorphological and biological reconstruction of early-stage apoptosis in hela cells induced by cytochalasin b,” *Oncology reports*, vol. 41, no. 2, pp. 928–938, 2019.

[6] B. Zhivotovsky and S. Orrenius, “Cell cycle and cell death in disease: past, present and future,” *Journal of internal medicine*, vol. 268, no. 5, pp. 395–409, 2010.

[7] S. Cai, X. Fu, and Z. Sheng, “Dedifferentiation: a new approach in stem cell research,” *BioScience*, vol. 57, no. 8, pp. 655–662, 2007.

[8] K. S. Ko and C. A. McCulloch, “Intercellular mechanotransduction: cellular circuits that coordinate tissue responses to mechanical loading,” *Biochemical and biophysical research communications*, vol. 285, no. 5, pp. 1077–1083, 2001.

[9] F. Martino, A. R. Perestrelo, V. Vinarskỳ, S. Pagliari, and G. Forte, “Cellular mechanotransduction: from tension to function,” *Frontiers in physiology*, vol. 9, p. 824, 2018.

[10] J.-C. Kuo, “Mechanotransduction at focal adhesions: integrating cytoskeletal mechanics in migrating cells,” *Journal of cellular and molecular medicine*, vol. 17, no. 6, pp. 704–712, 2013.

[11] J.-H. Kim, L. J. Dooling, and A. R. Asthagiri, “Intercellular mechanotransduction during multicellular morphodynamics,” *Journal of The Royal Society Interface*, vol. 7, no. suppl_3, pp. S341–S350, 2010.

[12] A. Ashkin, J. M. Dziedzic, J. E. Bjorkholm, and S. Chu, “Observation of a single-beam gradient force optical trap for dielectric particles,” *Optics letters*, vol. 11, no. 5, pp. 288–290, 1986.

[13] A. Ashkin, “Forces of a single-beam gradient laser trap on a dielectric sphere in the ray optics regime,” *Biophysical journal*, vol. 61, no. 2, pp. 569–582, 1992.

[14] T. R. Strick, J.-F. Allemand, D. Bensimon, A. Bensimon, and V. Croquette, “The elasticity of a single supercoiled dna molecule,” *Science*, vol. 271, no. 5257, pp. 1835–1837, 1996.

[15] R. Sarkar and V. V. Rybenkov, “A guide to magnetic tweezers and their applications,” *Frontiers in Physics*, vol. 4, p. 48, 2016.

[16] E. Evans, K. Ritchie, and R. Merkel, “Sensitive force technique to probe molecular adhesion and structural linkages at biological interfaces.,” *Biophysical journal*, vol. 68, no. 6, p. 2580, 1995.

[17] R. M. Hochmuth, “Micropipette aspiration of living cells,” *Journal of biomechanics*, vol. 33, no. 1, pp. 15–22, 2000.

[18] A. L. Weisenhorn, M. Khorsandi, S. Kasas, V. Gotzos, and H.-J. Butt, “Deformation and height anomaly of soft surfaces studied with an afm,” *Nanotechnology*, vol. 4, no. 2, p. 106, 1993.

[19] M. Radmacher, M. Fritz, C. M. Kacher, J. P. Cleveland, and P. K. Hansma, “Measuring the viscoelastic properties of human platelets with the atomic force microscope,” 1996.

[20] B. Vogelstein and K. W. Kinzler, “Cancer genes and the pathways they control,” *Nature medicine*, vol. 10, no. 8, pp. 789–799, 2004.

[21] M. Prokocimer, R. Barkan, and Y. Gruenbaum, "Hutchinson–gilford progeria syndrome through the lens of transcription," *Aging Cell*, vol. 12, no. 4, pp. 533–543, 2013.

[22] U. Aebi, J. Cohn, L. Buhle, and L. Gerace, "The nuclear lamina is a meshwork of intermediate-type filaments," *Nature*, vol. 323, no. 6088, pp. 560–564, 1986.

[23] L. Guelen, L. Pagie, E. Brasset, W. Meuleman, M. B. Faza, W. Talhout, B. H. Eussen, A. de Klein, L. Wessels, W. de Laat, *et al.*, "Domain organization of human chromosomes revealed by mapping of nuclear lamina interactions," *Nature*, vol. 453, no. 7197, pp. 948–951, 2008.

[24] H. J. Worman, "Nuclear lamins and laminopathies," *The Journal of pathology*, vol. 226, no. 2, pp. 316–325, 2012.

[25] K. Apte, R. Stick, and M. Radmacher, "Mechanics in human fibroblasts and progeria: Lamin a mutation e145k results in stiffening of nuclei," *Journal of Molecular Recognition*, vol. 30, no. 2, p. e2580, 2017.

[26] G. Binnig, C. F. Quate, and C. Gerber, "Atomic force microscope," *Physical review letters*, vol. 56, no. 9, p. 930, 1986.

[27] J. Helenius, C.-P. Heisenberg, H. E. Gaub, and D. J. Muller, "Single-cell force spectroscopy," *Journal of cell science*, vol. 121, no. 11, pp. 1785–1791, 2008.

[28] A. I. Gómez-Varela, D. R. Stamov, A. Miranda, R. Alves, C. Barata-Antunes, D. Dambournet, D. G. Drubin, S. Paiva, and P. A. De Beule, "Simultaneous co-localized super-resolution fluorescence microscopy and atomic force microscopy: combined sim and afm platform for the life sciences," *Scientific reports*, vol. 10, no. 1, pp. 1–10, 2020.

[29] H. O. Gautier, A. J. Thompson, S. Achouri, D. E. Koser, K. Holtzmann, E. Moeendarbary, and K. Franze, "Atomic force microscopy-based force measurements on animal cells and tissues," in *Methods in cell biology*, vol. 125, pp. 211–235, Elsevier, 2015.

[30] Z. Xin, G. Lin, H. Lei, T. F. Lue, and Y. Guo, "Clinical applications of low-intensity pulsed ultrasound and its potential role in urology," *Translational andrology and urology*, vol. 5, no. 2, p. 255, 2016.

[31] D. Dalecki, "Mechanical bioeffects of ultrasound," *Annu. Rev. Biomed. Eng.*, vol. 6, pp. 229–248, 2004.

[32] H. M. Santos and C. Lodeiro, "The power of ultrasound," Wiley Online Library, 2009.

[33] M. Ashokkumar, "The characterization of acoustic cavitation bubbles–an overview," *Ultrasonics sonochemistry*, vol. 18, no. 4, pp. 864–872, 2011.

[34] Z. Izadifar, Z. Izadifar, D. Chapman, and P. Babyn, "An introduction to high intensity focused ultrasound: Systematic review on principles, devices, and clinical applications," *Journal of Clinical Medicine*, vol. 9, no. 2, p. 460, 2020.

[35] . G. ter Haar and C. Coussios, "High intensity focused ultrasound: physical principles and devices," *International journal of hyperthermia*, vol. 23, no. 2, pp. 89–104, 2007.

[36] G. Ter Haar, "Therapeutic ultrasound," *European Journal of ultrasound*, vol. 9, no. 1, pp. 3–9, 1999.

[37] D. R. Mittelstein, J. Ye, E. F. Schibber, A. Roychoudhury, L. T. Martinez, M. H. Fekrazad, M. Ortiz, P. P. Lee, M. G. Shapiro, and M. Gharib, "Selective ablation of cancer cells with low intensity pulsed ultrasound," *Applied Physics Letters*, vol. 116, no. 1, p. 013701, 2020.

[38] H. Ballo, P. Koldovsky, T. Hoffmann, V. Balz, B. Hildebrandt, C. Gerharz, and H. Bier, "Establishment and characterization of four cell lines derived from human head and neck squamous cell carcinomas for an autologous tumor-fibroblast in vitro model.," *Anticancer research*, vol. 19, no. 5B, p. 3827, 1999.

[39] W. Eicheler, D. Zips, A. Dörfler, R. Grénman, and M. Baumann, “Splicing mutations in tp53 in human squamous cell carcinoma lines influence immunohistochemical detection,” *Journal of histochemistry & cytochemistry*, vol. 50, no. 2, pp. 197–204, 2002.

[40] S. E. Chang, S. Foster, D. Betts, and W. E. Marnock, “Dok, a cell line established from human dysplastic oral mucosa, shows a partially transformed non-malignant phenotype,” *International journal of cancer*, vol. 52, no. 6, pp. 896–902, 1992.

[41] C. Lundqvist, V. Baranov, S. Teglund, S. Hammarström, and M.-L. Hammarström, “Cytokine profile and ultrastructure of intraepithelial gamma delta t cells in chronically inflamed human gingiva suggest a cytotoxic effector function.,” *The Journal of Immunology*, vol. 153, no. 5, pp. 2302–2312, 1994.

[42] H. Janovjak, J. Struckmeier, and D. J. Müller, “Hydrodynamic effects in fast afm single-molecule force measurements,” *European Biophysics Journal*, vol. 34, no. 1, pp. 91–96, 2005.

[43] J. Alcaraz, L. Buscemi, M. Puig-de Morales, J. Colchero, A. Baro, and D. Navajas, “Correction of microrheological measurements of soft samples with atomic force microscopy for the hydrodynamic drag on the cantilever,” *Langmuir*, vol. 18, no. 3, pp. 716–721, 2002.

[44] D. Wang, P. Yu, F. Wang, H.-Y. Chan, L. Zhou, Z. Dong, L. Liu, and W. J. Li, “Improving atomic force microscopy imaging by a direct inverse asymmetric pi hysteresis model,” *Sensors*, vol. 15, no. 2, pp. 3409–3425, 2015.

[45] H. Habibullah, “30 years of atomic force microscopy: Creep, hysteresis, cross-coupling, and vibration problems of piezoelectric tube scanners,” *Measurement*, vol. 159, p. 107776, 2020.

[46] A. Weisenhorn, P. Hansma, T. Albrecht, and C. Quate, “Forces in atomic force microscopy in air and water,” *Applied physics letters*, vol. 54, no. 26, pp. 2651–2653, 1989.

[47] B. Drake, C. Prater, A. Weisenhorn, S. Gould, T. Albrecht, C. Quate, D. Cannell, H. Hansma, and P. Hansma, "Imaging crystals, polymers, and processes in water with the atomic force microscope," *Science*, vol. 243, no. 4898, pp. 1586–1589, 1989.

[48] T. Yeung, P. C. Georges, L. A. Flanagan, B. Marg, M. Ortiz, M. Funaki, N. Zahir, W. Ming, V. Weaver, and P. A. Janmey, "Effects of substrate stiffness on cell morphology, cytoskeletal structure, and adhesion," *Cell motility and the cytoskeleton*, vol. 60, no. 1, pp. 24–34, 2005.

[49] E. Terentjev, S. Bell, and A.-L. Redmann, "Universal kinetics for engagement of mechanosensing pathways in cell adhesion," *bioRxiv*, p. 292367, 2018.

[50] M. Lekka, D. Gil, K. Pogoda, J. Dulińska-Litewka, R. Jach, J. Gostek, O. Klymenko, S. Prauzner-Bechcicki, Z. Stachura, J. Wiltowska-Zuber, *et al.*, "Cancer cell detection in tissue sections using afm," *Archives of biochemistry and biophysics*, vol. 518, no. 2, pp. 151–156, 2012.

[51] D. E. Discher, P. Janmey, and Y.-l. Wang, "Tissue cells feel and respond to the stiffness of their substrate," *Science*, vol. 310, no. 5751, pp. 1139–1143, 2005.

[52] R. J. Pelham and Y.-l. Wang, "Cell locomotion and focal adhesions are regulated by substrate flexibility," *Proceedings of the National Academy of Sciences*, vol. 94, no. 25, pp. 13661–13665, 1997.

[53] A. Engler, L. Bacakova, C. Newman, A. Hategan, M. Griffin, and D. Discher, "Substrate compliance versus ligand density in cell on gel responses," *Biophysical journal*, vol. 86, no. 1, pp. 617–628, 2004.

[54] S. Jalali, M. Tafazzoli-Shadpour, N. Haghighipour, R. Omidvar, and F. Safshekan, "Regulation of endothelial cell adherence and elastic modulus by substrate stiffness," *Cell communication & adhesion*, vol. 22, no. 2-6, pp. 79–89, 2015.

[55] K. Mollaeian, Y. Liu, S. Bi, and J. Ren, “Investigation of the effect of substrate morphology on mdck cell mechanical behavior using atomic force microscopy,” *Applied Physics Letters*, vol. 115, no. 6, p. 063701, 2019.

[56] Y. F. Dufrêne and A. E. Pelling, “Force nanoscopy of cell mechanics and cell adhesion,” *Nanoscale*, vol. 5, no. 10, pp. 4094–4104, 2013.

[57] E. Thormann, J. K. Dreyer, A. C. Simonsen, P. L. Hansen, S. Hansen, U. Holmskov, and O. G. Mouritsen, “Dynamic strength of the interaction between lung surfactant protein d (sp-d) and saccharide ligands,” *Biochemistry*, vol. 46, no. 43, pp. 12231–12237, 2007.

[58] N. Gavara, “A beginner’s guide to atomic force microscopy probing for cell mechanics,” *Microscopy research and technique*, vol. 80, no. 1, pp. 75–84, 2017.

[59] Y.-W. Chiou, H.-K. Lin, M.-J. Tang, H.-H. Lin, and M.-L. Yeh, “The influence of physical and physiological cues on atomic force microscopy-based cell stiffness assessment,” *PloS one*, vol. 8, no. 10, p. e77384, 2013.

[60] N. Craig, “Effect of reduced temperatures on protein synthesis in mouse l cells,” *Cell*, vol. 4, no. 4, pp. 329–335, 1975.

[61] I. Watanabe and S. Okada, “Effects of temperature on growth rate of cultured mammalian cells (l5178y),” *The Journal of cell biology*, vol. 32, no. 2, pp. 309–323, 1967.

[62] K. Ranganathan and L. Kavitha, “Oral epithelial dysplasia: Classifications and clinical relevance in risk assessment of oral potentially malignant disorders,” *Journal of oral and maxillofacial pathology: JOMFP*, vol. 23, no. 1, p. 19, 2019.

[63] E. Henderson, P. Haydon, and D. Sakaguchi, “Actin filament dynamics in living glial cells imaged by atomic force microscopy,” *Science*, vol. 257, no. 5078, pp. 1944–1946, 1992.

[64] W. Xu, R. Mezencev, B. Kim, L. Wang, J. McDonald, and T. Sulchek, "Cell stiffness is a biomarker of the metastatic potential of ovarian cancer cells," *PloS one*, vol. 7, no. 10, p. e46609, 2012.

[65] Y. M. Efremov, M. Lomakina, D. Bagrov, P. Makhnovskiy, A. Alexandrova, M. Kirpichnikov, and K. Shaitan, "Mechanical properties of fibroblasts depend on level of cancer transformation," *Biochimica et Biophysica Acta (BBA)-Molecular Cell Research*, vol. 1843, no. 5, pp. 1013–1019, 2014.

[66] Q. Li, G. Y. Lee, C. N. Ong, and C. T. Lim, "Afm indentation study of breast cancer cells," *Biochemical and biophysical research communications*, vol. 374, no. 4, pp. 609–613, 2008.

[67] H. Haga, S. Sasaki, K. Kawabata, E. Ito, T. Ushiki, and T. Sambongi, "Elasticity mapping of living fibroblasts by afm and immunofluorescence observation of the cytoskeleton," *Ultramicroscopy*, vol. 82, no. 1-4, pp. 253–258, 2000.

[68] C. Rotsch and M. Radmacher, "Drug-induced changes of cytoskeletal structure and mechanics in fibroblasts: an atomic force microscopy study," *Biophysical journal*, vol. 78, no. 1, pp. 520–535, 2000.

[69] K. Mollaeian, Y. Liu, S. Bi, and J. Ren, "Atomic force microscopy study revealed velocity-dependence and nonlinearity of nanoscale poroelasticity of eukaryotic cells," *Journal of the mechanical behavior of biomedical materials*, vol. 78, pp. 65–73, 2018.

[70] N. Lichtenstein, B. Geiger, and Z. Kam, "Quantitative analysis of cytoskeletal organization by digital fluorescent microscopy," *Cytometry Part A: The Journal of the International Society for Analytical Cytology*, vol. 54, no. 1, pp. 8–18, 2003.

[71] P. A. Pullarkat, P. A. Fernández, and A. Ott, "Rheological properties of the eukaryotic cell cytoskeleton," *Physics Reports*, vol. 449, no. 1-3, pp. 29–53, 2007.

[72] D. A. Fletcher and R. D. Mullins, "Cell mechanics and the cytoskeleton," *Nature*, vol. 463, no. 7280, pp. 485–492, 2010.

[73] J. Guck, S. Schinkinger, B. Lincoln, F. Wottawah, S. Ebert, M. Romeyke, D. Lenz, H. M. Erickson, R. Ananthakrishnan, D. Mitchell, *et al.*, "Optical deformability as an inherent cell marker for testing malignant transformation and metastatic competence," *Biophysical journal*, vol. 88, no. 5, pp. 3689–3698, 2005.

[74] M. Lekka, "Discrimination between normal and cancerous cells using afm," *Bionanoscience*, vol. 6, no. 1, pp. 65–80, 2016.

[75] S. Park, W.-J. Jang, and C.-H. Jeong, "Nano-biomechanical validation of epithelialmesenchymal transition in oral squamous cell carcinomas," *Biological and Pharmaceutical Bulletin*, vol. 39, no. 9, pp. 1488–1495, 2016.

[76] Z. Zhou, C. Zheng, S. Li, X. Zhou, Z. Liu, Q. He, N. Zhang, A. Ngan, B. Tang, and A. Wang, "Afm nanoindentation detection of the elastic modulus of tongue squamous carcinoma cells with different metastatic potentials," *Nanomedicine: Nanotechnology, Biology and Medicine*, vol. 9, no. 7, pp. 864–874, 2013.

[77] S. E. Cross, Y.-S. Jin, J. Rao, and J. K. Gimzewski, "Nanomechanical analysis of cells from cancer patients," *Nature nanotechnology*, vol. 2, no. 12, pp. 780–783, 2007.

[78] S. E. Cross, Y.-S. Jin, J. Tondre, R. Wong, J. Rao, and J. K. Gimzewski, "Afm-based analysis of human metastatic cancer cells," *Nanotechnology*, vol. 19, no. 38, p. 384003, 2008.

[79] G. Tang, M. Galluzzi, B. Zhang, Y.-L. Shen, and F. J. Stadler, "Biomechanical heterogeneity of living cells: Comparison between atomic force microscopy and finite element simulation," *Langmuir*, vol. 35, no. 23, pp. 7578–7587, 2018.

[80] Y. M. Efremov, A. Dokrunova, A. Efremenko, M. Kirpichnikov, K. Shaitan, and O. Sokolova, "Distinct impact of targeted actin cytoskeleton reorganiza-

tion on mechanical properties of normal and malignant cells," *Biochimica et Biophysica Acta (BBA)-Molecular Cell Research*, vol. 1853, no. 11, pp. 3117–3125, 2015.

[81] A. Raz and B. Geiger, "Altered organization of cell-substrate contacts and membrane-associated cytoskeleton in tumor cell variants exhibiting different metastatic capabilities," *Cancer Research*, vol. 42, no. 12, pp. 5183–5190, 1982.

[82] S. Heyden and M. Ortiz, "Oncotripsy: Targeting cancer cells selectively via resonant harmonic excitation," *Journal of the Mechanics and Physics of Solids*, vol. 92, pp. 164–175, 2016.

[83] S. Heyden and M. Ortiz, "Investigation of the influence of viscoelasticity on oncotripsy," *Computer Methods in Applied Mechanics and Engineering*, vol. 314, pp. 314–322, 2017.

[84] T. Dechat, K. Pfleghaar, K. Sengupta, T. Shimi, D. K. Shumaker, L. Solimando, and R. D. Goldman, "Nuclear lamins: major factors in the structural organization and function of the nucleus and chromatin," *Genes & development*, vol. 22, no. 7, pp. 832–853, 2008.

[85] P. Scaffidi and T. Misteli, "Lamin a-dependent nuclear defects in human aging," *Science*, vol. 312, no. 5776, pp. 1059–1063, 2006.

[86] V. V. Ashapkin, L. I. Kutueva, S. Y. Kurchashova, and I. I. Kireev, "Are there common mechanisms between the hutchinson–gilford progeria syndrome and natural aging?," *Frontiers in genetics*, vol. 10, p. 455, 2019.

[87] L. Daniali, A. Benetos, E. Susser, J. D. Kark, C. Labat, M. Kimura, K. K. Desai, M. Granick, and A. Aviv, "Telomeres shorten at equivalent rates in somatic tissues of adults," *Nature communications*, vol. 4, no. 1, pp. 1–7, 2013.

[88] C. D. Ragnauth, D. T. Warren, Y. Liu, R. McNair, T. Tajsic, N. Figg, R. Shroff, J. Skepper, and C. M. Shanahan, "Clinical perspective," *Circulation*, vol. 121, no. 20, pp. 2200–2210, 2010.

[89] K. A. Mather, A. F. Jorm, R. A. Parslow, and H. Christensen, “Is telomere length a biomarker of aging? a review,” *Journals of Gerontology Series A: Biomedical Sciences and Medical Sciences*, vol. 66, no. 2, pp. 202–213, 2011.

[90] J. Ramunas, E. Yakubov, J. J. Brady, S. Y. Corbel, C. Holbrook, M. Brandt, J. Stein, J. G. Santiago, J. P. Cooke, and H. M. Blau, “Transient delivery of modified mrna encoding tert rapidly extends telomeres in human cells,” *The FASEB Journal*, vol. 29, no. 5, pp. 1930–1939, 2015.

[91] Y. Li, G. Zhou, I. G. Bruno, N. Zhang, S. Sho, E. Tedone, T.-P. Lai, J. P. Cooke, and J. W. Shay, “Transient introduction of human telomerase mrna improves hallmarks of progeria cells,” *Aging cell*, vol. 18, no. 4, p. e12979, 2019.

[92] S. Vidak and R. Foisner, “Molecular insights into the premature aging disease progeria,” *Histochemistry and cell biology*, vol. 145, no. 4, pp. 401–417, 2016.

[93] S. Cho, A. Abbas, J. Irianto, I. L. Ivanovska, Y. Xia, M. Tewari, and D. E. Discher, “Progerin phosphorylation in interphase is lower and less mechanosensitive than lamin-a, c in ips-derived mesenchymal stem cells,” *Nucleus*, vol. 9, no. 1, pp. 235–250, 2018.

[94] D. McClintock, L. B. Gordon, and K. Djabali, “Hutchinson–gilford progeria mutant lamin a primarily targets human vascular cells as detected by an anti-lamin a g608g antibody,” *Proceedings of the National Academy of Sciences*, vol. 103, no. 7, pp. 2154–2159, 2006.

[95] M. U. Bikkul, R. G. Faragher, G. Worthington, P. Meinke, A. R. Kerr, A. Sammy, K. Riyahi, D. Horton, E. C. Schirmer, M. Hubank, *et al.*, “Telomere elongation through htert immortalization leads to chromosome repositioning in control cells and genomic instability in hutchinson-gilford progeria syndrome fibroblasts, expressing a novel sun1 isoform,” *Genes, Chromosomes and Cancer*, vol. 58, no. 6, pp. 341–356, 2019.

[96] A. G. Bodnar, M. Ouellette, M. Frolkis, S. E. Holt, C.-P. Chiu, G. B. Morin, C. B. Harley, J. W. Shay, S. Lichtsteiner, and W. E. Wright, “Extension of

life-span by introduction of telomerase into normal human cells," *science*, vol. 279, no. 5349, pp. 349–352, 1998.

[97] M. Jaskelioff, F. L. Muller, J.-H. Paik, E. Thomas, S. Jiang, A. C. Adams, E. Sahin, M. Kost-Alimova, A. Protopopov, J. Cadinanos, *et al.*, "Telomerase reactivation reverses tissue degeneration in aged telomerase-deficient mice," *Nature*, vol. 469, no. 7328, pp. 102–106, 2011.

[98] B. B. de Jesus and M. A. Blasco, "Aging by telomere loss can be reversed," *Cell Stem Cell*, vol. 8, no. 1, pp. 3–4, 2011.

[99] R. Burla, M. La Torre, and I. Saggio, "Mammalian telomeres and their partnership with lamins," *Nucleus*, vol. 7, no. 2, pp. 187–202, 2016.

[100] R. D. Goldman, D. K. Shumaker, M. R. Erdos, M. Eriksson, A. E. Goldman, L. B. Gordon, Y. Gruenbaum, S. Khuon, M. Mendez, R. Varga, *et al.*, "Accumulation of mutant lamin a causes progressive changes in nuclear architecture in hutchinson–gilford progeria syndrome," *Proceedings of the National Academy of Sciences*, vol. 101, no. 24, pp. 8963–8968, 2004.

[101] A. Chojnowski, P. F. Ong, E. S. Wong, J. S. Lim, R. A. Mutalif, R. Navasankari, B. Dutta, H. Yang, Y. Y. Liow, S. K. Sze, *et al.*, "Progerin reduces lap2α-telomere association in hutchinson-gilford progeria," *Elife*, vol. 4, p. e07759, 2015.

[102] T. A. Dittmer and T. Misteli, "The lamin protein family," *Genome biology*, vol. 12, no. 5, pp. 1–14, 2011.

[103] Z. Jahed, H. Hao, V. Thakkar, U. T. Vu, V. A. Valdez, A. Rathish, C. Tolentino, S. C. Kim, D. Fadavi, D. A. Starr, *et al.*, "Role of kash domain lengths in the regulation of linc complexes," *Molecular biology of the cell*, vol. 30, no. 16, pp. 2076–2086, 2019.

[104] M.-C. Spindler, J. Redolfi, F. Helmprobst, P. Kollmannsberger, C. Stigloher, and R. Benavente, "Electron tomography of mouse linc complexes at meiotic telomere attachment sites with and without microtubules," *Communications biology*, vol. 2, 2019.

[105] E. Makhija, D. Jokhun, and G. Shivashankar, "Nuclear deformability and telomere dynamics are regulated by cell geometric constraints," *Proceedings of the National Academy of Sciences*, vol. 113, no. 1, pp. E32–E40, 2016.

[106] F. Lottersberger, R. A. Karssemeijer, N. Dimitrova, and T. de Lange, "53bp1 and the linc complex promote microtubule-dependent dsb mobility and dna repair," *Cell*, vol. 163, no. 4, pp. 880–893, 2015.

[107] D. S. Jokhun, Y. Shang, and G. Shivashankar, "Actin dynamics couples extracellular signals to the mobility and molecular stability of telomeres," *Biophysical journal*, vol. 115, no. 7, pp. 1166–1179, 2018.

[108] M. Herrmann, I. Pusceddu, W. März, and W. Herrmann, "Telomere biology and age-related diseases," *Clinical Chemistry and Laboratory Medicine (CCLM)*, vol. 56, no. 8, pp. 1210–1222, 2018.

[109] S. Bekaert, T. De Meyer, and P. Van Oostveldt, "Telomere attrition as ageing biomarker," *Anticancer research*, vol. 25, no. 4, pp. 3011–3021, 2005.

[110] Y. Doksani, "The response to dna damage at telomeric repeats and its consequences for telomere function," *Genes*, vol. 10, no. 4, p. 318, 2019.

[111] S. E. Artandi, S. Chang, S.-L. Lee, S. Alson, G. J. Gottlieb, L. Chin, and R. A. DePinho, "Telomere dysfunction promotes non-reciprocal translocations and epithelial cancers in mice," *Nature*, vol. 406, no. 6796, pp. 641–645, 2000.

[112] G. Aubert and P. M. Lansdorp, "Telomeres and aging," *Physiological reviews*, vol. 88, no. 2, pp. 557–579, 2008.

[113] N. D. Hastie, M. Dempster, M. G. Dunlop, A. M. Thompson, D. K. Green, and R. C. Allshire, "Telomere reduction in human colorectal carcinoma and with ageing," *Nature*, vol. 346, no. 6287, pp. 866–868, 1990.

Publications

Hsiao-Ching Tsai, Julia Kristin, Maja Strugačevac, Nina Bartels , Constanze Wiek, Jörg Heino Schipper, Mathias Getzlaff. *Biomechanical Evaluation of Human Oral Keratinocytes and Head and Neck Squamous Carcinoma Cells*. Submitted to the *Journal Auris Larynx*, November 2020.

Hsiao-Ching Tsai, Jäger Kathrin, Anna Maria Haschke, Micheal Walter, Mathias Getzlaff. *Biomechanical Research in Human Skin Fibroblasts and Progeria*. Planning to submit to the *Journal of Molecular Recognition*, 2021.

Conference Contributions

H.-C. Tsai, J. Kristin, J. Schipper, M. Getzlaff. Mechanical properties of head and neck squamous carcinoma cells. Talk, *DPG−Frühjahrstagung*, Regenburg, 2019.

F. Stuckmann, H.-C. Tsai, M. Getzlaff. Comparison of mechanical properties of cells using different cantilevers as a probe tips for atomic force microschopy. Poster, *DPG − Frühjahrstagung*, Regenburg, 2019.

K. Stommel, H.-C. Tsai, M. Getzlaff. The use of spherical particles for cantilevers in an atomic force microscope. Poster, *DPG − Frühjahrstagung*, Regenburg, 2019.

H.-C. Tsai, J. Kristin, J. Schipper, M. Getzlaff. Biomechanical research in head and neck squamous carcinoma cells (HNSCC). Talk, *9th AFM BioMed Conference*, Münster, 2019.

H.-C. Tsai, J. Kristin, J. Schipper, M. Getzlaff. Estimating biomechanical properties of head and neck squamous carcinoma cells (HNSCC) with single-molecular force microscopy. Talk, *DPG − Frühjahrstagung*, Dresden, 2020.

S. Sommerhage, H.-C. Tsai, M. Getzlaff. Characterization of an ultrasonic transmitter for mechanical manipulation of cancer cells in vitro. Poster, *DPG − Frühjahrstagung*, Dresden, 2020.

Acknowledgments

The research included in this dissertation could not have been performed if not for the assistance, patience, and support of many individuals. I would like to extend my gratitude first and foremost to my thesis advisor Prof. Dr. Mathias Getzlaff for mentoring me and giving me the chance to do my doctoral thesis at the Institue of Applied Physics of Heinrich Heine University Düsseldorf. He has helped me through extremely difficult times throughout the analysis and the writing of the dissertation and for that, I sincerely thank him for his confidence in me.

Besides my advisor, this research would not have been possible without the assistance of the personnel of Düsseldorf University Hospital, Department of Otorhinolaryngology collaboration who arranged the experimental apparatus and built the foundations in biotechnology. In particular, I would like to thank Prof. Dr. med. Dr. h. c. Jörg Schipper, PD Dr. med. Julia Kristin and Dr. Constanze Wiek for their support and knowledge of Medicine and Biology. I would further like to thank the biostatistician PD Dr. Pablo Emilio Verde for the suggestion in data analysis.

I would additionally like to thank the Institute for Physical Biology of Heinrich Heine University Düsseldorf for giving me access to the laboratory and research facilities. Special thanks should be given to Prof. Dr. Alexander Büll and Mrs. Elke Reinartz who patiently helped me with their knowledge allowing me to fully understand the technical concepts behind the AFM device. Many thanks to M. Sc. Tatsiana Kupreichyk for her technical support.

I would also like to extend my deepest gratitude to Prof. Dr. med. Michael Walter, Dean of the Institute for Clinical Chemistry and Laboratory Medicine of Rostock University Medical Center, for his collaboration in Progeria studies. Special thanks to M. Sc. Anna Maria Haschke and Mgr. Ing. Kathrin Jäger for their scientific advice and assistance.

I also would like to express thanks to Dr. Ing. Tobias Hemsel, Second Dean of Faculty Mechanical Engineering for Dynamics and Mechatronics of the University of Paderbor, for his collaboration in ultrasound technology. Thanks also to Mr. Paul Dunst for controlling ultrasonic processing systems and conducting the LDV measurements.

My sincere thanks also go to the Central Workshop of Heinrich Heine University Düsseldorf for the assistance during the ultrasonic experimental setup. Sincere thanks to Mr. Claudius Möhrle for his technical support.

Many thanks to my colleagues (Dr. Maryam Youhannayee, M. Sc. Mahboobeh Ravankhah, B. Sc. Tobias Löffer, B. Sc. Kai Besocke, and Mrs. Christiane Braun) at the Institue for Applied Physics of Heinrich Heine University Düsseldorf for their encouragement and being the most considerate and interesting people that I have ever worked with.

Getting through the dissertation required more than academic support, and I have many, many people to thank for their listening to and, at times, having to tolerate me. I would like to thank my friends for accepting me despite my flaws.

Most importantly, none of this could have happened without my family. I would like to extend my deepest gratitude to my parents Mr. Chien-Hsin Tsai, Mrs. Li-Kuan Huang, and my brother M. Sc. Po-Han Tsai without whose love, support, and understanding, I could never have completed the doctoral degree.

Eidesstattliche Versicherung

Ich versichere an Eides statt, dass die Dissertation von mir selbstständig und ohne unzulässige fremde Hilfe unter Beachtung der Grundsätze zur Sicherung guter wissenschaftlicher Praxis an derHeinrich-Heine-Universität Düsseldorf erstellt worden ist. Die aus fremden Quellen direkt oder indirekt übernommenen Gedanken sind als solche kenntlich gemacht. Die Arbeit wurde bisher weder im Inland noch im Ausland in gleicher oder ähnlicher Form einer anderen Prüfungsbehörde vorgelegt. Es wurden keine früheren erfolglosen Promotionsversuche unternommen.

Düsseldorf, den

Hsiao-Ching Tsai